Resonant and Time Resolved Spin Noise Spectroscopy of Electron Spin Dynamics in Semiconductors

by

Brennan C. Pursley

A dissertation submitted in partial fulfillment
of the requirements for the degree of
Doctor of Philosophy
(Applied Physics)
in The University of Michigan
2015

Doctoral Committee:

Associate Professor Vanessa Sih, Chair
Professor Pallab K. Bhattacharya
Professor Rachel S. Goldman
Professor Cagliyan Kurdak
Associate Professor Jennifer P. Ogilvie

“Kein versuch ist so dumm, dass man ihn nicht probieren sollte.”

```
"No experiment is so dumb, that it should not be tried."
```

—Edgar Meyer quoted by Walther Gerlach ca. 1920 [1, 2]

For my wife Shoshana and my boys Mason and Liam

ACKNOWLEDGEMENTS

It has taken many years to reach the point of writing this document—about eleven from community college to thesis defense. Many people have left a positive impact on my life throughout this journey. I will now attempt thank some of the biggest contributors.

I cannot imagine that I would have made it here if it were not for my wife Shoshana. She has helped add balance and direction to my life while providing an immense amount of love and support. We have come a long way together and the future is looking brighter than ever.

I am grateful for the guidance and patience of my adviser Professor Vanessa Sih. Her door is always open and I have found our discussions invaluable. She has been an excellent mentor to me over the last five years.

I would like to thank my fellow group members, both past and present, especially Benjamin Norman, Marta Luengo-Kovac, and Xinlin Song. Ben helped me develop a much clearer understanding of spin physics and our measurement systems, including a fortuitous critique during my early analysis of spin noise. Marta and Xin have both been excellent sounding boards and assisted in measurements that led directly to publications.

I would like to thank the members of my committee for their collaboration and feedback over the years. In particular, I thank Professor Rachel Goldman who helped me become a much better writer. I also thank Professor Cagliyan Kurdak who offered sound guidance throughout my tenure in the Applied Physics Program.

My undergraduate years put me on solid footing to transition to graduate level work. This is primarily thanks to Professor Dimitri Basov and some key members of his lab at the time: Alex Schafgans, Andrew LaForge, Brian Chapler, and Tom Driscoll. I learned a tremendous amount about being a research scientist from them, along with developing skills that I still use to this day. While at UCSD, I also had the pleasure of studying under Professor Daniel Arovas for several courses. If I someday have a chance to teach, I hope to emulate his enthusiasm, clarity, and generosity.

My educational journey began in community college where I failed the first physics course I ever took. Professor Takashi Nakajima transformed my understanding of the world while setting standards that I still strive to achieve. Working for Professor Daniel Finkenthal was my first opportunity to contribute meaningfully to research, solidifying my desire to become a physicist. Arthur Gerwig's robotics class let me truly tinker with electronics for the first time in my life. I will be forever grateful for the experiences I gained with their help.

TABLE OF CONTENTS

LIST OF FIGURES

Figure

LIST OF APPENDICES

Appendix

LIST OF ABBREVIATIONS

ADC analog-to-digital convertor

BPD balanced photo-diode bridge

CISP Current Induced Spin Polarization

EOM electro-optic modulator

Op-amp operational amplifier

PL photoluminescence

TRFR Time Resolved Faraday Rotation

TRFR/KR Time Resolved Faraday and Kerr Rotation

TRPL Time Resolved Photoluminescence

TRSN Time Resolved Spin Noise

RMS root-mean-square

RSA Resonant Spin Amplification

RSN Resonant Spin Noise

ABSTRACT

Resonant and Time-Resolved Spin Noise Spectroscopy of
Electron Spin Dynamics in Semiconductors

by

Brennan C. Pursley

Chair: Associate Professor Vanessa Sih

Determining the spin properties of novel materials is necessary for the development of proposed spin-based information processing devices, or spintronics. While existing optical techniques work for some semiconductors, they are ineffective for other strategic material systems. In this dissertation, we explore gallium arsenide bismuthide alloys and irradiated gallium arsenide using conventional methods. We then introduce the novel techniques of Resonant and Time Resolved Spin Noise which may enable optical studies of previously inaccessible materials.

Gallium arsenide bismuthide has a large tunable spin-orbit splitting, which could be desirable for spintronic applications. Hanle effect measurements reveal that the product of the g factor and effective spin lifetime (gT_s) ranges from 0.8 ns at 40 K to 0.1 ns at 120 K, while below 40 K there was negligible change. The temperature dependence of gT_s shows evidence of thermally activated behavior attributed to hole localization at Bi or Bi cluster sites.

Modern electronics are sensitive to radiation damage and require extensive modification for use in space, nuclear robotics, and other environments, but the effects of

long term exposure on spin properties had not previously been investigated. Time Resolved Kerr Rotation measurements of irradiated gallium arsenide reveal robust spin behavior to 5 MeV protons up to a 10^{14} p/cm^2 fluence, even as photoluminescence intensity decreases by two orders of magnitude.

Spin noise measurements are sensitive and capable of surpassing more established methods. However, the majority of schemes are restricted to Fourier analysis, record all sources of noise, and suffer digitizing restrictions. Since digitization involves discrete binning, amplitude resolution is limited by background fluctuations. Our novel techniques, Resonant and Time Resolved Spin Noise, bypass these issues using ultrafast laser pulses in tandem with analog electronic calculations that remove the background prior to digitizing. In principle, our system's accessible bandwidth for spin dynamics is $\sim$10 THz with sub-nanoradian/$\sqrt{Hz}$ signal resolution using commercially available components. We demonstrate this measurement technique on a bulk n-type gallium arsenide sample and extract values for the g factor and dephasing time that are consistent with results from Time Resolved Faraday Rotation and Resonant Spin Amplification.

CHAPTER I

Introduction

1.1 Why Spintronics?

Computer technology is ubiquitous and, in many ways, required for modern life. Typical smartphones are so powerful that NASA is using them in a fleet of satellites.[3] These facts are astonishing when contrasted with the age of the transistor–68 years old this December.[4] At present, there are plans to reduce transistor feature size through 2028.[5] However, as dimensions decrease, capability improvements are expected to be modest and there will be many challenges to successful fabrication.[6, 7] Attempts to achieve order of magnitude improvements beyond today's technology, be it computation speed or power consumption, will require something beyond the electronic transistor.

Transistors are the workhorse of modern technology because they can manipulate and store information through binary encoding—high or low voltages. But information can be encoded in a near limitless variety of forms. For example, quantum information storage through entangled system elements could allow significantly denser information storage and processing speeds. The recent 30 GHz manipulation of two entangled quantum dot electrons separated by 9 nm of material can hold a superposition of four distinct states in a space comparable to the smallest feature size of a modern transistor.[8] However, quantum computation is far from being available

for handheld devices. The first transistor functioned at room temperature with a few wires and a power supply. The state-of-the-art quantum information systems require vacuum systems and cryogenic temperatures.[9] If we desire significant and widely available computation improvements past the year 2030, we will need something else.

One alternative is to encode information using ensemble spin polarizations that allow classical limit modeling. Electrons are Fermions with a spin of 1/2, and as such, are a two-state system, follow the Pauli exclusion principle, and obey Fermi-Dirac statistics. Spintronics exploits these properties of electrons in a myriad of ways. Most consumers have already used a spintronic device: the read sensor of a hard disk drive.[10, 11] In 2007, a "spin field-effect transistor" was demonstrated in silicon, the core material of the electronics industry.[12] If spintronic logic is to become mass produced, the robust fabrication techniques for silicon would greatly simplify the endeavor—though there are many other challenges to overcome. With diminishing improvements for electronic transistors, spintronic gating demonstrated, and some consumer spintronics already available, one would expect fully spintronic computers on the horizon.

1.2 Why Spin Noise?

In order to engineer the next generation of technology, we need to thoroughly understand the material systems available to us and predict the behavior of structures that may not exist at present. This requires measurement techniques that can extract the precession frequency and spin dephasing time for a variety of materials that, respectively, have tunable carrier densities, mobilities and other unique properties. Spin noise can perform the necessary tasks while also being a contactless, nearly non-perturbative, optical method.

Spin dephasing times and g factors, beyond their base engineering utility, can also be used as another level of contrast for imaging and analysis. Proof-of-principle spin

noise based experiments have demonstrated three-dimensional carrier density mapping in bulk materials and the extraction of a homogeneous transition linewidth for an ensemble of quantum dots.[13, 14] Pump-probe methods would have proven difficult, if not impossible, to use for extraction of the same information due to absorption, beam profile, and energy selectivity issues. We direct the reader to the cited papers as further discussion of those measurements is beyond the scope of this dissertation.

Conventional continuous wave laser spin noise measurement systems leave a gap in sensitivity and bandwidth that requires the development of an alternative. Pulsed laser systems are ideal for accessing high speed dynamics that are well out of range for most electronics, and a few attempts at incoporating them have already been made.[15, 16, 17, 18] However, nearly all spin noise methods use a fast analog-to-digital convertor (ADC) for signal processing. This means that all sources of noise are recorded, reducing signal resolution. Moreover, aliasing—the appearance of a high frequency signal at a low frequency due to finite spaced sampling—has to be employed to observe frequencies beyond the Nyquist cutoff, complicating analysis. Our techniques of Resonant and Time Resolved Spin Noise bypass these issues while keeping many of the benefits inherent to spin noise experiments.

1.3 Organization

This dissertation addresses material characterization hurdles through the development of Resonant and Time Resolved Spin Noise. In the dissertation, we will survey physical concepts and experiments, building toward the need for, and understanding the role of, these new techniques. Proof-of-principle measurements demonstrate capabilities that are unachievable with existing methods.

Our focus will be on *how* one measures the spin physics of electrons within a semiconductor. To understand *what* we learn through experimentation, Ch. II discusses semiconductors and spin dynamics modeling. In the hope of clarity, we will keep

the development of relevant physics brief, add historical perspective when useful, and guide the reader to more thorough texts through citations. In Ch. III we discuss equipment used for conventional measurements, followed by Ch. IV with a discussion of standard spin dependent optical techniques.

The latter portion of the dissertation discusses experimental results. Chapter V is dedicated to a study of GaAsBi which promises to offer a tunable spintronic parameter. Chapter VI explores the robust spin dynamics of GaAs in the face of proton irradiation. Radiation poses a difficult challenge when designing satellite systems or equipment that will work in hazardous environments. The possibility that a spintronic device could function normally in a harsh environment without extensive modifcations is exciting.

Chapter VII is where we discuss the ideas and modeling behind Resonant and Time Resolved Spin Noise, including proof-of-principle measurements. We will rely on information from the previous chapters to aid in analysis and contrast with the novel capabilities. In Ch. VIII, we summarize this dissertations' contributions to the advancement of our understanding of spin dependent physics and the enhancement of available spin based measurement techniques.

CHAPTER II

Spin Physics in Semiconductors

Spin is the quantized intrinsic angular momentum of a particle. It is qualitatively useful to imagine a charged particle spinning about its central axis where the rotation—beyond having angular momentum—leads to a magnetic moment. Spin and magnetic moments are thus intimately related. Oddly enough, neutrons have a magnetic moment even though the net charge is zero. This is because neutrons are made up of subatomic particles known as quarks which have their own charge and associated spin—the charges cancel while the angular momentum does not. It is important to note that this classical analogy, though a useful way to picture spin, is not what quantitative calculations should be based upon. A thorough derivation of spin requires relativistic quantum mechanics using methods developed by Dirac.[19]

In this chapter I will review the physical concepts necessary to understand the experiments discussed in the manuscript. Each section topic could fill a textbook in its own right so we guide the reader to useful references for more detailed discussions. The sections are organized as follows: Sec. 2.1, the Stern-Gerlach experiment and its analysis; Sec. 2.2, semiconductor band theory, dopants, and scattering; Sec. 2.3, spin dynamics including the Bloch-Torrey equations, dephasing, optical selection rules, and Faraday rotation.

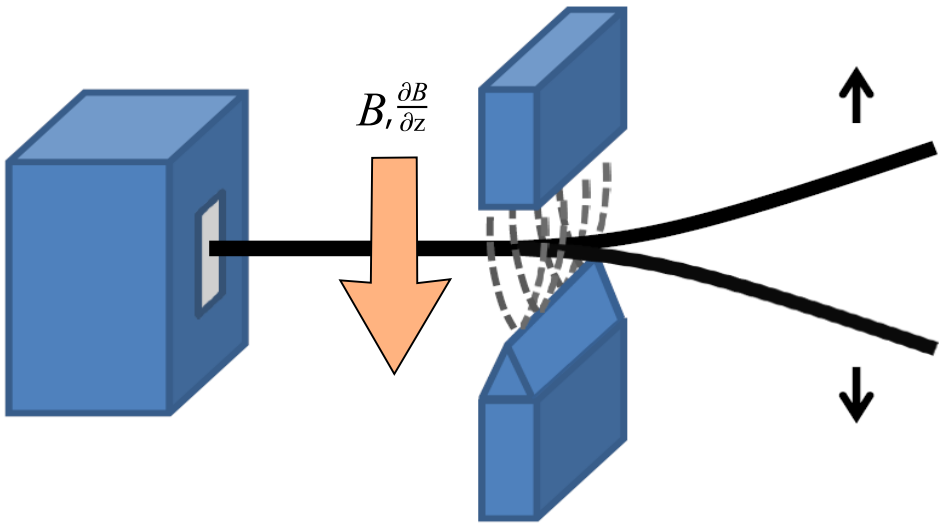

Figure 2.1: Schematic of Stern-Gerlach apparatus. B is the magnetic field, $\partial B/\partial z$ is the gradient of the field. Both point along the direction of the orange arrow. The small black arrows represent the orientation of angular momentum that led to the splitting of the beam of silver atoms. Stern and Gerlach believed they were measuring effects from quantized *orbital* angular momentum, when in fact, the splitting of the beam of silver atoms that they observed was due to quantized *spin* angular momentum.

2.1 The Stern-Gerlach Experiment

The first experiment to solidify quantum mechanics and imply the existence of spin, was performed by Otto Stern and Walther Gerlach in 1922.[20] At the time, the best quantum model was Bohr's atomic theory which, when combined with "space quantization"—the quantization of physical orientation—yielded a two state discretization of orbital angular momentum for the hydrogen atom.[2] Doubt surrounded the validity of quantum mechanics as aspects of Bohr's predictions could be accounted for using classical arguments and "space quantization" had not been observed. In 1921, Stern proposed that if hydrogenic atoms were passed through a magnetic field with a gradient in the same direction, then the idea of "space quantization" could be tested directly.[21]

Figure 2.1 shows a schematic of the Stern-Gerlach apparatus. A beam of atoms

is generated by heating silver to 1000° C in an oven and passing the output through a series of two slits. The beam then passes through specially shaped magnets so that both the field and its non-zero gradient point in the same direction. If we define the graded field as pointing in the z-direction, then the force on the magnetic moment of the atoms is: [22]

$$F_z = \frac{\partial}{\partial z}\left(\boldsymbol{\mu} \cdot \boldsymbol{B}\right) \simeq \mu_z \frac{\partial B_z}{\partial z} \tag{2.1}$$

Therefore, if there are only two allowed magnetic moments in the z-direction, a single unpolarized incident beam will be split by deflection in two directions. If this is not the case, the single beam would be smeared out over the screen.

Silver was chosen as it has only one electron in its outermost orbital thereby making it hydrogenic and easier to interpret. The Stern-Gerlach experiment was both fortuitous and erroneous. On one hand, they had confirmed the quantization of angular momentum in a visually striking way: the physical separation of two beams of atoms, sputtered onto a screen due to quantization. On the other hand, their guiding principle for performing the experiment, and subsequent interpretation of the results, was wrong. They were truly lucky in observing any effect at all. It would be several more years before anyone would make the connection between the Stern-Gerlach measurements and what we now call the spin of the electron.

2.2 Semiconductors

Semiconductors are materials that straddle the resistive and conductive regimes. Namely, we assume that we can *tune* the electrical conductivity of the material through temperature, doping, or some other method enabled by partially filled *bands* and a *bandgap*. The existence of bands and the associated gap allow for optical transitions to manipulate and interrogate a sample. This is the key to the measurement

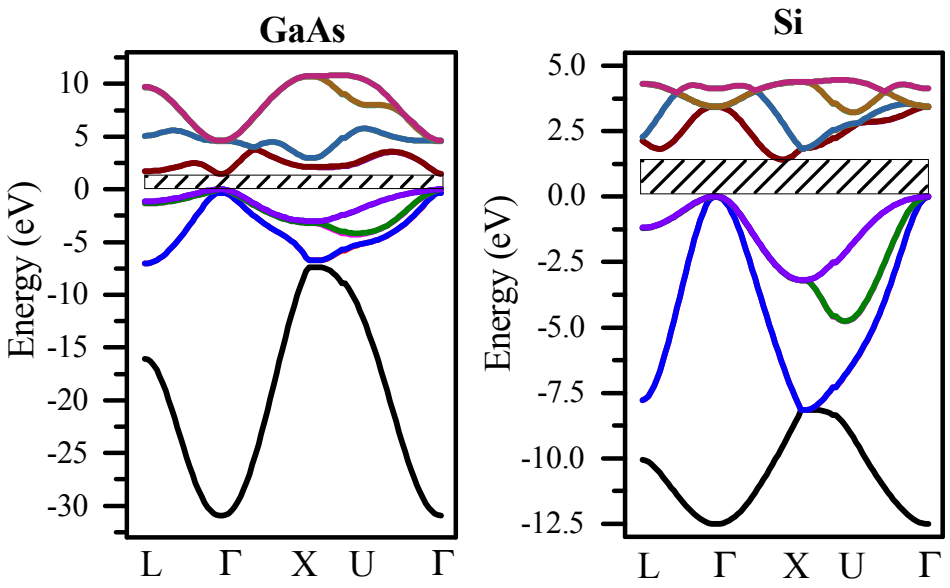

Figure 2.2: Tight binding method calculations of (left) GaAs and (right) Si band-structure. Dashed rectangles are the bandgaps. Calculations used an 8x8 Hamiltonian with up to next nearest neighbor interactions and include spin-orbit coupling. Reference data from pseudopotential calculations was used to seed the interpolation of parameters. Code was developed by John Hinckley.

techniques we will discuss in Ch. IV.

2.2.1 Band Theory

All materials are made of atoms so it is reasonable to assume that we can *build* material models based on our knowledge of the constituent atoms. This idea was first put forth by Bloch in 1928 and is commonly referred to as the "tight binding method."[23] We will briefly discuss the conceptual aspects to the formation of bands and how one makes calculations from there. Figure 2.2 shows two examples of tight binding calculations performed for gallium arsenide (GaAs) and silicon (Si). For an introduction to band theory and all things semiconductor, we recommend the references [24, 25].

2.2.1.1 The Tight Binding Method

We begin by assuming that we have solved the time-independent Schrodinger equation for the energy levels of the relevant atoms of our solid.

$$H\psi_n = E_n\psi_n \tag{2.2}$$

H is the Hamiltonian of the atom, E_n are the allowed energies, and ψ_n are the wavefunctions. We then arrange the atoms in a periodic lattice at distances such that the atoms do not yet "know" they are on a lattice. Slowly, we contract the lattice such that the energies of the outermost, or valence, electrons of the atoms begin to be perturbed. Our problem for understanding a solid has reduced to calculating the perturbation of the electronic wavefunctions when placed in a lattice. "Tight binding" describes our approximation that the electrons are bound to their host nucleus and perturbed by neighboring electrons and nuclei.

Wavefunctions in a periodic lattice are described by Bloch's Theorem and have the form[25]:

$$\phi_{\boldsymbol{k}}(\boldsymbol{r}) = u_{\boldsymbol{k}}(\boldsymbol{r})\, exp(i\boldsymbol{k}\cdot\boldsymbol{r}) \tag{2.3}$$

$$u_{\boldsymbol{k}}(\boldsymbol{r}) = u_{\boldsymbol{k}}(\boldsymbol{r}+\boldsymbol{R}) \tag{2.4}$$

where $\boldsymbol{r}$ is the electron position relative to the host nucleus, $\boldsymbol{R}$ is the lattice spacing, and our label $\boldsymbol{k}$ is the electron wavevector which is proportional to the momentum and inversely so to the de Broglie wavelength. We now assume we can expand $\phi_{\boldsymbol{k}}(\boldsymbol{r})$ in terms of $\psi_n(\boldsymbol{r})$ and solve for the expansion coefficients using the perturbation of the atomic Hamiltonian. In principle, we are done and have all the information we need. In practice, solving for the wavefunctions and allowed energies is non-trivial and requires approximations with varying applicability.

2.2.1.2 Bandgaps and the "Nearly Free Electron"

Using the tight binding method, we started with atoms so we also started with discrete energy spacing. We assume that as we brought the atoms together, the interaction was slight enough to warrant using perturbation theory. The resulting interactions broaden the atomic levels creating a dispersion relation between momenta and energy, or "band." The gaps between atomic energy levels remain assuming the perturbation is not strong enough to blend them.

There is an alternate approach, as with anything in quantum mechanics, to developing bands. One that works well for metals is called the "nearly free electron" model. Basically, start with a free electron and its associated wavefunction, create a weak periodic potential made up of positive charges—think bare nuclei—and then solve for the new wavefunction using perturbation theory.

The "nearly free" approach offers an enlightening way to think about bandgaps: the gaps are the result of Bragg reflection at the Brillouin zone edges. William Henry Bragg, and his son William Lawrence Bragg, shared the 1915 Nobel Prize in Physics "for their services in the analysis of crystal structure by means of X-rays."[26] What they did was connect the diffraction pattern of x-rays to the underlying crystal structure of materials.

With the "nearly free electron," we start with a plane wave solution. Plane waves will interfere when scattered from a periodic potential, and for certain wavevectors $\boldsymbol{k}$—the edges of the Brillouin zone—standing waves form. Since we are using perturbation theory, our original plane waves are no longer solutions, but superpositions of them are. At the Brillouin zone edges, we have multiple new solutions, all different superpositions of our original standing waves, which leads to different distributions of the electron wavefunction. These distributions vary the density of electrons near or far from the lattice sites resulting in different respective potential energies. Therefore, at the Brillouin zone boundary, we have the formation of energy gaps.

2.2.1.3 Spin-Orbit Coupling and Other Perturbations

We have said we are using perturbation theory, and we have even hinted that we are using Coulombic potentials, but we have not explicitly addressed this critical issue. The proper *choice* of potential determines the validity of our solutions, as well as their ease of calculation. The simplest case is that of a rigid periodic array of screened Coulombic-like potentials. Note that we use a *rigid* lattice. We reserve all motion, besides that of a nearly free electron, to the subject of scattering theory.

The periodicity of our lattice depends upon the constituent atoms and corresponding unit cell. The unit cell is the smallest collection of elements that can be repeated and interconnected to form a lattice—the reciprocal of the unit cell in momentum, or $\boldsymbol{k}$space, is the Brillouin zone. In practice, one determines the potential profile of a unit cell and then perturbs that profile. This allows for the modeling of mono-atomic materials and multi-atom alloys all the way through superlattice heterostructures.

The next perturbation, typically in terms of importance, is spin-orbit coupling. Without it, we have neglected a degree of freedom for the electron and eliminated entirely our ability to model material spin dynamics. Spin-orbit coupling stems from the Zeeman interaction

$$H_Z = -\boldsymbol{\mu} \cdot \boldsymbol{B_{eff}} \tag{2.5}$$

where $\boldsymbol{\mu} \sim \widehat{\boldsymbol{S}}$ is the magnetic dipole moment of the electron with $\widehat{\boldsymbol{S}}$ its spin angular momentum. $\boldsymbol{B_{eff}}$ is the effective magnetic field that the electron "sees" as it moves through the potential gradient of the lattice.

Special relativity tells us that a static electric field in the rest frame appears as a superposition of static electric and magnetic fields in a moving frame. This can be written as

$$\boldsymbol{B_{eff}} \sim \boldsymbol{E_{lat}} \times \frac{\boldsymbol{v}}{c} \tag{2.6}$$

where $\boldsymbol{E_{lat}}$ is the gradient of the lattice potential, $\boldsymbol{v}$ the electron drift velocity, and c

the speed of light. We connect the magnetic field to the orbital angular momentum of the electron by noting that $\boldsymbol{E_{lat}}$ is strictly along $\boldsymbol{r}$ from our choice of potential, and that

$$\widehat{\boldsymbol{L}} \sim \boldsymbol{r} \times \boldsymbol{v} \tag{2.7}$$

where $\widehat{\boldsymbol{L}}$ is the electron orbital angular momentum. Putting everything together, our Hamiltonian is

$$H_{SO} \sim \widehat{\boldsymbol{L}} \cdot \widehat{\boldsymbol{S}} \tag{2.8}$$

hence, the spin-orbit interaction. As one might expect, a Zeeman type interaction will result in energy splitting and we observe more structure in the bands.

2.2.1.4 The $\boldsymbol{k \cdot p}$ Method

There are many, Many, MANY other ways to perturb the bandstructure. The deformation potential which accounts for strain is but one example and is often required for heterostructures. While the full band structure can be fairly complicated, for practical purposes we can ignore almost everything except for a small region in $\boldsymbol{k}$-space between the bottom of the conduction band and top of the valence band, commonly referred to as the bandedges.

All of the action in a material happens where the electrons are mobile. This occurs primarily near the bandedges for many materials. The $\boldsymbol{k \cdot p}$ method allows us to approximate the bandedges using quadratic functions where the curvature is determined through an "effective mass." All of the relevant material information resides in the effective mass parameter and the energy separation of the bands. Rather than interpolate behavior between lattice sites like the tight binding method, we extrapolate from solutions at the bandedges using the quadratic functions. The simplest type of semiconductor has a direct gap where the bandedges are both at the Γ-point where $\boldsymbol{k} = 0$. GaAs has a direct gap and will be our focus for the remainder of

this manuscript. Silicon, the backbone of the electronics industry, has an indirect gap because the highest point in the valence band is at Γ while the conduction band minimum is at X (see Fig. 2.2) and is a bit tougher to work with both optically and theoretically.

$\boldsymbol{k \cdot p}$ theory gets its name from a term in the modified unit cell Hamiltonian. We start with the standard Schrodinger equation, assume it operates on Bloch states, and perform some mathematical manipulations to reach

$$\left(\frac{p^2}{2m_0} + V(r) + \frac{\hbar}{m_0}\boldsymbol{k \cdot p} + \frac{\hbar^2 k^2}{2m_0}\right) u_{n,\boldsymbol{k}} = E_{n,\boldsymbol{k}} u_{n,\boldsymbol{k}} \tag{2.9}$$

Using the above equation with perturbation theory allows us, in certain symmetry conditions, to write

$$E_{n,\boldsymbol{k}} = E_{n,0} + \sum_{i,j} \frac{\hbar^2}{m^*_{i,j}} k_i \cdot k_j \tag{2.10}$$

with $m^*_{i,j}$ being an effective mass. We will now jump to some results, but for the interested reader, a useful derivation can be found in Ref. [24].

In materials like GaAs, we can limit our focus to the following four bands: Conduction, Heavy Hole, Light Hole, and Split-Off. For GaAs, the conduction band has s-like wavefunctions $\left(j = \frac{1}{2} \rightarrow \Phi_{\frac{1}{2},\frac{1}{2}}, \Phi_{\frac{1}{2},\frac{-1}{2}}\right)$ and a simple dispersion relation for the energy:

$$E_c = E_g + \frac{\hbar^2 k^2}{2m^*_c} \tag{2.11}$$

with E_g being the bandgap and m^*_c being an effective mass of the conduction band electron. For the remaining valence bands, life is more complicated as they are p-like with corresponding total angular momentum $j = \frac{3}{2}$. If we assume there is large spin-orbit coupling, as in many semiconductors, we can ignore the split-off band and use the 4×4 Luttinger-Kohn matrix equation.[24, 27]

$$-\begin{pmatrix} H_{hh} & b & c & 0 \\ b^* & H_{lh} & 0 & c \\ c^* & 0 & Hlh & -b \\ 0 & c^* & -b^* & H_{lh} \end{pmatrix} \begin{pmatrix} \Phi_{\frac{3}{2},\frac{3}{2}} \\ \Phi_{\frac{3}{2},\frac{1}{2}} \\ \Phi_{\frac{3}{2},\frac{-1}{2}} \\ \Phi_{\frac{3}{2},\frac{-3}{2}} \end{pmatrix} = E \begin{pmatrix} \Phi_{\frac{3}{2},\frac{3}{2}} \\ \Phi_{\frac{3}{2},\frac{1}{2}} \\ \Phi_{\frac{3}{2},\frac{-1}{2}} \\ \Phi_{\frac{3}{2},\frac{-3}{2}} \end{pmatrix} \tag{2.12}$$

with the following element definitions

$$H_{hh} = \frac{\hbar^2}{2m_0}\left[(\gamma_1+\gamma_2)\left(k_x^2+k_y^2\right)+(\gamma_1-2\gamma_2)\,k_z^2\right] \tag{2.13}$$

$$H_{lh} = \frac{\hbar^2}{2m_0}\left[(\gamma_1-\gamma_2)\left(k_x^2+k_y^2\right)+(\gamma_1+2\gamma_2)\,k_z^2\right] \tag{2.14}$$

$$b = \frac{-\sqrt{3}i\hbar^2}{m_0}\gamma_3\left(k_x-ik_y\right)k_z \tag{2.15}$$

$$c = \frac{\sqrt{3}\hbar^2}{2m_0}\left[\gamma_2\left(k_x^2-k_y^2\right)-2i\gamma_3 k_x k_y\right] \tag{2.16}$$

For GaAs, the Kohn-Luttinger parameters are [24]

$$\gamma_1 = 6.85$$

$$\gamma_2 = 2.1$$

$$\gamma_3 = 2.9$$

The band structure is certainly simpler to work with when compared to the tight binding model, but the valence band result is still too complicated for back of the envelope calculations. If we make the further approximation that the relevant physics near the Γ-point can be represented with just a parabolic dispersion relation, then we can empirically extract an effective mass. The values for GaAs below, taken from

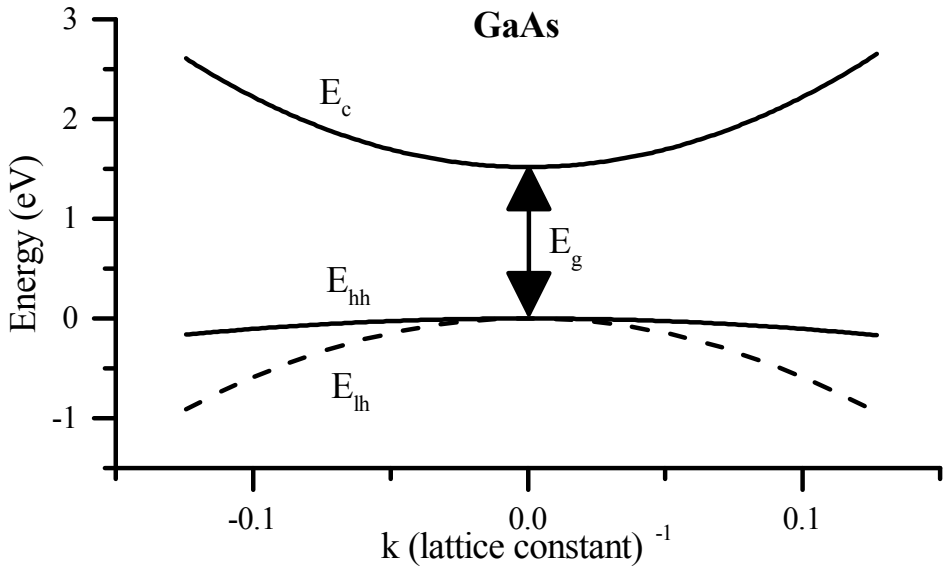

Figure 2.3: Plot of the approximate bandstructure of GaAs about the Γ-point using the effective mass approximation. $\boldsymbol{k}$ is in units of the inverse lattice constant, equal to $(5.65\ \text{Å})^{-1}$.

Ref. [24], can be used for density of states calculations.

$$m_c^* = 0.067 m_0$$

$$m_{hh}^* = 0.45 m_0^*$$

$$m_{lh}^* = 0.08 m_0^*$$

We use the above effective mass values to make Fig. 2.3. Often, such a figure is used to represent the direct gap behavior of various materials. It should be clear that the diagram is only accurate near the bandedge.

2.2.2 Holes

At this point, the reader may wonder "What are holes?" We discussed band theory from the perspective of perturbations of electron wavefunctions but then called certain bands "heavy hole" and "light hole." A "hole" is a pseudoparticle that conveniently represents the motion of a *missing* electron from a collection of many electrons. As

such, it has opposite charge, momentum, and spin compared to the electron that used to be there—a full band should be charge-neutral with no net momentum or spin at equilibrium, with a few exceptions that we will not discuss. Holes are commonly formed when an electron is promoted from the valence band to the conduction band or an acceptor site (impurity that attracts an electron). Since we will be doing optical studies, we will purposefully promote electrons to the conduction band, and must acknowledge the formation of holes. However, many spin dependent theories disregard their behavior as the hole spin lifetime is often significantly shorter than the electron spin lifetime. This is due to the complexity of the valence band, compared to the conduction conduction band, which leads to more dramatic hole scattering from the same mechanisms we will discuss in section 2.2.4.

2.2.3 Doping

The term "acceptor", introduced in the previous subsection (2.2.2), comes from the notion that impurities can modify the free carrier density. The idea of "doping" is the introduction of more electrons to the conduction band than are *intrinsically* available through "donors," or comparably, more holes to the valence band through "acceptors." A material with more donors than acceptors is called "n-type" with the inverse being "p-type." The number of dopants affects the conductivity through a modified carrier density, and the momentum relaxation time through ionized impurity scattering (discussed below). Our focus is not on the modification of electronic properties of materials and we will see later (Ch. VI) that they can be divorced almost entirely from the relevant spin parameters. Doping does alter the bandstructure through modification of the spin orbit interaction which affects dephasing. It also makes a difference in how certain experiments are carried out (Ch. IV). If an experimenter wanted to apply a bias to a sample and make the carriers move in a specific direction, then doping would play a much larger role. We will reserve ourselves

to thinking of it as a tunable parameter with qualitative behavior modifications, but will not explore the trends in detail.

2.2.4 Momentum Scattering

No discussion of semiconductors would be complete without mentioning momentum scattering. We are only concerned with scattering that might perturb the spin state and will keep our discussion of particular mechanisms brief. Spin dephasing is discussed in section 2.3. Classical scattering theory is encompassed by the Boltzmann transport equation so we introduce the model and quickly reach the relaxation time approximation. The Boltzmann equation can be used as a jumping point to derive spin dynamics as outlined in Ref. [28]. For practical purposes, we discuss the scattering matrix and its utility in determining scattering times.

2.2.4.1 Boltzmann Transport

We will follow the treatment outlined in Appendix F of Ref. [25]. Let us define a distribution function in terms of time, position and particle velocity $\rightarrow f(t, \boldsymbol{r}, \boldsymbol{v})$. Now we let it evolve some differential amount $f(t, \boldsymbol{r}, \boldsymbol{v}) \rightarrow f(t + dt, \boldsymbol{r} + d\boldsymbol{r}, \boldsymbol{v} + d\boldsymbol{v})$. According to the Liouville theorem, the volume element is conserved unless there are collisions. Therefore

$$f(t + dt, \boldsymbol{r} + d\boldsymbol{r}, \boldsymbol{v} + d\boldsymbol{v}) - f(t, \boldsymbol{r}, \boldsymbol{v}) = dt \left(\frac{\partial f}{\partial t}\right)_{coll} \tag{2.17}$$

Rewriting the left hand side as a differential equation, we have

$$\frac{\partial f}{\partial t} + \boldsymbol{v} \cdot \nabla_{\boldsymbol{r}} f + \boldsymbol{\alpha} \cdot \nabla_{\boldsymbol{v}} f = \left(\frac{\partial f}{\partial t}\right)_{coll} \tag{2.18}$$

where $\boldsymbol{\alpha}$ is an acceleration of the particles. This is known as the Boltzmann transport equation.

We now make the relaxation time approximation for collisions. All this means is that we assume an exponential decay towards equilibrium. We write the approximation as

$$\left(\frac{\partial f}{\partial t}\right)_{coll} = \frac{-\left(f - f_0\right)}{\tau_c} \tag{2.19}$$

where f_0 is the equilibrium distribution and τ_c is the carrier relaxation time. This should not be confused with momentum or energy relaxation. In order to calculate momentum, energy, or any other relaxation that depends upon carrier scattering, we must perform a weighted average. In the notation of Ref. [24]

$$\langle\langle \tau_c \rangle\rangle = \frac{\langle \tau_c \chi \rangle}{\langle \chi \rangle} \tag{2.20}$$

where single brackets are an average over the equilibrium distribution of χ while the double brackets represents an average of the perturbed distribution. Such averaging is only valid for small perturbations of the distribution function. The Boltzmann equation assumes that we are following a single particle while the averaging takes into account that we experimentally work with ensembles.

Our final form of the Boltzmann equation is

$$\frac{\partial f}{\partial t} + \boldsymbol{v} \cdot \nabla_{\boldsymbol{r}} f + \boldsymbol{\alpha} \cdot \nabla_{\boldsymbol{v}} f = \frac{-\left(f - f_0\right)}{\tau_c} \tag{2.21}$$

We can introduce whatever external forces we want via the $\boldsymbol{\alpha}$ term and extract an associated relaxation time. It should be noted that the differential equation is four dimensional (three spatial, plus time) and has two different gradients (velocity and position). The Boltzmann equation is non-trivial to solve and a host of other approximations typically go into its use. The interested reader should consult [25, 24]

2.2.4.2 Scattering Matrix Formalism

The scattering matrix element determines how a particle with state $\boldsymbol{k}$ at time 0 gets to state $\boldsymbol{k'}$ through a *unitary* perturbing Hamiltonian $H_{pert}(\boldsymbol{r}, t)$.

$$H_{\boldsymbol{k'},\boldsymbol{k}} = \langle \psi_{\boldsymbol{k'}} | H_{pert}(\boldsymbol{r}, t) | \psi_{\boldsymbol{k}} \rangle \tag{2.22}$$

We invoke Fermi's Golden Rule to get the scattering rate from $\boldsymbol{k} \to \boldsymbol{k'}$ and achieve

$$S_{\boldsymbol{k},\boldsymbol{k'}} = \frac{2\pi}{\hbar} |H_{\boldsymbol{k'},\boldsymbol{k}}|^2 \delta(E_{\boldsymbol{k'}} - E_{\boldsymbol{k}}) \tag{2.23}$$

Equation 2.23 assumes the scattering is elastic (i.e. no emission or absorption). This is fine for many cases but we require a more general form. If we assume the perturbation is harmonic $\left(\text{i.e. } H_{pert}(\boldsymbol{r}, t) \to \mathcal{H}(\boldsymbol{r}, t)\, e^{+i\omega t} + \mathcal{H}^{\dagger}(\boldsymbol{r}, t)\, e^{-i\omega t}\right)$, then we can generalize Eq. 2.23 to

$$S_{\boldsymbol{k},\boldsymbol{k'}} = \frac{2\pi}{\hbar} \left(|H^{a}_{\boldsymbol{k'},\boldsymbol{k}}|^2 \delta(E_{\boldsymbol{k'}} - E_{\boldsymbol{k}} - \hbar\omega) + |H^{e}_{\boldsymbol{k'},\boldsymbol{k}}|^2 \delta(E_{\boldsymbol{k'}} - E_{\boldsymbol{k}} + \hbar\omega) \right) \tag{2.24}$$

where a stands for absorption and e for emission. We note that $|H^{e}_{\boldsymbol{k'},\boldsymbol{k}}|^2 = |H^{a}_{\boldsymbol{k'},\boldsymbol{k}}|^2$ since we have assumed our perturbation to be Hermitian.

2.2.4.3 Ionized Impurities

Ionized impurities are accounted for by assuming they are isolated and have a screened Coulombic potential. Such a perturbation changes the spin-orbit coupling in a localized region and leads to spin scattering. We set $H_{pert}(\boldsymbol{r}, t) = \frac{q}{4\pi\epsilon r} e^{-\lambda r}$, where ϵ is the dielectric constant and λ the screening constant. We get the carrier scattering rate by integrating over all final states using Eq. 4.26 from [24]

$$\frac{1}{\tau_c} = \int S_{\boldsymbol{k},\boldsymbol{k'}} (1 - \cos\xi)\, d^3k' \tag{2.25}$$

The angle ξ, determined by $\cos\xi \simeq \frac{\boldsymbol{v_k}\cdot\boldsymbol{E}}{\boldsymbol{v_{k'}}\cdot\boldsymbol{E}}$ where E is the electric field, stems from the assumption that the bands are isotropic at the scattering point and accounts for directional dependence. We must then perform an appropriate weighted average as discussed above for Boltzmann transport. In the end, we can calculate the temperature dependence for ionized impurity momentum scattering (when our assumptions hold)

$$\tau_{ion} \sim T^{\frac{3}{2}} \tag{2.26}$$

2.2.4.4 Phonons

Phonons are quantized oscillations of the entire crystal lattice. As such, they perturb the spin orbit coupling through strain via the deformation potential leading to spin flips. A thorough derivation of phonon dispersion is beyond the scope of this section but can be found in Ref. [25]. Once the dispersion relation is known, the scattering matrix formalism can be used to derive physical behavior. The important point here is that phonons have momentum and energy dispersion such that electrons with different energy and momenta experience different phonon scattering. This can lead to unique spin dependent phenomena beyond the scope of this thesis.

2.2.4.5 Other Mechanisms

There are many other mechanisms that we did not address here. Most require poor quality samples with different kinds of defects or the fabrication of a heterostructure. For our purposes, they play a diminished role. A few of the more common scatterings are: alloy disorder, neutral impurity scattering, and interface roughness.

2.3 Spin Dynamics

Although spin is inherently quantum mechanical, we are able to very accurately describe ensemble measurements using classical equations of motion. Experiments

dating back to the first observations of the Hanle effect (ca. 1924) and before implied that a collection of magnetic moments were precessing and dephasing due to an applied magnetic field. It feels contradictory to think of a two state system as precessing continuously, but we can map the quantum behavior onto a continuum by thinking in terms of probabilities.

For a single spin, we will only ever measure two states: up or down. We can think of the probability for the spin to transition between states as continuously evolving over time, dependent upon external perturbations. If we can prepare a spin in a known state with controlled perturbations, then repeatedly measure its state at a later time, we can map out the expected measurement as a function of time. If we probe an ensemble of many independent spins, then we will essentially be performing many independent measurements of the later spin states as a function of time, leading to continuum-like signal. In this way, we can observe, on average, classical behavior. Rabi oscillations are a prime example of the success in such thinking where the probability of being in a given state oscillates dependent upon the strength and frequency of an applied field.[29]

Figure 2.4 shows a simple spherical geometry used to represent spin dynamics, commonly referred to as the Bloch sphere. Experimental demonstrations have repeatedly shown that β and ϕ can be used as real parameters to extract meaningful behavior. Two unique uses are control of an initial phase offset in β and ϕ (what we call β_0 and ϕ_0 respectively) for the determination of the sign of the Lande g-factor in GaAsBi and the study of current induced spin polarization.[30, 31]

2.3.1 Bloch-Torrey Equations

The governing differential equations for spin dynamics were derived empirically and are commonly known as the Bloch-Torrey equations. They describe a magnetic dipole moment experiencing a torque from an applied field with some decay

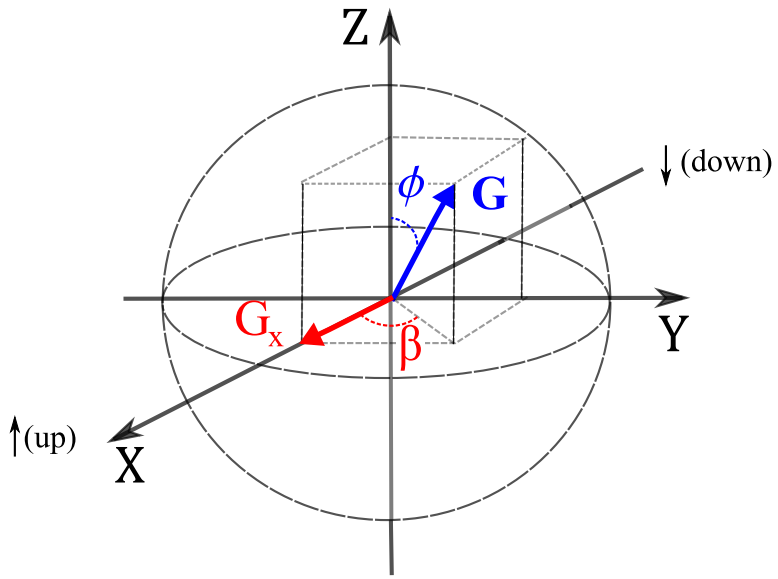

Figure 2.4: Spherical geometry of the spin density vector. $\boldsymbol{G}$ is the unit Green's function vector solution, with G_X being the measured component. The angles ϕ and β account for the orientation of the unit vector.

in amplitude over time. Felix Bloch formalized the theory in two 1946 papers, including an experimental demonstration of nuclear magnetic resonance in condensed matter.[32, 33] Ten years later, H. C. Torrey generalized the equations by incorporating diffusion.[34] A more modern route has been taken in a 2003 paper (Ref. [28]) to derive Bloch-Torrey like equations from first principles using the semi-classical Boltzmann equation. With this method, the quantum mechanical behavior of spins is mathematically connected to a very classical seeming function.

A generalized form of the Bloch-Torrey equations is

$$\frac{\partial \boldsymbol{S}}{\partial t} - \boldsymbol{\Omega} \times \boldsymbol{S} + \frac{1}{\mathbb{T}}\boldsymbol{S} - \nabla \cdot [\mathbb{D}\nabla \boldsymbol{S} - \boldsymbol{v}_d \boldsymbol{S}] = \boldsymbol{F}(t, \boldsymbol{r}) \tag{2.27}$$

where $\boldsymbol{S}$ is the spin density vector, $\boldsymbol{\Omega}$ is the Larmor precession frequency, $\mathbb{T}$ is the dephasing tensor, $\mathbb{D}$ is the diffusion tensor, $\boldsymbol{v}_d$ is the drift velocity of the electrons, and $\boldsymbol{F}(t, \boldsymbol{r})$ is a forcing function. The gradient operators act on position only and it is assumed that each component of each spin and velocity vector is a scalar function of

position. This form accounts for asymmetric drift, asymmetric diffusion, asymmetric dephasing, precession, and forcing.

2.3.2 The Green's Function Solution To Spin Dynamics

We do not require the inclusion of drift or diffusion for later discussion so we can limit ourselves to the simplicity of the 1946 Bloch equations. We further ease our burden by assuming isotropic spin dephasing—if we assume an isotropic band structure, why not? This holds well enough to describe many experimental results. For the interested reader, the effects of anisotropic spin dephasing are discussed in Refs. [35, 36, 31]. We also choose a Dirac-delta as our forcing function so that we may solve for the Green's function. Our simplified governing differential equation is

$$\frac{\partial \boldsymbol{G}}{\partial t} - \boldsymbol{\Omega} \times \boldsymbol{G} + \frac{1}{\tau_s}\boldsymbol{G} = \widehat{\boldsymbol{G_0}}\delta\left(t\right) \tag{2.28}$$

where $\boldsymbol{G}$ is the Green's function, $\widehat{\boldsymbol{G_0}}$ is a normalized initial orientation, and the Larmor precession frequency can be written as

$$\boldsymbol{\Omega} = \frac{\mu_B g \boldsymbol{B}}{\hbar} \tag{2.29}$$

where g is the Lande g-factor.[11]

Using spherical geometry (see Fig. 2.4), we can define the initial orientation using only two angles where at time 0, $\beta = \beta_0$, and $\phi = \phi_0$. We usually assume ϕ does not evolve with time.

$$\widehat{\boldsymbol{G_0}} = \langle \cos\beta_0 \sin\phi_0, \sin\beta_0 \sin\phi_0, \cos\phi_0 \rangle \tag{2.30}$$

Orienting $\boldsymbol{B}$ in the z-direction, setting $\beta = \Omega t + \beta_0$, and measuring along the x-direction, we arrive at

$$G_X = \mathbb{H}\left(t\right) e^{-t/\tau_s} \sin\phi_0 \cos\left(\Omega t + \beta_0\right) \tag{2.31}$$

where $\mathbb{H}$ is the Heaviside step function. Equation 2.31 is what we base all of our experiment analysis upon using τ_s to encompass all relevant spin scattering mechanisms and Ω to account for precession of the electron spin ensembles. It is worth mentioning that the appearance of τ_s in the differential equation can be derived from using the relaxation time approximation in the semi-classical Boltzmann equation.

2.3.2.1 Applicability of The Model

We should also note that this functional form is not restricted to spins in semiconductors—although one might have guessed that already. We have hidden all mention of whatever material system we might be working with in the g-factor and dephasing time τ_s. In this way, we can think of the vast majority of spin measurements as probing a gas of spins that behave differently in different containers. We should note that spin, though a property of an electron and attached to its movement, can change independently. This is similar to the rotation speed of a planet being independent of its orbit. This allows for spin waves and other unique phenomena to exist, whereby an electron can be stationary but the spin changes with time. If we reincorporate diffusion to our model, we would find that there is also a *spin* diffusion length, independent of the charge diffusion length as polarization can be scrambled as an electron bounces through a material. We ignore all these interesting things as higher order corrections, unnecessary for the simplest forms of the experiments we will discuss. However, it is these very same measurement systems, when combined with samples that are biased, strained or otherwise, that can extract data on such behavior. The resulting tweaks to 2.31 are fairly straightforward.

2.3.3 Spin Dephasing

We have said that we are at the bottom of the conduction band where $\boldsymbol{k} = 0$. It turns out that the optical transitions we will use to perform measurements will impart

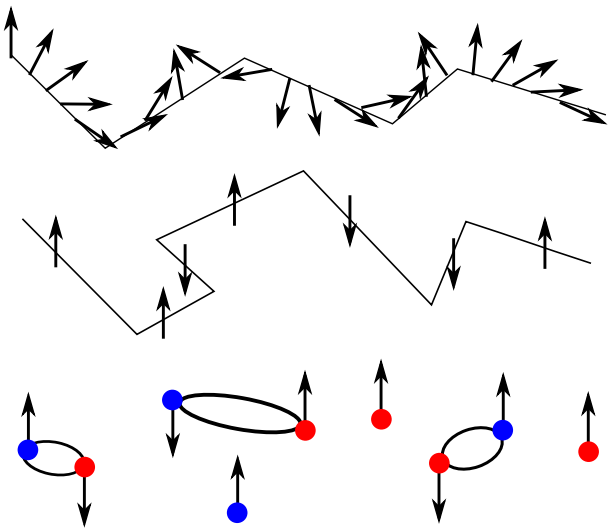

Figure 2.5: The dephasing mechanisms are represented schematically. From top to bottom: D'yakanov-Perel, Elliot-Yafet, and Bir-Aranov-Pikus

negligible momentum (Sec.2.3.4). It is a fair question to ask, "Why should we care about scattering?" Quantum mechanics has built into it, an uncertainty principle—we never really know the exact position and momentum of ourselves or anything else. On top of that, electrons are Fermions implying that only two (one spin up and one spin down) of the $\sim 10^{13}$ to 10^{19} carriers/cm^3 can ever have a $\boldsymbol{k}$ value of 0, even in the ground state. Classical mechanics also says that finite temperature implies finite movement. Therefore, with actual materials at finite temperature, nearly every electron spin is slightly away from $\boldsymbol{k} = 0$.

The electrons will explore momentum space within their allowed portion of dispersion, and in doing so, undergo scattering. The rate and type of momentum scattering determines how quickly the ensemble spin polarization becomes scrambled, or *dephased*. We can think of each electron's spin polarization as having some relative angle (or phase) with all the other electron spins. If that phase changes, the overall polarization will change as well. We will discuss three main dephasing mechanisms and give citations for the interested reader to study their derivation.

2.3.3.1 D'yakanov-Perel

We know from our discussion of spin orbit coupling that electrons experience an effective magnetic field as they move through the lattice. This can be a pronounced effect when the lattice is made up of two different kinds of atoms. In 1972, M. I. D'yakonov and V. Perel published a theory for spin ensemble dephasing based on the spin orbit field of a non-centrosymmetric semiconductor.[37] In short, moving one way in a unit cell of GaAs is not the same as moving another way. This means that spins will experience different effective magnetic fields dependent on their direction of travel and that the orthogonal component of the spin will precess about the field they experience.

If the spins could continue moving along a straight path indefinitely, dephasing would not occur. Instead, there would be beating of the polarization signal dependent upon the average velocity and the periodicity of the lattice. In order to randomize the spin polarization, scattering of some kind must occur. Subsequent scattering events will randomize the electron's movement through the lattice. This introduces random phase shifts from random amounts of precession between scattering.

In an interesting twist, if the momentum scattering time is significantly shorter than a single period of precession, the dephasing is minimized. This is defined as "motional narrowing" where the randomized effects from carrier movement are quickly averaged, leading to much longer dephasing times. This has the counter-intuitive result that a bad crystal with lots of defects for momentum scattering, can minimize spin dephasing from the D'yakanov-Perel mechanism.

We list two limiting cases where the momentum scattering time is τ_p, and the Larmor precession frequency Ω is momentum dependent with some distribution $\Delta\Omega$.[11] In the first case, a spin ensemble can make a full precession prior to a momentum

scattering event which leads to dephasing dependent upon $\Delta\Omega$

$$\tau_p \Omega_{avg} \gtrsim 1 \rightarrow \frac{1}{\tau_s} \approx \Delta\Omega \tag{2.32}$$

In the second case, momentum scattering is very rapid leading to motional narrowing, with the dephasing time depending upon the product of the mean square of the precession frequency and the momentum scattering time

$$\tau_p \Omega_{avg} \lesssim 1 \rightarrow \frac{1}{\tau_s} \approx \Omega_{avg}^2 \tau_p \tag{2.33}$$

2.3.3.2 Elliot-Yafet

In 1954, R. J. Elliot published work showing that the spin orbit field could lead to dephasing in a centrosymmetric material if momentum scattering were present.[38] Spin orbit coupling is a perturbation of the simple rigid lattice bandstructure solutions and therefore mixes those Bloch states. Elliot considered the case where the mixed states were degenerate in energy but could have the same momenta. Therefore, a momentum scattering event could lead to a spin flip, even if the momenta remained the same after scattering. In 1963, Y. Yafet explored the role of scattering from phonons—another way to change momentum, yielding a more complete picture.[39]

The main results are the Elliot and Yafet relations. The Elliot relation gives an order of magnitude estimate for the dephasing rate, while the Yafet relation highlights the qualitative temperature dependence by noting $\frac{1}{\tau_p(T)} \sim \rho(T)$ where T is the temperature and τ_p the momentum relaxation time. The relations are summarized as

$$\frac{1}{\tau_s} \simeq \frac{(g_0 - g)^2}{\tau_p} \sim (g_0 - g)^2 \rho(T) \tag{2.34}$$

where g_0 is the free electron g-factor and g the effective g-factor. The key distinction between the D'yakonov-Perel and Elliot-Yafet mechanisms is their opposite relation-

ship with momentum scattering.[11]

2.3.3.3 Bir-Aranov-Pikus

The Bir-Aranov-Pikus (BAP) mechanism is the dephasing of spins through an exchange interaction between electrons and holes.[40, 41] It is primarily found in p-type materials as it requires sufficient overlap between the electron and hole wavefunctions to be effective. The exchange interaction has to do with the symmetry operations of a wavefunction made up of indistinguishable particles. As we have mentioned before, a hole is a pseudoparticle that really represents a *missing* electron from a collection of many electrons. Since electrons are Fermions, the exchange interaction must be antisymmetric. This leads to a spin flip where the spin of the electron in the conduction band is exchanged with the spin of the hole. One could think of a spin up electron going back to the valence band while a spin down electron is promoted.

In GaAs, holes undergo rapid momentum scattering and typically dephase orders of magnitude faster than electrons in the conduction band.[42] In n-type materials, there are also very few holes to interact with as the equilibrium state of the material is to have a full valence band with many free conduction electrons. The BAP mechanism typically plays a small role.

2.3.4 Spin Dependent Optical Selection Rules

We want to probe the spin behavior optically, but this is only possible if there are spin selective optical transitions. As we saw with our development of band theory, spin plays a significant role so it is fair to assume we have something to work with.

We begin by noting that for the tight binding model, we used the atomic wavefunctions as a basis to develop our bands. We also note that our assumption from the $\boldsymbol{k} \cdot \boldsymbol{p}$ model was that most of the interesting things happen at the bottom of the band and the dispersion is approximated to be quadratic in momentum. For GaAs

and other direct gap semiconductors, this means that we are centered about $\boldsymbol{k} = 0$. Light imparts negligible momentum to an excited electron so we can further simplify our view to just $\boldsymbol{k} = 0$. In short, we are working with atomic like transitions that have been shifted in energy and we can ignore any role of momentum. This is not the case for indirect gap materials, but we will ignore that for now.

For GaAs, the conduction band is s-like and the valence band is p-like. We further assume that transitions to the conduction band are isotropic, which about the Γ-point is a very good approximation. By noting that electric dipole transitions are proportional to

$$\langle \psi_f | \, \boldsymbol{p} \, | \psi_i \rangle \tag{2.35}$$

where ψ_i and ψ_f are initial and final states respectively, we can write

$$\langle p_x | \, p_x \, | s \rangle = \langle p_y | \, p_y \, | s \rangle = \langle p_z | \, p_z \, | s \rangle \tag{2.36}$$

Using the notation of Ref. [24] where the kets $|j, m_j\rangle$ are written in terms of total angular momentum j and the z-component m_j, we expand the heavy and light hole states in terms of linear momenta p and spin states represented by arrows. The heavy hole states are

$$\begin{aligned} \left|\tfrac{3}{2}, \tfrac{3}{2}\right\rangle &= \tfrac{-1}{\sqrt{2}} \left(|p_x\rangle + i \, |p_y\rangle \right) \uparrow \\ \left|\tfrac{3}{2}, \tfrac{-3}{2}\right\rangle &= \tfrac{1}{\sqrt{2}} \left(|p_x\rangle - i \, |p_y\rangle \right) \downarrow \end{aligned} \tag{2.37}$$

The light hole states are

$$\begin{aligned} \left|\tfrac{3}{2}, \tfrac{1}{2}\right\rangle &= \tfrac{-1}{\sqrt{6}} \left[\left(|p_x\rangle + i \, |p_y\rangle \right) \downarrow - 2 \, |p_z\rangle \uparrow \right] \\ \left|\tfrac{3}{2}, \tfrac{-1}{2}\right\rangle &= \tfrac{1}{\sqrt{6}} \left[\left(|p_x\rangle - i \, |p_y\rangle \right) \uparrow + 2 \, |p_z\rangle \downarrow \right] \end{aligned} \tag{2.38}$$

We can see that the holes are eigenstates of a circular polarization basis with

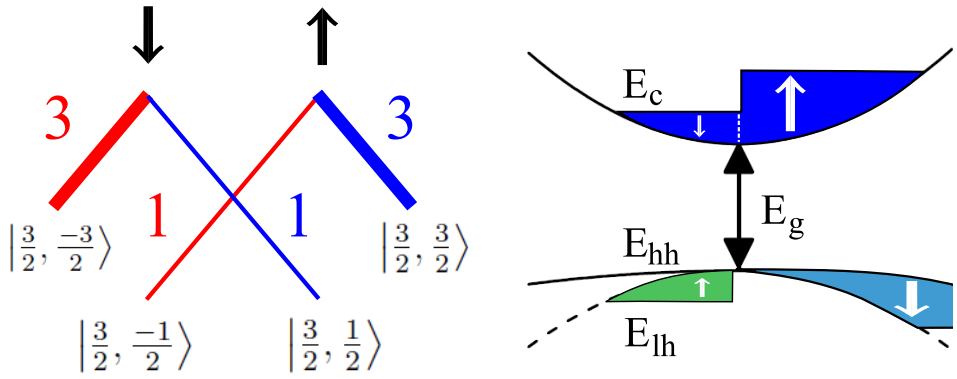

Figure 2.6: (left) Direct Gap Optical Selection Rules for circularly polarized light. (right) Schematic of spin polarization in the different bands immediately after a σ_+ transition. The hole polarization typically dephases on very short time scales and is neglected in most analysis. `Red = σ+, blue = σ−, numbers and line thicknesses indicate the relative probability of the optical transitions`

operators of the form

$$\sigma_+ = \frac{p_x + ip_y}{\sqrt{2}} \tag{2.39}$$

$$\sigma_- = \frac{p_x - ip_y}{\sqrt{2}} \tag{2.40}$$

Evaluating transitions from the hole states to the conduction band defined by $|\Phi_c\rangle$ and using the approximation $p_x = p_y = p_z = p$ we get

$$\begin{aligned} \left\langle \tfrac{3}{2}, \tfrac{3}{2} \right| \sigma_+ \left|\Phi_c\right\rangle &= \left\langle p\right| p \left|\Phi_c\right\rangle \uparrow \\ \left\langle \tfrac{3}{2}, \tfrac{1}{2} \right| \sigma_+ \left|\Phi_c\right\rangle &= \tfrac{-1}{\sqrt{3}} \left\langle p\right| p \left|\Phi_c\right\rangle \downarrow \end{aligned} \tag{2.41}$$

for σ_+ polarized transitions and

$$\begin{aligned} \left\langle \tfrac{3}{2}, \tfrac{-3}{2} \right| \sigma_+ \left|\Phi_c\right\rangle &= -\left\langle p\right| p \left|\Phi_c\right\rangle \downarrow \\ \left\langle \tfrac{3}{2}, \tfrac{-1}{2} \right| \sigma_+ \left|\Phi_c\right\rangle &= \tfrac{1}{\sqrt{3}} \left\langle p\right| p \left|\Phi_c\right\rangle \uparrow \end{aligned} \tag{2.42}$$

for σ_- polarized transitions with all other matrix elements being 0. We are left with a 3:1 ratio of up:down or down:up conduction electron spins, dependent upon the choice of circular polarization of incident light. The valence band is also polarized with opposite polarizations in the heavy hole and light hole bands. However, as we discussed before, it is common for the hole polarizations to rapidly dephase. Hole spins are typically disregarded from measurement analysis, but can be accessed through the same type of measurements discussed in Ch. IV. We can now probe spins through polarized photoluminescence (PL) or spin selective differential absorption.

2.3.5 Faraday and Kerr Rotation

Faraday and Kerr Rotation are essentially the same physical phenomena: the rotation of the linear polarization of a beam of light after transmission through (Faraday) or reflection from (Kerr) a magnetized material. The original experiments by Michael Faraday and John Kerr were conducted in the 1840s and 1870s respectively. Spins are magnetic moments and if they are polarized, the sample is magnetized. The underlying mechanism for the rotation is a difference in the circular indexes of refraction based on the difference in absorption for σ_+ and σ_- polarized light of a probe beam. Linear polarization is equal parts σ_+ and σ_-, so differential absorption should lead to an ellipticity in the probe beam after interaction. However, if the absorption is a small enough percentage of the beam that we can ignore losses, we can approximate the effect as a rotation of the linear polarization.[43]

We can describe Faraday rotation using the Jones vector formulation (see Appendix A).[44] We start by decomposing a linearly polarized incident ray into its circularly polarized components

$$\boldsymbol{E}_i = E_0 e^{i\varphi} \begin{pmatrix} 1 \\ 0 \end{pmatrix} = E_0 e^{i\varphi} \frac{\sqrt{2}}{2} \left[\frac{1}{\sqrt{2}} \begin{pmatrix} 1 \\ i \end{pmatrix} + \frac{1}{\sqrt{2}} \begin{pmatrix} 1 \\ -i \end{pmatrix} \right] \tag{2.43}$$

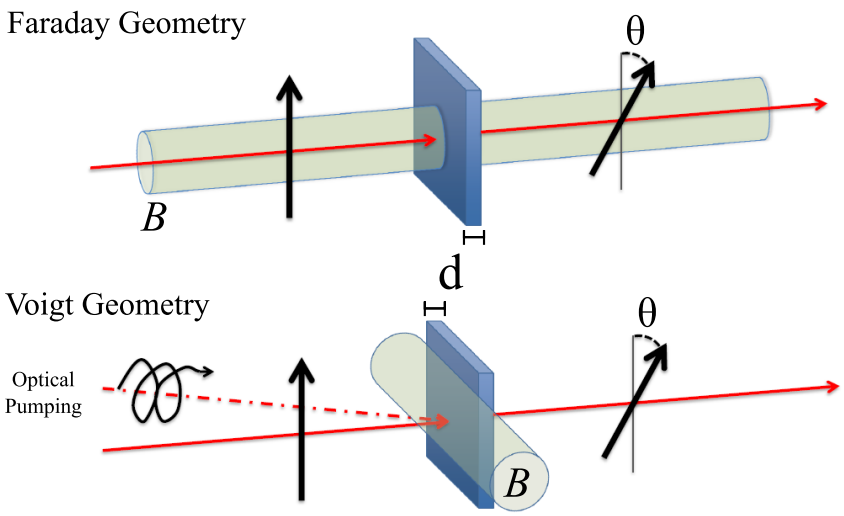

Figure 2.7: Faraday Rotation Experiment Geometries. The blue rectangular box represents a sample of thickness d. The red line is the optical path with an arrowhead indicating direction of propagation. B is the applied magnetic field with orientation represented schematically by a green cylinder. θ is the angle of rotation that a linear polarization (black arrow) undergoes after passing through the sample.

Initially both circularly components have the same phase. If we assume negligible losses, when the components pass through a material, they each pick up a new phase based on their respective circular indexes of refraction, n_+ and n_-. The amount of the phase shift $\Delta\varphi$ will depend upon the effective path length of the light d, the wavevector amplitude in the direction of propagation k, and the respective indexes of refraction. We arrive at

$$\Delta\varphi_\pm = n_\pm kd \tag{2.44}$$

If we define θ as half of the relative phase shift between the two components, we can write down the phase shifts as

$$\Delta\varphi_\pm = \frac{(n_+ + n_-)\,kd}{2} \pm \frac{(n_+ - n_-)\,kd}{2} \tag{2.45}$$

$$= \frac{(n_+ + n_-)\,kd}{2} \pm \theta \tag{2.46}$$

The final polarization state is then

$$\boldsymbol{E}_f = E_0 e^{i\left(\varphi + \frac{(n_+ + n_-)kd}{2}\right)} \frac{\sqrt{2}}{2} \left[e^{i\theta} \frac{1}{\sqrt{2}} \begin{pmatrix} 1 \\ i \end{pmatrix} + e^{-i\theta} \frac{1}{\sqrt{2}} \begin{pmatrix} 1 \\ -i \end{pmatrix} \right] \tag{2.47}$$

Using trigonometric identities, we can write Eq. 2.47 as

$$\boldsymbol{E}_f = E_0 e^{i\left(\varphi + \frac{(n_+ + n_-)kd}{2}\right)} \begin{pmatrix} \cos\theta & \sin\theta \\ -\sin\theta & \cos\theta \end{pmatrix} \begin{pmatrix} 1 \\ 0 \end{pmatrix} \tag{2.48}$$

This is the rotation of a linear polarization with an overall complex phase. Since our measurements are restricted to intensities, we can ignore the constant phase factor.

2.3.5.1 Verdet Coefficient vs. Faraday Cross Section

The amount of rotation θ has been experimentally shown to be linear in the amount of magnetization of most materials. However, there is more than one way to magnetize a material. When Faraday first performed his experiment, he magnetized a sample using a magnetic field. In this way, he reoriented the orbital angular momentum, as well as the spin angular momentum, along the magnetic field lines. The optical rotation he measured has been shown to be proportional to the Verdet coefficient V where

$$\theta = V d \frac{B}{\mu_0} \tag{2.49}$$

with B the applied magnetic field strength, d the thickness of the material, and μ_0 the vacuum permeability.[43]

The majority of our experiments are performed in the Voigt or transverse field geometry (see Fig. 2.7) and we do not polarize the material along the optical path.

In this case, the appropriate scaling comes from the Faraday cross section σ_F where

$$\theta = \sigma_F S d \tag{2.50}$$

with S the spin polarization density and d the same as before.[45] The theory is relatively new (published in 2012) and few measurements have been attempted to directly test the predictions. However, σ_F holds promise as a useful material parameter with guidance for future spintronic engineering.

2.3.5.2 Kramers-Kronig Relations

We would like to quantitatively relate the differential absorption we expect from polarizing spins to the differential index of refraction we measure. We can write down relationships between the complex wavevector $\widetilde{k}$, the complex susceptibility $\widetilde{\chi}$, the index of refraction n, and the absorption coefficient α as follows:[46]

$$\widetilde{k} = \frac{\omega}{c}\sqrt{1+\widetilde{\chi}} \tag{2.51}$$

$$\widetilde{k} = k + 2i\alpha \tag{2.52}$$

$$n = \frac{c}{\omega}k \tag{2.53}$$

For a three-dimensional system, the density of states should go as $(E - E_g)^{1/2}$ where E_g is the bandgap. Combining that behavior piecewise with an exponential function representing the Urbach tail gives us a model for absorption.[47] If we assume $1 \gg \widetilde{\chi}$ then we can Taylor expand the square root and get:

$$n = 1 + Re\left\{\widetilde{\chi}\right\} \tag{2.54}$$

$$\alpha = \frac{\omega}{2c} Im\left\{\widetilde{\chi}\right\} \tag{2.55}$$

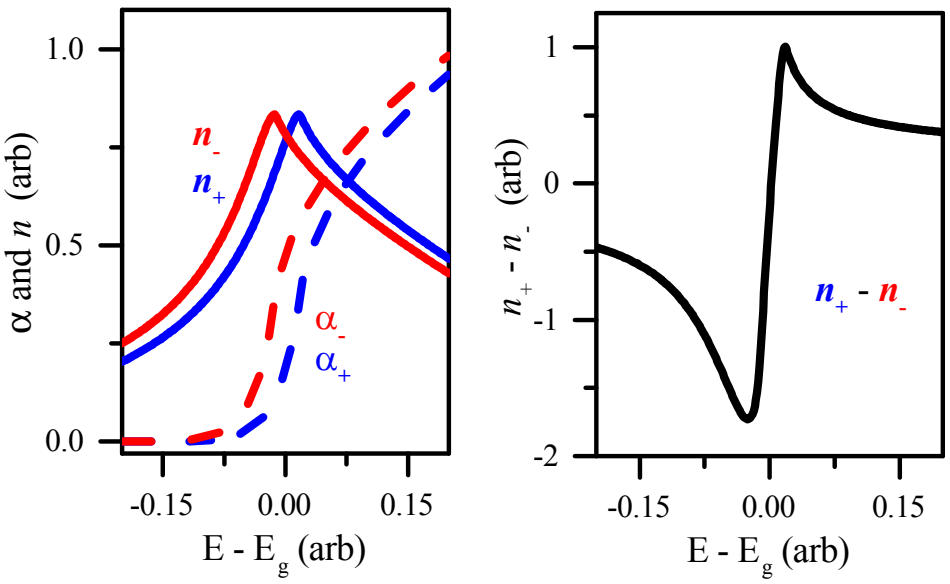

Figure 2.8: (left) Model of absorption spectra and index of refraction behavior. $\alpha_{\pm}$ and $n_{\pm}$ are the circular absorption coefficients and indexes of refraction respectively. (right) Differential circular refractive index dependence upon energy.

We should mention that the Taylor expansion assumption is acceptable for dilute gasses but a bit of a stretch for GaAs. We will use it for qualitative analysis a little bit later.

Our goal now is to relate the real and imaginary parts of $\widetilde{\chi}$ so we can use what we know about α. Expressions for this very purpose exist and are called the Kramers-Kronig relations:[25]

$$Re\left\{\widetilde{\chi}\left(\omega\right)\right\} = \frac{2}{\pi} P \int_0^{\infty} ds \frac{s\, Im\left\{\widetilde{\chi}\left(s\right)\right\}}{s^2 - \omega^2} \tag{2.56}$$

$$Im\left\{\widetilde{\chi}\left(\omega\right)\right\} = \frac{-2\omega}{\pi} P \int_0^{\infty} ds \frac{Re\left\{\widetilde{\chi}\left(s\right)\right\}}{s^2 - \omega^2} \tag{2.57}$$

where P means take the Cauchy principal part of the integral. A figure depicting differential absorption and the associated differential index of refraction using this model is shown in figure 2.8.

CHAPTER III

Manipulating, Detecting, and Recording Optical Polarization

In Chapter VII, we will discuss a novel optical spin measurement technique. We must understand the behavior of available equipment prior to discussing the design of such an experiment. Therefore, in this chapter, we discuss how to manipulate and detect the polarization of light, along with the types of electronic devices used to process the resultant information. The sections are organized as follows: light sources (Sec. 3.1), manipulating and detecting light polarization (Sec. 3.2), conventional analog electronic processing (Sec. 3.3), and analog to digital conversion (Sec. 3.4).

3.1 Light Sources

We primarily treat light as a classical wave, though we note that light comes in discrete quanta called "photons." There are two asymptotic types of light sources: coherent (the electromagnetic field has a predictable phase for temporal and spatial evolution) or incoherent (the electromagnetic field has a random phase for temporal and spatial evolution). There are also two asymptotic types of light polarization: polarized (the electromagnetic field has a predictable temporal and spatial orientation), and random (the temporal and spatial orientation is not predictable).

3.1.1 Coherence and Polarization

In general, there is a varying degree of coherence, dependent upon the source. We can describe regions where we can approximate a source as coherent with values for a coherence length and time, respectively. Coherence is the key to interference in that controlled manipulations of the relative phase between two or more wavefronts is possible. We will exploit this fact shortly. Further development of the concept of coherence is beyond the scope of this dissertation. We recommend Ref. [44] for the interested reader.

Beyond coherence, light can be polarized, where the orientation of the electric field follows a predictable temporal and spatial evolution—a fact that we have already used with optical selection rules. Similarly, we can have randomly polarized light with random electric field orientation. It is common to define polarization in terms of the orientation of the electric field vector alone, and we do so as well.

Polarization and coherence are not entirely separate entities. We are able to manipulate the polarization of light independent of the coherence of the source. However, only light of the same polarization will lead to interference while randomly polarized light must be incoherent by our definitions. It is worth noting that the interface of polarization and coherence of light is an area of active research and that our above definitions are too primitive for certain cases.[48] For our purposes, they will suffice.

3.1.2 Laser Light Sources

Lasers are nearly coherent light sources and can be broken down into two broad categories: continuous wave (CW) and pulsed. The key aspect leading to coherence in lasers is stimulated emission, whereby subsequent transitions are induced by passing photons of approximately the same energy. Lasers are often polarized with the stimulating photon helping determine the emitted photon's polarization state. All of our pump sources will be lasers. Our probes will be lasers that are nearly coherent

or PL whose coherence depends upon the state of the sample.

High quality CW lasers can approach the single wavelength idealization making them very useful for extracting precise energy dependent information. They also have extremely high spatial and temporal coherence allowing for sensitive interferometry experiments. Pulsed lasers are broad in the energy spectra but can achieve very short pulse widths in time ($\lesssim$1 ps for many modern systems). Pulsed laser systems are said to have a short coherence time while retaining high spatial coherence.

The energy broadening of a pulsed laser can be traced to a superposition of interfering sinusoids. A titanium-sapphire (Ti:Saph) pulsed laser, used in the experiments of the later chapters, works on the principle of "mode-locking," which is the coherent interference of sinusoids with a distribution of frequencies that maintain a fixed phase relationship. As the sinusoids evolve in time, they periodically all have the same modulo 2π phase. The frequency of the pulsing depends upon the laser cavity length and the range of available lasing frequencies. The broader the range of frequencies used, the narrower the pulse width in time. An excellent resource for those interested in lasers is Ref. [49].

3.2 Manipulating and Detecting The Polarization of Light

Optical access to spin dynamics comes from spin dependent selection rules (see Sec. 2.3.4) where we can "pump" a spin polarization through an appropriate polarization of incident absorbed light, then "probe" that spin polarization through radiative recombination along the same pathways or through the differential index of refraction of a probe laser. An alternative to pumping is to make use of spin *noise*, the random orientation of spin polarization. We will assume that we have the appropriate optical access (decidedly the case for GaAs).

3.2.1 Manipulating Polarization

In order to pump or probe spin polarizations, we need to be able to control the polarization of light. Our assumed range of operation is that of a Ti:Saph laser (710 nm - 980 nm) putting us in the near infrared. There are many convenient materials in this regime for the fabrication of optical polarizers and waveplates so apparatus are straightforward to purchase and assemble. We only need three elemental components in order to perform our experiments and they are: a 1/4-waveplate, a 1/2-waveplate, and a linear polarizer. As the names imply, a 1/4-waveplate imparts a 1/4-wave relative retardance between the two orthogonal components, while a 1/2-waveplate introduces a 1/2-wave shift.

Waveplates are made from materials where the *linear* index of refraction is different for one axis compared to the other. Such materials are said to have *linear birefringence*, which allows one polarization of light to travel *faster* than the other through the material—hence "fast" and "slow" axes. Waveplates are fixed at the time of manufacture, while variable retarders and photo-elastic modulators are continuously tunable over some range. Tunability requires exploitation of various material systems, such as liquid crystals, but the end goal is the same—linear birefringence. We can substitute a single electro-optic component such as a retarder or modulator for the waveplates reducing our required number of elemental components to two.

By combining the components in the proper order, we can change and analyze the polarization of light as we desire. Linear and circular polarizations of light are special cases. Elliptical polarization is the general case where the relative phase between orthogonal electric field components is not an integer multiple of $\pi/4$. In order to extract the exact polarization of light, all four Stokes parameters must be measured.[50] We will assume that we are only working with the special cases of circular and linear polarization. A collection of schematics showing combinations of optics for polarization modification can be found in Fig. 3.1. The polarized light

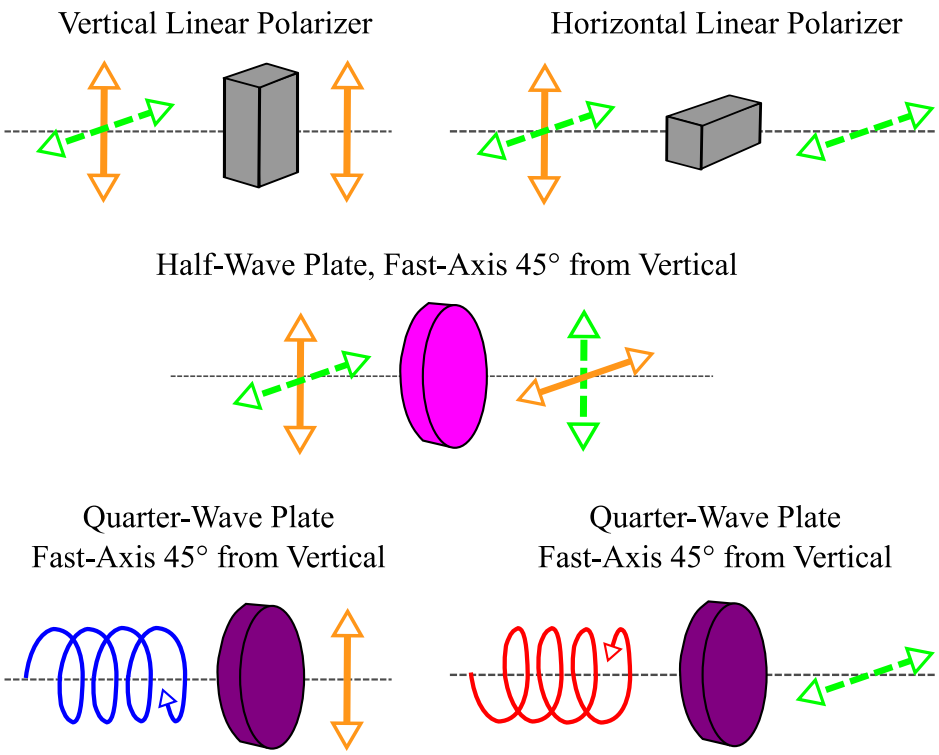

Figure 3.1: Schematics of the behavior of various optical polarization elements: (top) Vertical and horizontal linear polarizers. (middle) Half-wave plate acting on linear polarization. (bottom) Quarter-wave plates acting on left/σ_+ (blue) and right/σ_- (red) circularly polarized incident light.

and optical components can be mathematically represented by the Jones vectors and matrices respectively, found in Appendix A.

3.2.2 Detecting Polarization

As our optical selection rules suggest (see Sec. 2.3.4), PL of direct gap materials will have some emission in the circular polarization basis. We have neglected linearly polarized transitions as they are not spin selective and their magnitude will be canceled out with our detection schemes. The net circular polarization of PL emitted after right circular (σ_+) excitation can be calculated as

$$P = \frac{I_{\sigma_+,\sigma_+} - I_{\sigma_+,\sigma_-}}{I_{\sigma_+,\sigma_+} + I_{\sigma_+,\sigma_-}} \tag{3.1}$$

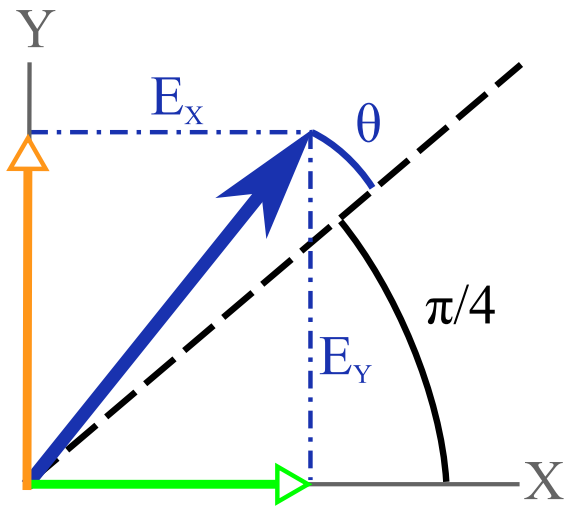

Figure 3.2: Differential rotation measurement of linear polarization. The linear polarization is initially *balanced* with equal amplitude of orthogonal components E_X and E_Y. After passing through a sample, the polarization is rotated by an angle θ which can be related to the new values of E_X and E_Y.

where $I_{j,k}$ is the intensity of k polarized PL from j polarized excitation (see top of Fig. 3.3). With our assumption of isotropic selection rules, we could permute j and k to measure only one polarization of emitted light under differing excitation conditions.

$$P = \frac{I_{\sigma_+,\sigma_+} - I_{\sigma_-,\sigma_+}}{I_{\sigma_+,\sigma_+} + I_{\sigma_-,\sigma_+}} \tag{3.2}$$

In practice, fixing the *incident* polarization can lead to unintended effects such as dynamic nuclear polarization complicating a measurement—unless the effect is desired.[51] Therefore, we use alternating excitation polarizations and Eq. 3.2 for measurement. Evaluation of such data is typically in terms of "percent polarization" as we are working in the circular polarization basis.

For Faraday and Kerr rotation, we have assumed that absorption is negligible when light passes through the sample allowing us to work exclusively in a linear basis. This approximation is quite reasonable for the small rotations we typically measure ($\lesssim 100$

μrad). Using Fig. 3.2, we can see that if we decompose the initial linear polarization onto two orthogonal axes, the rotated polarization involves opposing electric field amplitude changes for the components.

We will be measuring the intensity of the light, but can relate it to the field strength as $I \sim |E|^2$. We can relate the electric field components to the angle θ as

$$E_X = \frac{E_0}{\sqrt{2}} \cos(\theta + \pi/4) \quad , \quad E_Y = \frac{E_0}{\sqrt{2}} \sin(\theta + \pi/4) \tag{3.3}$$

If we perform a differential intensity measurement, similar to what we discussed for PL, then use some trigonometric identities, we get

$$\begin{aligned} \frac{I_Y - I_X}{I_Y + I_X} &= \frac{|E_Y|^2 - |E_X|^2}{|E_Y|^2 + |E_X|^2} && (3.4) \\ &= \sin^2(\theta + \pi/4) - \cos^2(\theta + \pi/4) && (3.5) \\ &= -\cos(2\theta + \pi/2) && (3.6) \\ &= \sin(2\theta) && (3.7) \\ &\simeq 2\theta && (3.8) \end{aligned}$$

where we have used the small angle approximation. Therefore

$$\theta \simeq \frac{1}{2} \left(\frac{I_Y - I_X}{I_Y + I_X} \right) \tag{3.9}$$

We can perform the two measurements of polarization dependent intensity at separate instances in time, as we must for PL, assuming our sample's state remains nearly static for a given set of experiment parameters. However, our efficiency in performing an experiment would be significantly improved if we could measure the two polarizations simultaneously. We will discuss how to make that possible shortly. The excitation and detection schemes for interacting with polarized light are summarized

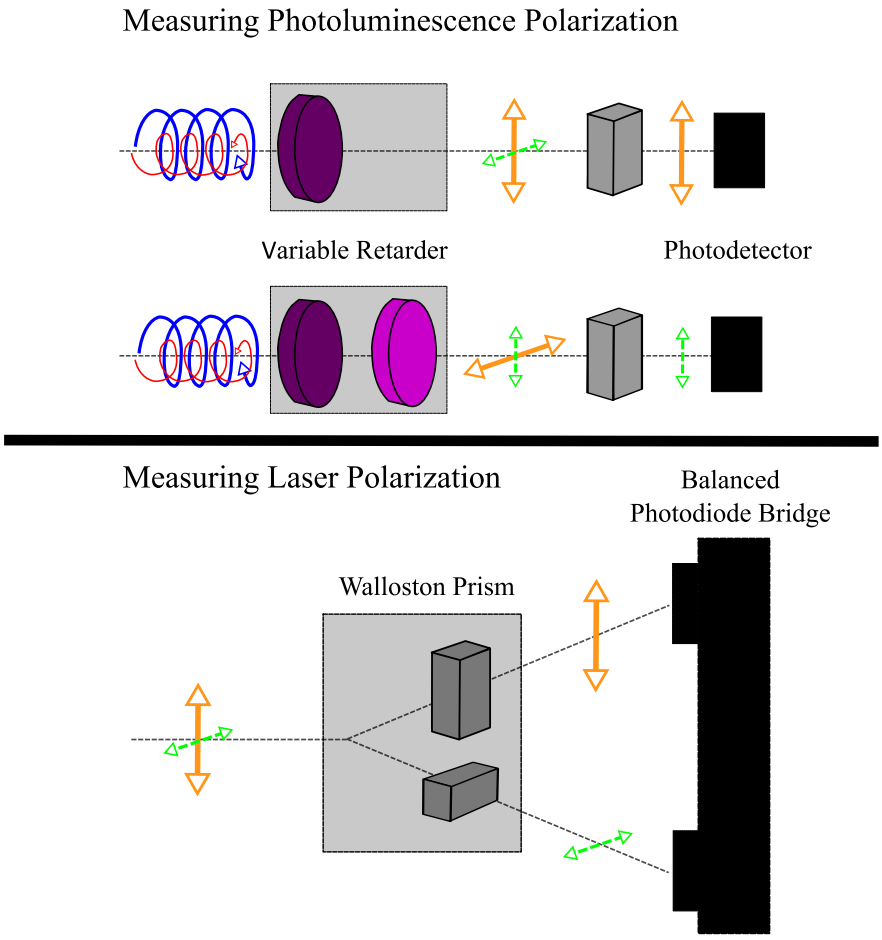

Figure 3.3: (top) Schematic representing the detection of PL polarization assuming a circular polarization basis. A variable retarder switches between $\lambda/4$ and $3\lambda/4$ retardance to switch between the circular and linear polarization bases, along with modulating the resultant linear polarization by $\lambda/2$. (bottom) Schematic representing the detection of the rotation of a linear polarization using a Walloston prism and balanced photo-diode bridge.

schematically in Fig. 3.3.

3.3 Conventional Analog Electronic Processing

There are a variety of photodetectors capable of generating a voltage that is linearly proportional to the incident light intensity. They all work on one relatively simple principle: if a photon's energy is greater than the material's bandedge, an electron will be promoted to the conduction band. Through bandstructure engineering and applied bias, the promoted carrier is swept towards a current or voltage detector and counted. Different devices have varying levels of "quantum efficiency" that gauges the carrier promotion probability, with some reaching near 100%.

As we have seen previously, the desired information is proportional to the *difference* in amplitude between two orthogonal polarizations. If two separate measurements are conducted and recorded, postprocessing requires that subtraction be performed. For very small net polarizations this is problematic, as random fluctuations in the signal, or *noise*, can change the sign of the calculation dependent upon the relative amplitudes. We will discuss below a few options for minimizing the noise.

3.3.1 The Balanced Photo-diode Bridge

Rather than measuring one polarization state, followed by a measurement of the other, the balanced photo-diode bridge (BPD) allows for two orthogonal polarization states to be measured and subtracted simultaneously. The electrical processing, beyond performing the required difference calculation, removes any fluctuation in the difference that is common to both photodiode signals. This is known as common mode rejection and reduces various sources of noise including laser power fluctuations. The full polarization measurement apparatus involves placing a linear polarizing beam splitter, such as a Walloston prism, on the optical path immediately before the BPD (see Fig. 3.3).

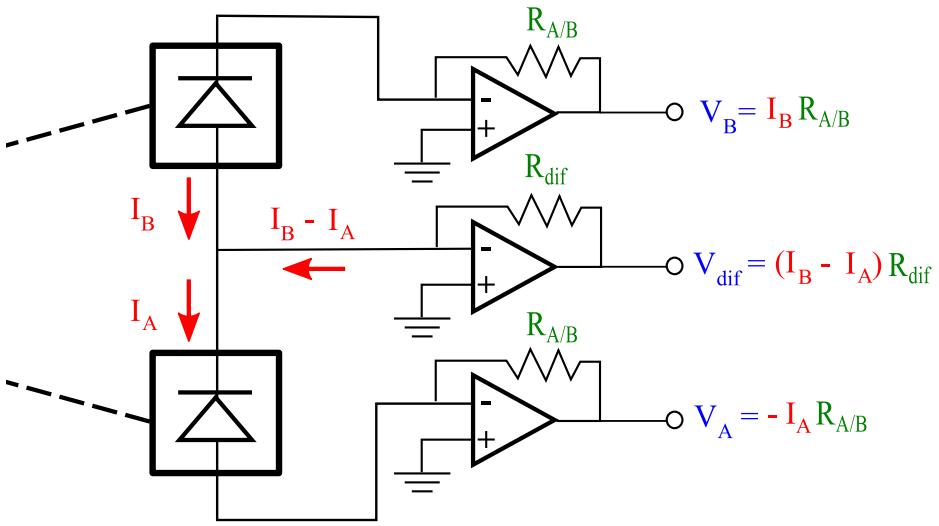

Figure 3.4: Balanced Photo-diode Bridge. The dashed lines represent incident light leading to photo-diodes (squares with diode symbol inside. Electrical currents I are represented by red arrows and traverse the black line wiring of the circuit. The triangles with $\pm$ symbols are op amps arranged for linear amplification and conversion of a current to a voltage. The amplification is dependent upon the choice of resistors R in green. At the right are terminals where voltages (blue) are measured with their respective quantity in terms of I and R.

Each beam is sent to its own photo-diode on the BPD and generates a respective current I_A or I_B. Due to the diode behavior, a difference current forms $(I_A - I_B)$ at their junction (see Fig. 3.4). We can then convert all of the currents into voltages $V_A, V_B,$ and V_{dif} with amplification dependent upon the values of the resistors $R_{A/B}$ and R_{dif}. Measuring the three voltages gives us everything necessary to calculate the probe polarization's angle of rotation.

Performing the difference calculation using analog electronics on the board allows us to achieve high quality "common mode rejection," where the *common* amplitude between the resultant voltages generated by each polarized beam is canceled out. The fewer electronic components between the photodiode and the difference calculation, the fewer sources of noise in the measurement. The amplification allows us to magnify the difference signal for improved resolution. While the BPD design is superior to a single photodiode for measuring relative polarizations, the electronic components and other aspects of the experiment can be noisy enough to prevent detection of sufficiently small signals.

3.3.2 Lock-In Amplifiers

The key concept behind a lock-in amplifier is that noise has different amplitudes for different frequency components, or spectra. If we look at a noisy voltage without spectral resolution, we have essentially integrated over all possible allowed frequencies, or the *bandwidth*, of our instrument. Looking at the spectra directly (see Fig. 3.5), we can see each frequency in our allowed bandwidth is contributing some amplitude to the integral. If we can filter out all but one frequency component, we will have reduced the integrated noise by several orders of magnitude.

Lock-in amplifiers ideally extract the the signal at a given frequency, which is analogous to finding the coefficient of a single Fourier component. This is accomplished in much the same way mathematical calculations do, but with a twist: multiply the

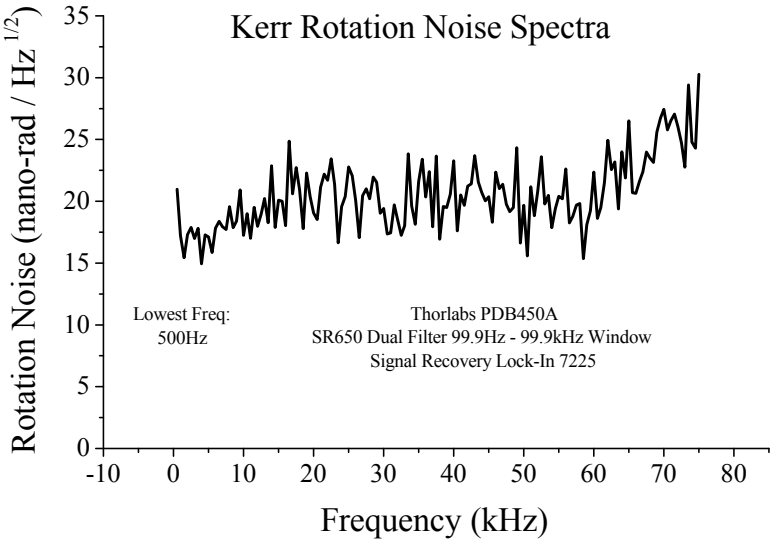

Figure 3.5: Noise spectra scaled assuming a beam splitter cuts the detected power in half from the 200 μW at the sample location. Data was collected in Kerr rotation geometry from an n-GaAs sample at 10 K $\rightarrow$ no spin pumping. Noise should include the contributions from all sources, includng *spin* noise.

input voltage/current by an unit amplitude oscillating reference voltage/current, then apply a low-pass filter.

Through orthogonality of Fourier components, a signal oscillation that matches the reference frequency will yield a constant term.

$$\int_{-\infty}^{\infty} dt A\cos(\omega t)\cos(\omega_0 t) = A\delta_{\omega,\omega_0} \tag{3.10}$$

This is the mapping of any component oscillating at the reference frequency to 0 Hz.

Through realistic electronic behavior, an infinite integral cannot be calculated. We are also contending with a frequency continuum the size of our bandwidth. In general, components of the input are mapped to sum and difference frequencies, through trigonometric identities, relative to the reference.

$$A\cos(\omega t)\cos(\omega_0 t) = \frac{A}{2}\left\{\cos\left[(\omega+\omega_0)\,t\right] + \cos\left[(\omega-\omega_0)\,t\right]\right\} \tag{3.11}$$

By applying a low pass filter, we restrict the possible frequency distribution through bandwidth reduction. In principle, our signal to noise ratio can improve indefinitely through continued reduction of the bandwith, approaching the Fourier integral. In practice, the filtration takes time and there will always be a finite noise signal. Figure 3.6 shows, for a particular implementation of time resolved Kerr rotation, the measured relationship between the mean rotation noise amplitude, three times the error of the mean (EOM), the lock-in filtration time-constant t_c, and the number of measurements N. Rotation noise assumes an error in the difference portion of the calculation for Eq. 3.9 which is directly related to measured voltages. The bandwidth dependent EOM for the rotation measurement goes as

$$EOM = \frac{1}{\sqrt{2\pi t_c}} \frac{\sigma}{N} \sim (N t_c)^{-1/2} \tag{3.12}$$

where σ is the standard deviation per root Hz of the noise amplitude and $1/\sqrt{2\pi t_c}$ is the square root of the bandwidth determined by the lock-in time constant t_c.

3.3.3 Cascaded Lock-Ins

The concept of "locking in" to a signal can be extended to multiple reference frequencies. In this case, a *cascade* of lock-in amplifiers are used where an input signal has been modulated at two or more frequencies. The signal is *demodulated* through subsequent multiplication by reference sinusoids and low pass filtration. There is one important point to the use of cascade lock-ins: the bandwidth reduction must be sequential eliminating the highest frequencies first. In other words, the reduced bandwidth from the first lock-in of the cascade must be large enough to contain the subsequent modulation frequencies, but small enough to eliminate the highest modulation frequency at the time of input.

Beyond noise reduction, one can also use this technique to measure a function and

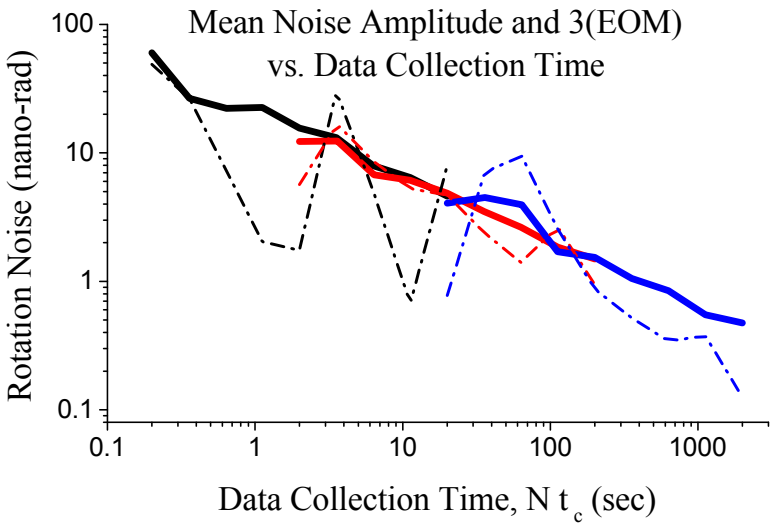

Figure 3.6: Average noise (dashed lines) and 3(EOM) (solid lines) of a particular time resolved Kerr rotation setup. Data was collected in Kerr rotation geometry from an n-GaAs sample at 10 K $\rightarrow$ no spin pumping. Noise should include the contributions from all sources, including *spin* noise. Black $\rightarrow t_c = 0.02$s, Red $\rightarrow t_c = 0.20$s, Blue $\rightarrow t_c = 2.00$s.

its subsequent derivatives simultaneously. This stems from the fact that a lock-in is a *differential* measurement. We must remember that the coefficient of the extracted Fourier component is proportional to the difference of two physical states of the system. We will label the state of the system as $f(x_1, x_2, ...)$ where the x_i are some variables that the state can depend on. As an example, we will limit ourselves to two variables: polarization (P) and magnetic field (B). The amplitude of the Fourier component A from a single lock-in polarization measurement under a constant field can be written as

$$A_1 = f(P_1, B_0) - f(P_0, B_0) \tag{3.13}$$

If we perform a cascaded measurement where we modulate the magnetic field by some amount, our resultant value would be the product of *two* amplitudes. This might be better thought of as extracting a single Fourier component at the sum frequency which involves the multiplication of two sinusoids and their respective amplitudes. The logic

continues for a product of N number of amplitudes if N modulation frequencies and lock-ins are used.

Our final signal from two cascaded lock-ins will go as

$$A_1 A_2 = [f(P_1, B_1) - f(P_0, B_1)] - [f(P_1, B_0) - f(P_0, B_0)] \tag{3.14}$$

We can rewrite the equation in a slightly more familiar form if we say that the difference of function f between the two polarization states yields the net polarization P_{net} at a given applied field.

$$A_1 A_2 = P_{net}(B_1) - P_{net}(B_0) \tag{3.15}$$

If we divide Eq. 3.15 by the difference between the two applied magnetic fields, we get

$$\frac{P_{net}(B_1) - P_{net}(B_0)}{B_1 - B_0} \simeq \left.\frac{\partial P_{net}}{\partial B}\right|_{B=B_0} \tag{3.16}$$

If we modulated the modulation of the magnetic field (i.e. modulate the value where we evaluate the derivative) then we would be able to get the second derivative of the net polarization as a function of magnetic field. We could choose to modulate with some other variable (pump laser intensity, etc.) and get a mixed partial second derivative.

Figure 3.7 shows an odd-Lorentzian, indicative of a Hanle effect measurement with an initial spin polarization in a plane parallel to the sample surface. The figure also shows the derivative with respect to applied magnetic field. The sample was an InGaAs eplilayer where alternating in-plane spin polarizations were generated using Current Induced Spin Polarization (CISP) from a $\sim$1 kHz modulated applied voltage.[31, 51] The applied magnetic field was modulated about a central value at $\sim$1 Hz allowing for the cascaded lock-in measurement.

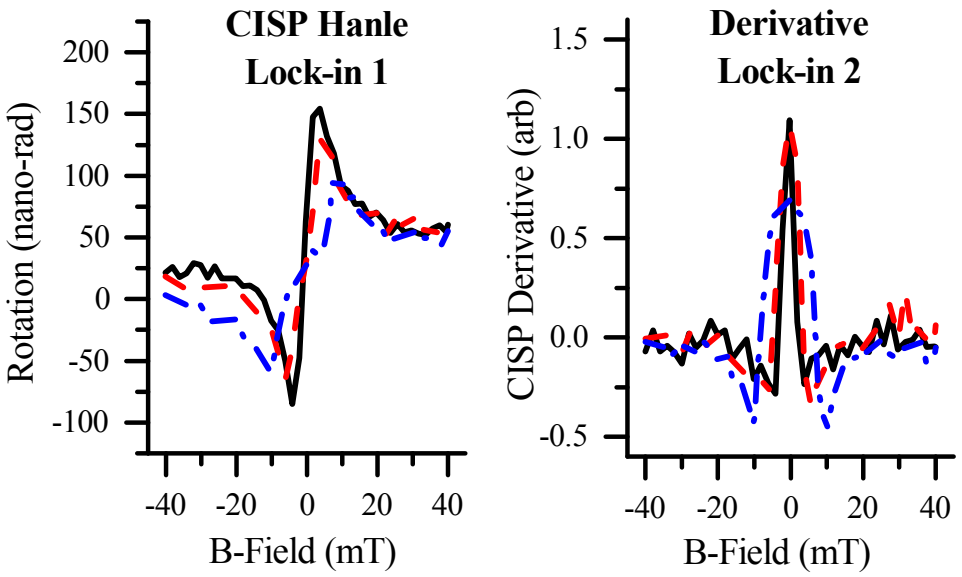

Figure 3.7: Cascaded lock-in measurement of Current Induced Spin Polarization Hanle and its derivative with respect to magnetic field in an InGaAs sample at 30 K. The amplitude of an oscillating voltage controlling the magnetic field modulation was varied: (blue dash-dot) 0.250 V_{rms}, (red dash) 0.125 V_{rms}, (black solid) 0.060 V_{rms}.

3.4 Analog to Digital Conversion

The key component of any modern measurement device, prior to data storage, is the analog-to-digital converter (ADC). In this chapter, we will discuss the relatively simple implementation of a 2-bit unipolar flash ADC whose circuit diagram is shown in Fig. 3.8. The interested reader should consult Ref. [52] for a more thorough discussion.

An ADC encodes a continuous variable's value as a discrete binary number. For our case, the continuous variable is a voltage in a circuit. The resolution of our measurement system is determined by the allowed voltage range and how many bits we use to record a value. In this example, we will use two bits, allowing us to record four different binary states: 00, 01, 10, and 11. We will also limit ourselves to a unipolar measurement where we can only measure positive values. Assuming ground

is 0 and the highest possible voltage is V_{max}, our resolution is

$$\text{resolution} = \frac{V_{max} - V_{min}}{2^{N_{bits}} - 1} \tag{3.17}$$

$$= \frac{V_{max}}{3} \tag{3.18}$$

Therefore we can label our four states as: 0 Volts (00), $V_{max}/3$ (01), $2V_{max}/3$ (10), and V_{max} (11).

We now need to define how we will *apply* the labels to a voltage between 0 and V_{max} when it enters our circuit. We will use the common scheme of taking the halfway point between our label values as a threshold. If we measure $V \leq V_{max}/6$, then we apply the label "0 Volts" or 00. If $V > V_{max}/6$, then we apply the label "$V_{max}/3$" or 01, and so on. We can implement this labeling scheme by using what is called an "R-2R" resistor ladder (shown in Fig. 3.8). By placing one terminal of a resistor R at ground, one terminal of another resistor R at $V_{ref} = V_{max}$, and then connecting them in series with $2^{N_{bits}} - 2$ resistors of value 2R, the junctions between the resistors will be at the voltages $V_{max}/6 + (x-1)\,(V_{max}/3)$, where x is the number of junctions up the ladder, starting from $x = 0$.

We have just created a voltage labeling scheme with a ladder of threshold voltages that we can use for comparison with our input voltage. Now, we use what are called comparators and *compare* our input voltage to all of the threshold voltages *simultaneously*. This simultaneous comparison is where the term "flash" comes from in the ADC name, since all possible digitization states are evaluated in parallel. The comparators can be implemented with a simple operational amplifier (Op-amp), where one terminal is held at the threshold voltage, while the other terminal is at the measured voltage. If the measured voltage is above a given threshold, the comparator output is 0, otherwise it is 1. The comparator output is then sent to an "exclusive or" gate, where the output is 0 unless one, *and only one*, input of the gate is 1. The

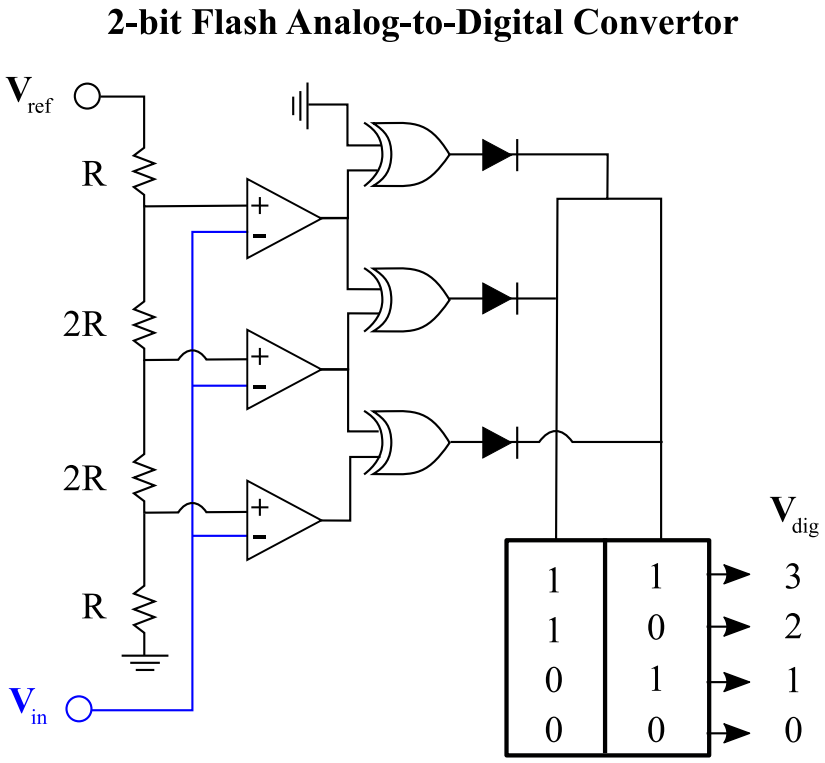

Figure 3.8: 2-bit unipolar flash analog-to-digital converter circuit with a truth table output. The input wire (blue) is held at V_{in}, the voltage to be measured. V_{ref} is held at V_{max} for the example in the text. R and 2R label the resistance values of an "R-2R" ladder. The triangle symbols with + and - are comparators implemented using a standard Op-amp. The stretched triangles with curved lines are "exclusive or" gates. The small filled black triangles with lines at the point are diodes. Ground is the standard three-line symbol with decreasing line length at the termination.

resulting logic allows for the proper encoding, left to the reader as an exercise.

To finalize the encoding, we must remember that there are only N_{bits} number of bits, but that we are working with $2^{N_{bits}} - 1$ junctions for our "R-2R" ladder labeling system. By placing diodes after the "exclusive or" gates, we can prevent any undesirable currents and strictly record a binary value. The result of the processing is shown as a truth table connected to the output wires for each bit.

Standard ADCs are more complex with protection circuitry, bipolar functionality, and other features. It is rare for an individual to build a custom ADC, but it remains useful for the average scientist to understand the key workings of nearly every measurement device. One important result of our discussion is that, at least for "flash" ADC design, halving the resolution means doubling the number of necessary components. Since it takes a finite amount of time for any information to travel, the length of the wiring in the circuit, along with the individual components' response, sets an upper bound for bandwidth. A common feature of commercially available ADCs is the reduction in the number of bits in order to achieve faster sampling rates. This tradeoff plays a limiting role in conventional spin noise measurements (see Sec. 4.4), spurring our development of Resonant and Time Resolved Spin Noise (see Ch. VII).

CHAPTER IV

Modern Optical Spin Sensitive Measurements

There are many ways of measuring spin dynamics, with and without physically contacting a sample. We will restrict our discussion to optical techniques, their implementation, and subsequent analysis. A primary benefit of optical techniques is that they do not require altering the sample in any appreciable fashion. This is in stark contrast to electrical measurements which can require extensive processing in highly specialized facilities before experimentation. We note that optical techniques have their own unique complications and discuss them for each measurement system.

The sections are organized as follows: The Hanle effect (Sec. 4.1), Time Resolved Photoluminescence (TRPL) (Sec. 4.2), Time Resolved Faraday and Kerr Rotation (TRFR/KR) (Sec. 4.3), and conventional spin noise techniques (Sec. 4.4).

4.1 The Hanle Effect

The Hanle Effect is the depolarization of a steady-state spin ensemble by an applied magnetic field. It is named for Wilhelm Hanle who in 1924 published a paper postulating that a Zeeman "level crossing" explained the observed signal in his experiment and the 1923 work of Wood and Ellet.[53, 54, 55, 56] In the same year that Hanle published his work, John Eldridge published a theory paper postulating that Larmor precession of classical "electric vibrators" would lead to a Lorentzian

lineshape.[57] In the abstract, he points out his classical theory does not account for the Zeeman splitting of Sodium lines. Hanle's "level crossing" hypothesis, a distinctly quantum perspective in that discrete transition energies are thought to be tuned into, and out of, resonance with one another, is what bridges the gap. Moreover, it requires that there be coherence between these transitions when they are in resonance, or else a net polarization would not be observed. At the time, the best quantum theories assumed radiative transitions were random. It is worth noting that the Stern-Gerlach experiment was published only two years before, and quantum mechanics still had not reached a mature form.

Hanle's revelation has led to a wealth of experiments in systems ranging from atomic gasses to interstellar radiation. More recently, the Hanle effect has been used to characterize solid state spintronic material systems ranging from optical measurements of GaAsBi to highly contested "3-T" electrical measurements in Si.[58, 59, 60]

The optics path for two variations of Hanle effect experiments are shown in Fig. 4.1. For PL detection, we make use of the modulated incident polarization scheme discussed previously (see Eq. 3.2), where

$$P = \frac{I_{\sigma_+,\sigma_+} - I_{\sigma_-,\sigma_+}}{I_{\sigma_+,\sigma_+} + I_{\sigma_-,\sigma_+}}$$

For Faraday rotation detection, we will also modulate the incident polarization, but make use of a balanced photodiode bridge and Eq. 3.9 for detection where:

$$\theta \simeq \frac{1}{2}\left(\frac{I_Y - I_X}{I_Y + I_X}\right)$$

4.1.1 The Model

The conventional method for deriving the Hanle effect is to start from Eq. 2.28 and solve for the steady state condition. We will take a different route and begin with

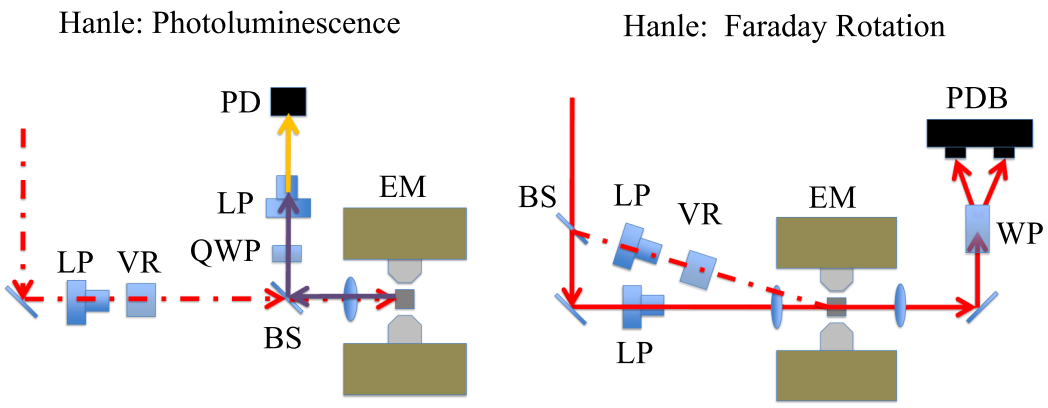

Figure 4.1: Optics paths for two different Hanle effect measurement schemes. (left) laser pumping with PL detection. (bottom) laser pumping with probe laser Faraday rotation detection. Dashed red lines are pump paths. Solid lines are for probes: laser (probe), PL (purple), and polarization filtered PL (yellow). `BS = beamsplitter, EM = electromagnet, LP = linear polarizer, PD = photodiode, PDB = photodiode bridge, QWP =` $\lambda/4$ `waveplate, VR = variable retarder, WP = Walloston prism.`

Eq. 2.31 and integrate assuming a constant polarization rate as our forcing function. The end result is the same, however we do need to let the spin lifetime $\tau_s \rightarrow T_s$ where T_s is an effective spin dephasing time that includes mechanisms beyond the spin dephasing we have already discussed. In this case, we assume that there will be some amount of PL generated from radiative recombination as we will be continuously pumping our sample and want to reach a steady state. At steady state, our pumping rate should be $\frac{S_0}{\tau_R}$ where τ_R is the radiative recombination time. We limit ourselves to τ_s and τ_R and can use Matthiessen's rule for summing rates to achieve

$$\frac{1}{T_s} = \frac{1}{\tau_s} + \frac{1}{\tau_R} \tag{4.1}$$

Putting everything together we get

$$S_X(\Omega) = \int_{-\infty}^{\infty} dt\, \frac{S_0}{\tau_R} G_X(t) \tag{4.2}$$

$$= \frac{S_0}{\tau_R} \sin\phi_0 \int_{-\infty}^{\infty} dt\, \mathbb{H}(t)\, e^{-t/T_s} \cos(\Omega t + \beta_0) \tag{4.3}$$

$$= \frac{S_0}{\tau_R} \sin\phi_0 \int_{0}^{\infty} dt\, e^{-t/T_s} \cos(\Omega t + \beta_0) \tag{4.4}$$

$$= \frac{S_X(0, \Omega, \beta_0, \phi_0)}{1 + \Omega^2 T_s^2} \tag{4.5}$$

where

$$S_X(0, \Omega, \beta_0, \phi_0) = \frac{S_0}{1 + \frac{\tau_R}{\tau_s}} \sin\phi_0 (\cos\beta_0 + \Omega T_s \sin\beta_0) \tag{4.6}$$

If we were to use a probe laser and perform Faraday rotation measurements, then we can combine Eqs. 4.5 and 4.6 with 2.50 and our derivation is complete. If instead, we plan to use PL for the measurement, as was originally done, we need to connect the injected spin polarization to the detected percent PL polarization. Assuming that the excitation and recombination pathways are identical—not generally true as non radiative pathways may exist—then we can make the substitution $S_0 \rightarrow S_0^2 \sim P_0$ where P_0 is the maximum possible percent polarization. Equations 4.5 and 4.6 become

$$P(\Omega) = \frac{P(0, \Omega, \beta_0, \phi_0)}{1 + \Omega^2 T_s^2} \tag{4.7}$$

$$P(0, \Omega, \beta_0, \phi_0) = \frac{P_0}{1 + \frac{\tau_R}{\tau_s}} \sin\phi_0 (\cos\beta_0 + \Omega T_s \sin\beta_0) \tag{4.8}$$

Figure 4.2 shows the expected signal for two cases of ϕ and β values. We can see that the factor gT_s determines the width of the Hanle curves while the ratio τ_R/τ_s determines the maximum measured polarization. This shows that an appreciable amount of information for a given material's spin dynamics can be inferred from

Hanle measurements. However, exact value extraction of any of the parameters is problematic.

4.1.2 Pros and Cons

The Hanle effect is one of the simplest ways to show that a sample exhibits spin dependent behavior, but a main drawback is the inability to deconvolute g and T_s. In essence, Hanle data *must* be supplemented by another type of measurement to completely determine the spin dependent parameters. One remedy is to perform time resolved PL (TRPL) with a pulsed laser system and extract τ_R. We will discuss TRPL in the next section.

Another complication is the convolution of τ_R and τ_s. The spin evolution continues up until carrier recombination occurs. We can see from Fig. 4.2 that if $\tau_R \ll \tau_s$, then the polarization signal will be strong at 0-field but the ensemble will not have had sufficient time to evolve, broadening the Hanle curve. If the opposite is true, then the polarization signal will be negligible due to the spins appreciably dephasing long before radiative recombination, on top of broadening the Hanle curve.

Samples must be chosen carefully when attempting Hanle measurements. Increasing the dopant level will typically decrease τ_R, but it also places more unpolarized carriers in the bands. If pumping is not sufficient to overwhelm the doped carrier density of the sample with polarized spins, then the magnitude of the PL polarization signal will suffer. If pumping is too high, sample heating could occur, complicating data analysis. On the positive side, Hanle PL measurements can be performed on samples that have broad emission spectra. Such samples are problematic for Faraday and Kerr rotation as, by symmetry arguments, they likely have broad absorption spectra which can diminish the differential index of refraction—the key physical parameter in those measurements.

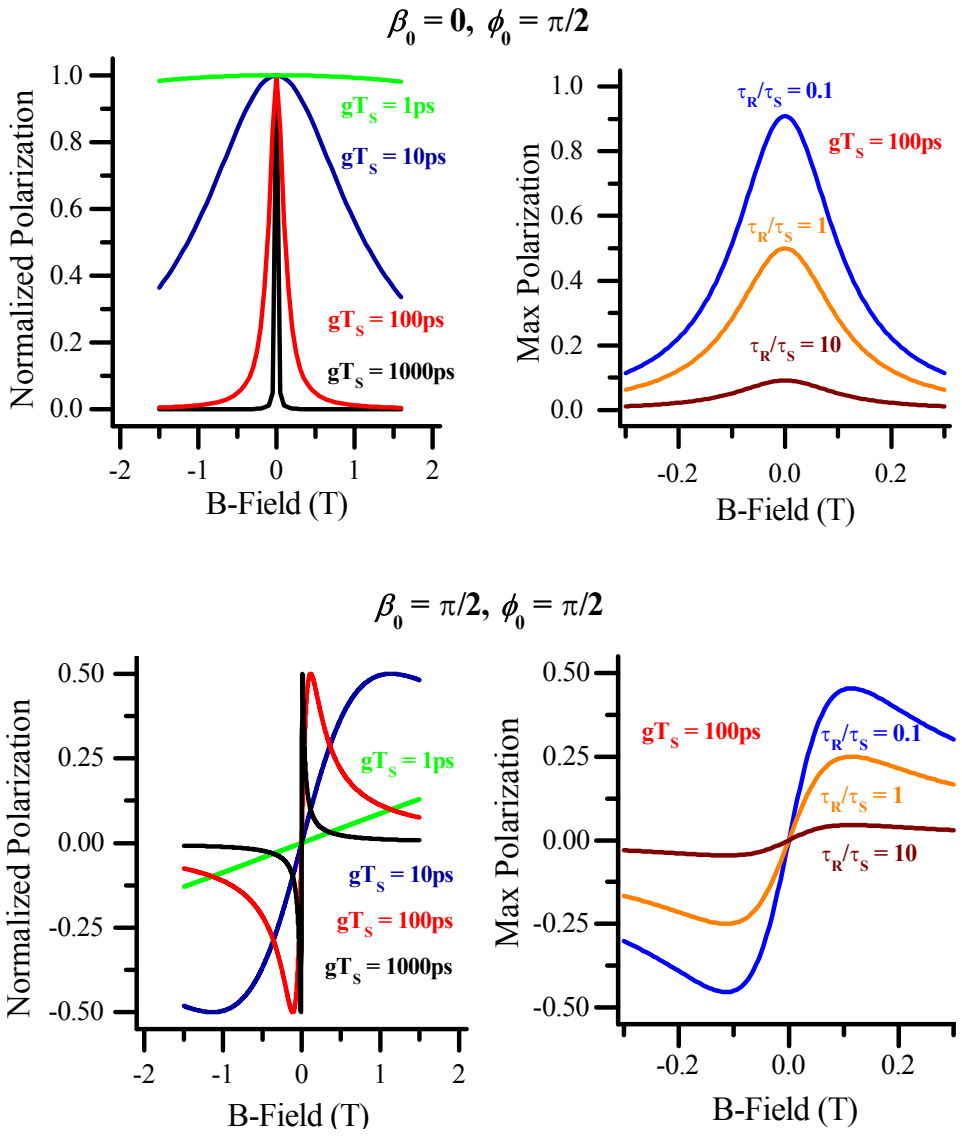

Figure 4.2: Expected Hanle curves plotted for two different initial polarization directions with various values for the product gT_s and the ratio τ_R/τ_s. (top) initial polarization is orthogonal to the sample surface and parallel to the optical path. (bottom) initial polarization is parallel to the plane of the sample surface and orthogonal to the optical path.

4.2 Polarization Dependent Time Resolved Photoluminescence

In order to perform TRPL measurements, we must have a way of pumping, and then probing, a sample on time scales much shorter than the time scale of the studied dynamics. To do this, we will assume we have access to a pulsed laser system with appropriately small pulse widths. We will modulate the circular polarization of the laser and use it as a pump. A streak camera with polarization filtering will be used to time resolve the emitted photoluminescence. We further assume that the pulse repetition time is much longer than all relevant dynamics, including τ_R. We will address the opposite case, specifically for Faraday and Kerr rotation, in Sec. 4.12. The optics path of polarization dependent TRPL is identical to a Hanle PL experiment, with the exceptions of a pulsed excitation laser and a streak camera detector (see Fig. 4.1).

4.2.1 The Model

Our pump pulse is modeled well by the Dirac-delta function used to acquire Eq. 2.31. We directly relate the spin polarization to the detected PL circular polarization, the same as we did in our discussion of the Hanle effect. We arrive at

$$P\left(\Delta t, \Omega, \phi_0, \beta_0\right) = P_0 \mathbb{H}\left(\Delta t\right) e^{-t/\tau_s} \sin\phi_0 \cos\left(\Omega \Delta t + \beta_0\right) \tag{4.9}$$

Expected signal is plotted in Fig. 4.3 where the spin dependent behavior rides on top of a radiative decay signal that can be much larger. Taking the difference of the signals generated by opposite pump conditions isolates the spin dependent behavior, modeled by Eq. 4.9.

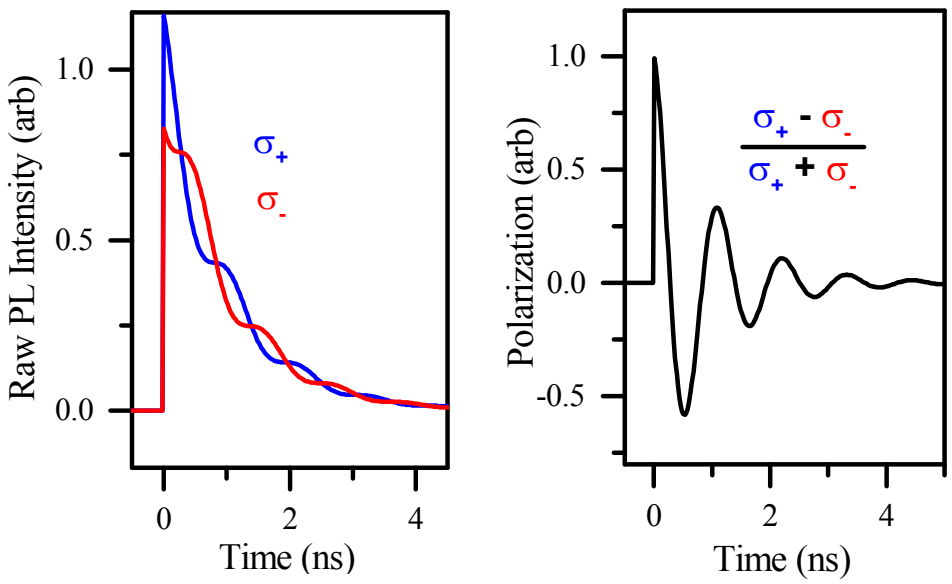

Figure 4.3: Expected polarization dependent TRPL signal curves plotted for $\beta_0 = 0$, $\phi_0 = \pi/2$, $\tau_s = \tau_R$ =1ns, $g = 0.4$, and $B = 160$ mT. (left) TRPL simulated for two different incident polarizations. (right) The differential signal is obtained from the raw signals using Eq. 3.2 and modeled by Eq. 4.9

4.2.2 Streak Cameras

PL has an associated recombination rate which can be calculated with the help of Fermi's Golden Rule (see Sec. 2.2.4.2). If we assume that we briefly excite a population of N number of electrons to the conduction band and that their recombination rate $1/\tau_R$ remains constant, we can write the following differential equation:

$$\frac{\partial N}{\partial t} = \frac{-1}{\tau_R} N \tag{4.10}$$

In other words, the excited population exponentially decays as $N(t) = N_0 \exp(-t/\tau_R)$ where N_0 is the initial number of excited carriers. If we could count all the carriers that arrive at a detector during a given window of time δt *and* vary the position of that window, then we could map out the approximate form of Eq. 4.10

$$\frac{N(t_i + \delta t) - N(t_i)}{\delta t} \simeq \frac{-N(t_i)}{\tau_R} \tag{4.11}$$

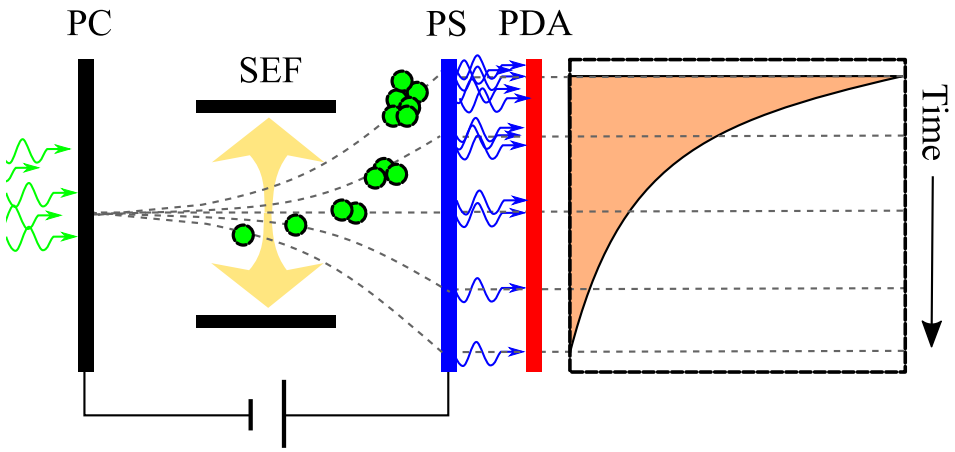

Figure 4.4: A schematic of a streak camera generating time dependent data. A constant bias is applied between the photocathode and the phosphor screen. A field is swept orthogonal to the direction of travel for the free electrons. `PC = photocathode, PDA = photodetector array, PS = phosphor screen, SEF = swept electric field`

A streak camera is a specialized piece of equipment that attempts to map out the function $N(t)$ that could be modeled by Eq. 4.10 or more complex rate equations. The camera must be used in tandem with a pulsed laser system so that a population of carriers can be excited quickly and then decay freely.

Streak cameras work by first exploiting the photoelectric effect, where light quanta of high enough energy emitted as PL from a sample can help free an electron from its Coulombic attraction to a given material. We call the material that emits the electrons a photocathode. The free electrons are accelerated towards, and collide into, a phosphor plate with an applied voltage between the photocathode and the phosphor plate. While accelerating toward the plate, an electric field is rapidly swept in magnitude *orthogonal* to the electron's direction of travel, causing a *streak* in the free electron distribution, dependent upon *when* each electron was released from the photocathode. Upon hitting the phosphor screen, each electron's energy is converted into photons that are released by the phosphor. Those photons hit a photodetector array and are counted. The arrival time distribution of the photons is thereby converted

into a spatial distribution at a photodetector array. The size of the photodetectors, rate of the electric field sweep, and a number of other factors determine the sensitivity and applicability of the streak camera. A diagram of a typical streak camera system is shown in Fig. 4.4.

4.2.3 Pros and Cons

Polarization dependent TRPL measurements do not have to contend with the convolution of gT_s during fitting, a major improvement over Hanle. This is because we can also map out the time evolution directly rather than infer its existence from a field scan. We can also isolate the spin dependence from a simple subtraction of two opposite excitation state measurements, while extracting τ_R from an average of the same signals.

On the downside, the signal to noise decays as τ_R as opposed to τ_s due to the time dependent behavior of radiative recombination. As time evolves, there are fewer and fewer carriers available in the conduction band leading to a smaller and smaller overall signal. Hanle measurements do not have this issue as they are performed under steady state conditions. Compounding the problem is that if $\tau_R \ll \tau_s$, the spins will not have enough time to evolve and we will not extract any appreciable time dependent spin signal. If $\tau_R \gg \tau_s$, then like Hanle, we will not see any spin dependent signal at all. The same care with sample selection for Hanle applies to TRPL.

4.3 Time Resolved Faraday and Kerr Rotation

TRFR/KR are the time resolved measurements of induced circular birefringence of a sample. The technique was developed circa 1994 by David Awschalom's research group at the University of California, Santa Barbara.[61] Like polarization dependent TRPL, these techniques require a pulsed laser system, but rather than just use pulses

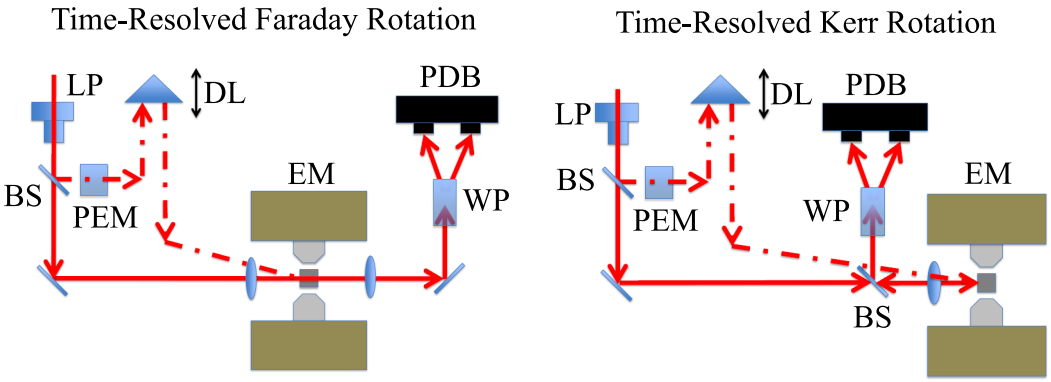

Figure 4.5: Time resolved Faraday (left) and Kerr (right) rotation optics paths. Red lines are pump (dash-dot) and probe (solid) lasers. `BS = beamsplitter, DL = delay line, EM = electromagnet, LP = linear polarizer, PEM = photo-elastic modulator, PDB = photodiode bridge, WP = Walloston prism.`

for excitation, we must also use them for detection.

In order to achieve accurate time resolution, we make use of the fact that the speed of light is constant. By splitting a single pulse along two paths, and then varying one path length relative to the other using a mirror on a delay stage (see Fig. 4.5) we can control the relative pump and probe arrival times. It is possible to purchase commercial piezos that allow sub-nm positioning but for practical purposes such accuracy is not needed. To the best of the author's knowledge, the shortest obtained pulsewidth in time is 67 attoseconds.[62] This corresponds to the spatial halfwidth of the pulse intensity being ~20 nm. For the experiments discussed in this dissertation, the pulsewidths were ~3 picoseconds corresponding to a need for ~1 mm resolution in pathlength accuracy.

4.3.1 The Model

Like TRPL, we do not need to make any appreciable modifications to Eq. 2.31 to model TRFR/KR. Moreover, we assume we can reach a minimally perturbative condition where we can ignore radiative recombination. We are not attempting to

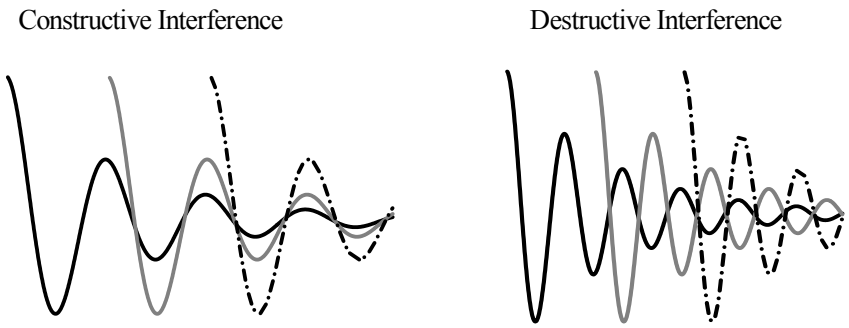

Figure 4.6: Interference of Time Resolved Faraday/Kerr Signals.

reach a steady state as in the Hanle effect, so minimizing perturbation is possible. We rewrite Eq. 2.31 explicitly as a rotation angle by using Eq. 2.50 and let $t \to \Delta t$ to represent the relative pulse delay time.

$$\theta\left(\Delta t, \Omega, \phi_0, \beta_0\right) = \theta_0 \mathbb{H}\left(\Delta t\right) e^{-\Delta t/\tau_s} \sin\phi_0 \cos\left(\Omega \Delta t + \beta_0\right) \tag{4.12}$$

where

$$\theta_0 = S_0 \sigma_F d \tag{4.13}$$

with S_0 the maximum spin density amplitude, σ_F the Faraday cross-section, and d the physical path length of the probe light through the sample.

4.3.2 Resonant Spin Amplification

Pulsed laser systems have pulse repetition periods t_{rep} of varying length based on design. If $\tau_s \gtrsim t_{rep}$, then we must account for contributions from subsequent pulses (shown schematically in Fig. 4.7). We do this by assuming each pump pulse excites its own isolated spin population and sum over many pump pulses delayed by t_{rep}. We give a simplified expression with $\beta_0 = 0$ and $\phi_0 = \pi/2$, useful for most experiments.

$$\theta\left(\Delta t, \Omega\right) = \theta_0 \sum_{n=0}^{\infty} \mathbb{H}\left(\Delta t + n t_{rep}\right) e^{-\left(\Delta t + n t_{rep}\right)/\tau_s} \cos\left[\Omega\left(\Delta t + n t_{rep}\right)\right] \tag{4.14}$$

If we assume that $\Delta t \geq 0$, we can derive a closed form solution.

$$\theta\left(\Delta t, \Omega\right) = \theta_0 e^{-\Delta t/\tau_s} \frac{\cos\left[\Omega \Delta t\right] - e^{-\Delta t/\tau_s} \cos\left[\Omega\left(\Delta t - t_{rep}\right)\right]}{\sin^2\left[\Omega t_{rep}\right] + \left(\cos\left[\Omega t_{rep}\right] - e^{t_{rep}/\tau_s}\right)^2} \tag{4.15}$$

When $\tau_s \gtrsim t_{rep}$, it is typically very difficult to fit *time* dependent experimental data for the parameter τ_s. The feasible range for a time delay scan is fixed by t_{rep} while the ideal delay window would be $> \tau_s$. Therefore, we must use another tunable parameter to extract functional behavior. In this case, we can tune an external magnetic field to change the Larmor precession frequency and directly observe interference. The resultant signal is referred to as Resonant Spin Amplification, also developed by the Awschalom group, with the first publication in 1998.[63] Plots of Eq. 4.15's dependence upon Δt and Ω are shown in Fig. 4.7. In the limit that $t_{rep} \gg \tau_s$, Eq. 4.15 reduces to Eq. 4.12.

4.3.3 Pros and Cons

TRFR/KR have the distinct advantage over Hanle measurements of having g and τ_s as independent model parameters. Moreover, if we choose appropriately small laser powers for the pump and probe, we can avoid significant perturbations and neglect radiative recombination effects in our signal. We also have direct access to the short *and* long timescale evolution of our samples through resonant spin amplification.

However, there are some drawbacks. One important issue is the need for steep absorption curves at the bandedge of a given sample. Steep slopes will lead to steep changes in the index of refraction, thereby amplifying any differential index measurement. If a sample is a high quality bulk crystal, or has reduced carrier dimensionality (e.g. a quantum well, wire or dot), then absorption curves are quite steep by design. The issues typically arise with novel materials in the early stages of growth characterization which can correlate with defects and inhomogeneity. Of course, these are the

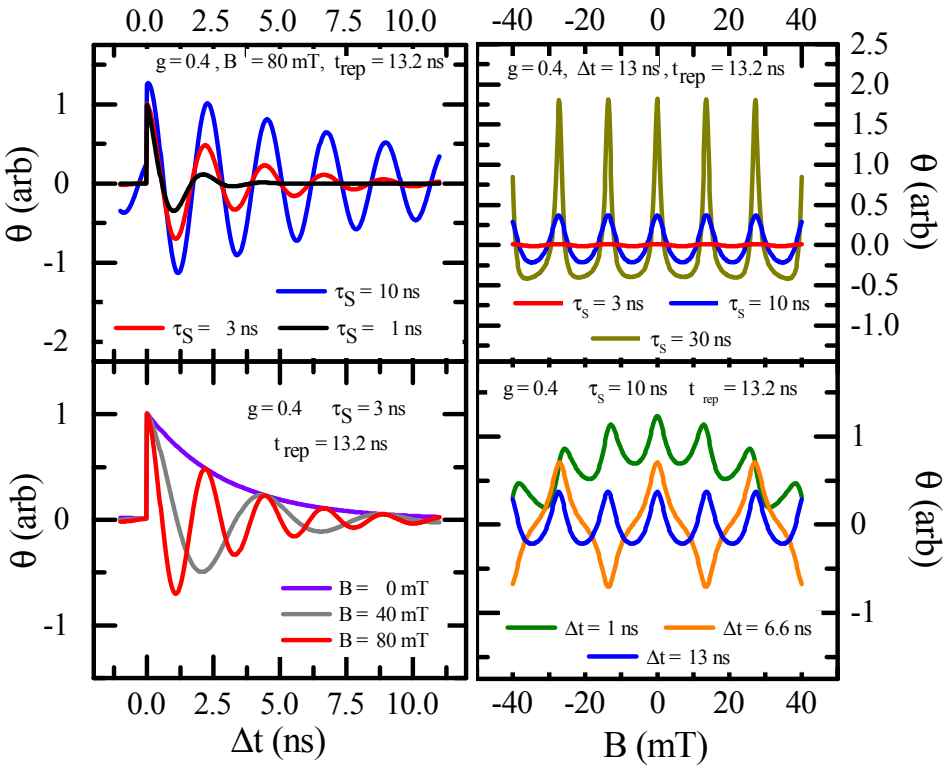

Figure 4.7: (left) Expected Time Resolved Faraday/Kerr Rotation and (right) Resonant Spin Amplification Curves for various parameter values. All plots use Eq. 4.15. The color coding is the same for both plots, allowing for direct comparison of time delay scans at fixed field and field scans at fixed time delay.

types of materials that can be most promising to study. Indirect bandgaps are also problematic, with Ge being one of the few indirect gap materials successfully probed by TRFR/KR.[64, 65] This is, at least in part, due to the close proximity of a direct gap allowing for more efficient pumping.

Another problem arises when the carrier density is low, as there are few carriers with which to interact, leading to a proportional decrease in signal. If a sample is doped with $\sim 10^{16}$ carriers/cm^2, then we could excite $\sim 10^{15}$ carriers/cm^2 without significant perturbation. In an undoped sample of GaAs, the intrinsic carrier density is $\sim 10^{13}$ carriers/cm^2 implying we would have to decrease our pump intensity by $\sim$3 orders of magnitude to avoid significant perturbation. PL measurements such as Hanle or polarization dependent TRPL complement TRFR/KR with their opposite strengths and weaknesses.

4.4 Conventional Spin Noise

Conventional spin noise spectroscopy is the detection of spin fluctuations and analysis of their Fourier spectra. Experiments attempt to extract information from the covariance of subsequent spin polarization measurements of a sample at thermal equilibrium. The fluctuation dissipation theorem implies that a randomly oriented spin ensemble should decay to equilibrium in the same fashion as a purposefully oriented ensemble.[66] Therefore, if we apply a magnetic field to a sample containing an ensemble of spins, the normal dynamics apply. For typical measurements, a signal proportional to the spin polarization is rapidly digitized in the time domain and then processed with a Fast Fourier Transform.

Spin noise can trace its roots to Felix Bloch's 1946 paper titled "Nuclear Induction." [33] In that paper, he mentions that for N nuclei of magnetic moment μ, there should be a "resultant moment of the order $(N)^{1/2}\,\mu$" due to "statistically incomplete cancellation." The first published measurement of nuclear spin noise did not occur

until 1985.[67] The earliest published Faraday rotation measurement of spin noise was slightly earlier in 1981.[68] Neither paper seemed to spark much interest in spin noise for analysis, possibly due to the difficulty in achieving appreciable signal.

In 2004, Scott Crooker et al. published a paper using what is arguably the current standard design for optical spin noise measurements.[69] They measured fluctuations in spin polarization for two isotopes of rubidium using the simple optics path shown in Fig. 4.8. Extraction of the noise spectra was performed by a spectrum analyzer connected to a balanced photodiode bridge. The very next year, Michael Oestreich and collaborators published their measurements of the spin noise of electrons in GaAs using a similar setup.[70] The research groups led by Crooker in the United States and Oestreich in Germany have continued to develop innovative capabilities for spin noise measurements. The interested reader should consult the following review papers for a bit more of the history and discussion of available methods: Refs. [71, 72].

The literature is somewhat unclear on the accepted derivation of spin noise. It is near universally accepted that the Fourier transform of the spin noise spectrum should be a Lorentzian, stemming from the decaying sinusoidal behavior of spin dynamics. Numerous measurements support this analysis, but to date, there has not been any publication directly mapping the correlation function. There is one measurement that reports the derivative of a time resolved signal, but the analysis is atypical and our modeling runs counter to some of their claims.[15]

For the time being, we will only address spectrally resolved spin noise measurements and leave the time resolved discussion for Ch. VII. Spectrally resolved experiments typically use linearly polarized continuous wave (CW) lasers as Faraday rotation probes with an optical path comparable to Fig. 4.8. The electronics used must be fast enough to record signal peaks at tuned Larmor precession frequencies, so $\sim$MHz to $\sim$GHz photodiode bridges followed by comparably fast spectral analysis systems are required. Since the electronic sampling is rapid, the system performs time

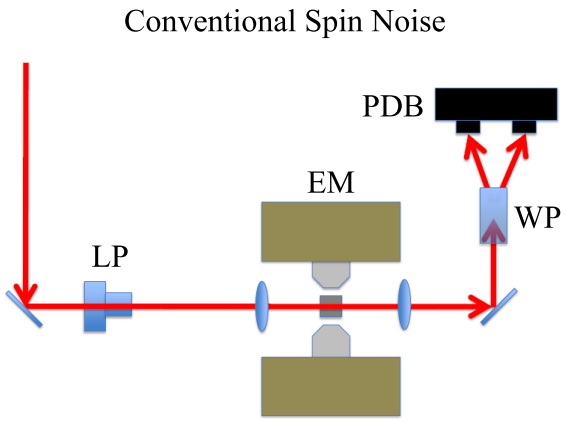

Figure 4.8: Conventional Spin Noise optics path. The laser (solid red line) can be continuous wave or pulsed. `EM = electromagnet, LP = linear polarizer, PDB = photodiode bridge, WP = Walloston prism.`

resolved Faraday rotation but the signal only becomes useful after a Fourier transform. We will derive the covariance function and expected Fourier spectra below. The covariance function is a key result that we will need again in Ch. VII.

4.4.1 The Model

We begin, much as we have in previous sections, with Eq. 2.31. We will also make use of the relation $\theta_0 = S_0 \sigma_F d$ to put our result in terms of the covariance of our rotation measurement. The covariance of a random variable X can be written as

$$Cov\left(X_i, X_j\right) = \langle X_i X_j \rangle - \langle X \rangle^2 \tag{4.16}$$

where $\langle X \rangle$ is the expectation value for X and the X_i are independent measurements. If we take $\langle \theta \rangle = 0$, an acceptable approximation for GaAs and many non-magnetic materials, then we have reduced our work to finding

$$Cov\left(\theta_i, \theta_j\right) = \langle \theta_i \theta_j \rangle \tag{4.17}$$

Invoking the fluctuation dissipation theorem, we say

$$\theta_i = \theta_0 \mathbb{H}(t_i)\, e^{-t_i/\tau_s} \sin\phi_0 \cos(\Omega t_i + \beta_0) \tag{4.18}$$

Substituting Eq. 4.18 into Eq. 4.17, we get

$$Cov(\theta_i, \theta_j) = \left\langle \theta_0^2 e^{-(2t_i+\Delta t)/\tau_s} \sin^2\phi_0 \cos(\Omega t_i + \beta_0) \cos[\Omega(t_i + \Delta t) + \beta_0] \right\rangle \tag{4.19}$$

where we have assumed both values of θ are from the same evolving spin ensemble. This assumption allows the substitution of $t_j = t_i + \Delta t$ and the subsequent dropping of the Heaviside function. We are allowed to make this assumption because the value of $Cov(\theta_i, \theta_j)$ is 0 otherwise. This can be confirmed by the equality $\langle\theta_i\theta_j\rangle = \langle\theta_i\rangle\langle\theta_j\rangle$ for *uncorrelated* measurements and our assumption that $\langle\theta\rangle = 0$.

We must now average over all possible orientations and amplitudes of our spin polarization. This appears somewhat complicated by the time variable t_i, but is straightforward to address. We set $t_i = 0$ and let $\Delta t \to |\Delta t|$ as our spin noise experiments should not depend upon the *absolute* time they were conducted, only the *relative* time between measurements Δt. If averaging over t_i were necessary, it could not be taken over all time as the value of the covariance becomes 0. It is difficult to justify a truncated time average as all Δt values should be allowed in our covariance function. To truncate the time average is to truncate the allowed Δt values.

From here, our covariance becomes

$$Cov(\theta_i, \theta_j) = \left\langle \theta_0^2 e^{-|\Delta t|/\tau_s} \sin^2\phi_0 \cos(\beta_0) \cos[\Omega|\Delta t| + \beta_0] \right\rangle \tag{4.20}$$

$$= \left\langle\theta_0^2\right\rangle \left\langle\sin^2\phi_0\right\rangle e^{-|\Delta t|/\tau_s} \times \left[\cos\Omega|\Delta t| \left\langle\cos^2\beta_0\right\rangle - \frac{1}{2}\sin\Omega|\Delta t| \left\langle\sin 2\beta_0\right\rangle\right] \tag{4.21}$$

where we have broken up the averaging over the respective variables θ_0, β_0, and ϕ_0.

Letting $0 \leq \phi_0 < \pi$ and $0 \leq \beta_0 < 2\pi$, we average over the angles and reduce Eq. 4.21 to

$$Cov\left(\theta_i, \theta_j\right) = \frac{1}{4}\left\langle \theta_0^2 \right\rangle e^{-|\Delta t|/\tau_s} \cos\Omega|\Delta t| \tag{4.22}$$

We can separate the covariance into the variance of single measurement values and the unit magnitude correlation function as

$$Var\left(\theta_i\right) = \frac{1}{4}\left\langle \theta_0^2 \right\rangle \tag{4.23}$$

$$Corr\left(\theta_i, \theta_j\right) = e^{-|\Delta t|/\tau_s} \cos\Omega|\Delta t| \tag{4.24}$$

Equation 4.24 is sufficient for application of a Fourier transform which will yield the expected Lorentzian spectral shape. If we are interested in the *amplitude* of the signal, we will have to do a bit more work.

4.4.2 Fourier Spectra

We briefly postpone discussion of the amplitude and define a Fourier transform and its inverse as

$$F\left(\omega\right) = \int_{-\infty}^{\infty} d\Delta t f\left(\Delta t\right) e^{-i\omega\Delta t} \tag{4.25}$$

$$f\left(\Delta t\right) = \frac{1}{2\pi}\int_{-\infty}^{\infty} dw F\left(\omega\right) e^{i\omega\Delta t} \tag{4.26}$$

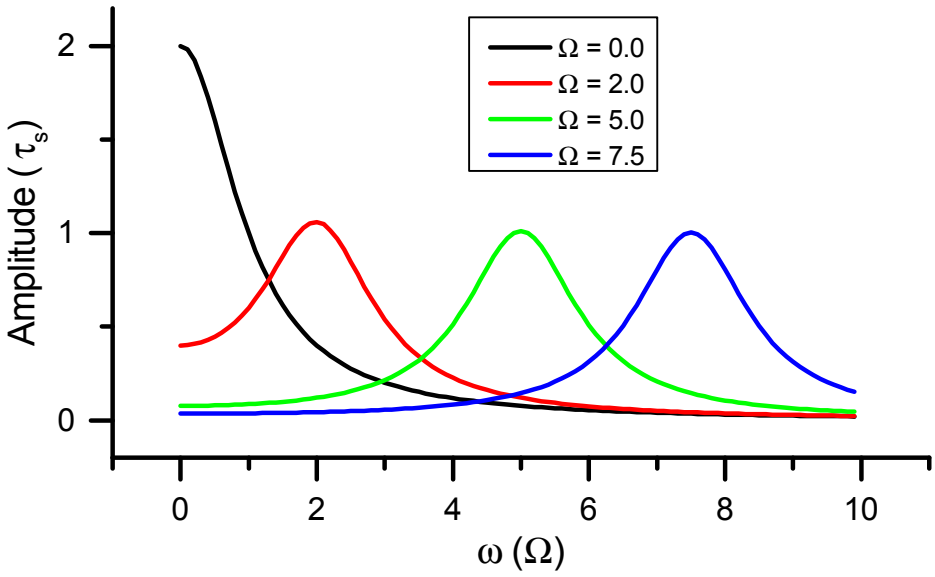

Figure 4.9: Fourier spectra of conventional spin noise spectroscopy. Vertical axis is in units of $\tau_s = 1$. Horizontal axis is in units of Ω. Various values for Ω are plot using Eq. 4.29. A similar figure, but of data collected by Scott Crooker et al., can be found in Ref. [73]

Operating on Eq. 4.24 and taking the real part yields

$$Re\left\{F\left[Corr\left(\theta_i,\theta_j\right)\right]\right\} = Re\left\{\int_{-\infty}^{\infty} d\Delta t\, e^{-|\Delta t|/\tau_s}\cos\Omega|\Delta t|\right\} \tag{4.27}$$

$$= 2\int_{0}^{\infty} d\Delta t\, e^{-\Delta t/\tau_s}\cos\Omega\Delta t\cos\omega\Delta t \tag{4.28}$$

$$= \tau_s\left[\frac{1}{1+\tau_s^2\left(\omega-\Omega\right)^2}+\frac{1}{1+\tau_s^2\left(\omega+\Omega\right)^2}\right] \tag{4.29}$$

We plot the behavior in Fig. 4.9. Since the lineshapes are Lorentzian, the width dependence upon τ_s is equivalent to the even-Lorentzian Hanle lineshape dependence on gT_s (see Fig. 4.2). However, with spin noise, we are able to shift the peak away from 0 and extract g from the linear relationship between field strength and peak location.

4.4.3 Amplitude Behavior

We will now derive the value of $\langle\theta_0^2\rangle$ found in Eq. 4.23. We start, by using Eq. 2.50, yielding

$$\langle\theta_0^2\rangle = \sigma_F^2 d^2 \langle S_0^2\rangle \tag{4.30}$$

Since S_0 is a spin polarization density, we can rewrite it as

$$S_0 = \frac{N_+ - N_-}{V} \tag{4.31}$$

where $N_\pm$ are the total number of *probed* carriers for a given spin. $V = Ad$ is the volume probed by the laser, assumed to be cylindrical, and defined by the cross-section A and sample thickness d. We substitute these values back into Eq. 4.30, arriving at

$$\langle\theta_0^2\rangle = \frac{\sigma_F^2}{A^2} \langle(N_+ - N_-)^2\rangle \tag{4.32}$$

Using the fact that the spins we are discussing are a two state system, the distribution for the polarization along the radius of our spherical geometry should be binomial. In that case, we can interpret $\langle(N_+ - N_-)^2\rangle$ as the variance of a binomial distribution of $N = N_+ + N_-$ total spins. Therefore $\langle(N_+ - N_-)^2\rangle = (1/4)\,N$. For those concerned about having negative radial values, the variance calculation yields the same magnitude, whether we integrate over the entire number line, or just restrict ourselves to positive values.

Equation 4.32 is now

$$\langle\theta_0^2\rangle = \frac{\sigma_F^2}{4}\frac{N}{A^2} \tag{4.33}$$

If we multiply top and bottom by d, we can write our result in terms of the more useful value of carrier density n, yielding

$$\langle\theta_0^2\rangle = \frac{\sigma_F^2}{4}\frac{nd}{A} \tag{4.34}$$

We can now see that the variance of our measurements θ_i goes as

$$Var\left(\theta_i\right) = \frac{\sigma_F^2}{16}\frac{nd}{A} \tag{4.35}$$

with an inverse dependence upon probe beam cross-section, and linear dependence upon carrier density and sample thickness. The carrier density and cross-section dependence have already been experimentally demonstrated.[73, 69]

We can also quantitatively compare the square root of Eq. 4.35 to published theory and measurements using Ref. [45]. They did not perform an average over the angles of the Bloch sphere and essentially use 4.34, leading to a factor of two difference compared to our final result. To highlight this difference, we explicitly use $\langle\theta_0^2\rangle$ in their calculation, instead of $Var\left(\theta_i\right)$. Solving for σ_F where $\sigma_F^{\phi_0,\beta_0}$ is our calculation and σ_F^{Giri} is from Ref. [45], we get

$$\sigma_F^{\phi_0,\beta_0} = 4\sqrt{\frac{Var\left(\theta_i\right)}{fn}\frac{A}{d}} \tag{4.36}$$

$$\sigma_F^{Giri} = 2\sqrt{\frac{\langle\theta_0^2\rangle}{fn}\frac{A}{d}} \tag{4.37}$$

where we have introduced the factor f from Ref. [45] to account for the Fermi distribution of carriers and the relative probe energy. Using values from Table I in Ref. [45] and defining $\sigma_F^{Giri:th}$ as the value calculated from first principles, we see that Eq. 4.36 has slightly worse agreement between experiment and theory compared to Eq. 4.37.

It is unclear if this is a sign of breakdown in the Bloch sphere utility or assumption errors in the relatively new calculation of Ref. [45]. We should note that there is no classical argument to avoid averaging over the angles ϕ_0 and β_0. All values are within an order of magnitude with the first principles calculation being consistently *lower* than those extracted from data. This includes the cases discussed in Ref. [45]

Spin Noise Data	Ref. [45]		This Work
	$\sigma_F^{Giri:th}$ rad×cm^2	$\sigma_F^{Giri:exp}$ rad×cm^2	$\boldsymbol{\sigma_F^{\phi_0,\beta_0:exp}}$ rad×cm^2
Ref. [74]	-1.2×10^{-15}	$\pm 3 \times 10^{-15}$	$\pm 6 \times 10^{-15}$
Ref. [73]	-0.85×10^{-15}	$\pm 2.9 \times 10^{-15}$	$\pm 5.8 \times 10^{-15}$

Table 4.1: Comparison of Faraday Coefficient Calculations using sample information and spin noise data from Refs. [74, 73]. $\sigma_F^{Giri:th}$ is a calculation of the Faraday cross-section from first principles made by Ref. [45]. $\sigma_F^{Giri:exp}$ is the extraction of the Faraday cross-section by Ref. [45] using Eq. 4.37 and the available data set. $\sigma_F^{\phi_0,\beta_0:exp}$ is our extraction of the Faraday cross-section using Eq. 4.36 which includes the factor of 2 relative to $\sigma_F^{Giri:exp}$ due to averaging over ϕ_0 and β_0.

involving TRFR/KR, an experiment that involves active spin pumping. One would expect some variation of the experimentally extracted magnitudes both above *and* below the theoretical predictions if all the relevant physics were included. However, the available calculation can aide in experiment planning as a lower bound is a useful predictor of feasibility.

4.4.4 Pros and Cons

Conventional spin noise is a simple and powerful tool. As it is strictly a probe rather than pump-probe, measurement, it has found applications as wide ranging as three-dimensional mapping of charge density, determination of the homogeneous linewidth of quantum dots, and observing the Zeeman splitting of an atomic gas.[69, 13, 14] Those measurements go well above and beyond the general utility of nearly non-perturbative spin dependent parameter extraction.

However, there are some key downsides to this method. Similar to the Hanle effect, if τ_s is very small, the signal is very broad with a low peak amplitude. For Hanle measurements, we could simply apply larger and larger magnetic fields in order to map out the spin behavior. For conventional spin noise, we would observe the broad

peak shift out of the bandwidth limited measurement window as we increased the magnetic field. This brings us to another point: the fastest observable precession frequency is fixed by the bandwidth of the detectors. For practical purposes, this restricts modern spin noise detection of Larmor precession frequencies to below $\sim$1 GHz.

Much of this has to do with the capabilities of the fastest digitizing boards and balanced diode bridge response. It is foreseeable that with improved technology, faster sampling rates will become available, and indeed, there exist digitizers that can operate up to $\sim$100 GHz, but they bring another issue: effective bit depth. Digitizing a voltage requires an ADC where an array of logic gates allow for discretized recording. The size and speed of those gates determines the rate at which information can be stored. If we desire slow sampling, we can have a large array of gates which will allow for many more discrete bins giving us high resolution. If instead, we want a very fast board, we need to remove gates, reducing the number of bins, or "bit depth." Modern $\sim$1 GHz oscilloscopes have an effective bit depth of $\sim$6 bits. This corresponds to about two digits of precision.

Two digits of precision should be plenty for large signal to noise ratios, but many reported measurements are in the single to tens of nanoradian/$\sqrt{\text{Hz}}$. Background voltage fluctuations from shot noise, thermal noise, and a host of other sources can become comparable or larger than the spin noise signal at this range. There has been some work on creating sampling schemes to push the envelope, but digitization remains a roadblock for the study of fast oscillations, rapid dephasing, and very small signals.[75] We discuss the complement to this technique that overcomes the above roadblocks, and is the key result of this disseration, in Ch. VII.

CHAPTER V

Spin Dynamics of GaAsBi

In this chapter, we discuss Hanle effect measurements of the novel alloy GaAsBi that were published in an original paper, listed as Ref. [58]. We begin with the motivation for the experiment (Sec. 5.1), detail the measurement conditions (Sec. 5.2), analyze the data (Sec. 5.3), and provide a summary in (Sec. 5.4). Our measurements show that the product of the g factor and effective spin dephasing time (gT_s) range from 0.8 ns to 0.1 ns between 40 K and 120 K respectively. Below 40 K, gT_s is approximately constant. The temperature dependence of gT_s shows evidence of thermally activated behavior attributed to hole localization at Bi or Bi cluster sites.

5.1 Motivation

Dilute bismuthides ($GaAs_{1-x}Bi_x$), also known as bismides, are GaAs based semiconductor alloys with many desirable properties. They can be grown on common GaAs substrates, minimally perturb electron mobility, and when combined with nitrogen, can remain lattice matched to GaAs while tuning the bandgap over a broad range.[76, 77, 78] For our purposes, the observation of giant spin-orbit bowing is more intriguing.[79]

The strength of spin-orbit coupling influences both bandstructure and spin dephasing rates, as we saw in Ch. II. GaAsBi alloys hold the promise of a tunable

spin-orbit coupling which is exciting for both academic and engineering purposes. On one hand, we could directly test dephasing mechanism behavior in a single material type, but with various spin-orbit fields. On the other, we could, in principle, optimize the spin-orbit field strength during a device's design phase and then fabricate a product using the appropriate concentration of Bi. With that in mind, we now discuss our experiment that highlights some of the challenges of this material system.

5.2 Experiment Details

GaAsBi epilayers were grown to 100 nm thickness by molecular beam epitaxy at 350° C with a growth rate of $0.1\mu m/hr$ on 500 nm GaAs buffer layers that were grown on semi-insulating (001) GaAs substrates.[1] Details of the sample growth conditions can be found in Refs. [58, 80]. The bandgaps of the respective materials should form a Type I heterojunction shown schematically in Fig. 5.1.

Samples were mounted on the cold-finger of a liquid helium continuous flow cryostat allowing data collection between 10 K and 200 K. PL was excited using a tunable-wavelength mode-locked Ti:Sapphire laser with ∼3 ps pulsewidth and 76 MHz repetition rate. Two excitation wavelengths—ExA = 780 nm (1.59 eV) and ExB = 855 nm (1.45 eV)—were used to selectively excite carriers above (ExA) or below (ExB) the observed GaAs substrate bandgap at all temperatures.

Excitation and collection paths were normal to the sample surface using the PL geometry of Fig. 4.1. The incident beam was focused to a 75 μm diameter cross-section on the sample surface with intensities ranging from 1 W/cm^2 to 250 W/cm^2. A grating spectrometer with 0.2 nm resolution and a liquid nitrogen cooled charge-coupled device (CCD) array were used for analysis.

Hanle effect measurements were conducted with a constant irradiance of 23 W/cm^2 using either ExA or ExB between 10 K and 120 K. Energy dependence of the PL was recorded between 1.30 eV and 1.38 eV with averaging over 4 meV intervals

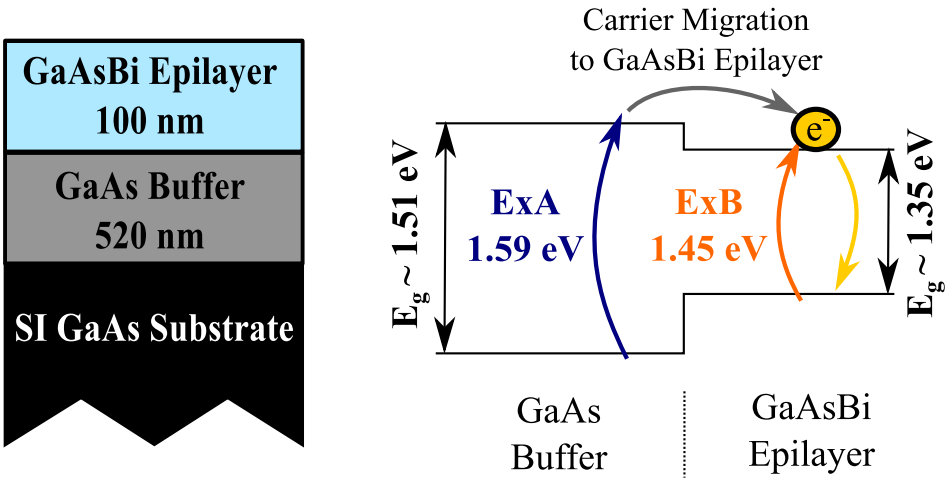

Figure 5.1: (left)Bismuthide sample structure and (right) excitation pathways in the Type I heterojunction. The bandgap of the buffer layer GaAs is approximately 1.51 eV at 10 K, while the bandgap of the GaAsBi layer is estimated to be 1.35 eV.

about a central energy value. An applied magnetic field was varied from -250 mT to +250mT to observe the Hanle effect. Averaging over several complete measurements was performed to improve the signal to noise ratio. Fitting was performed using Eqs. 4.7 and 4.8 with $\phi_0 = \pi/2$ and $\beta_0 = 0$. For reference, the simplified equations with explicit inclusion of the magnetic field (B), g factor (g), Bohr magneton (μ_B), reduced Planck's constant ($\hbar$), dephasing time (τ_s), and recombination time (τ_R) are below.

$$P(B) = \frac{P(0)}{1 + \left(\frac{\mu_B}{\hbar} g T_s B\right)^2} \tag{5.1}$$

$$P(0) = \frac{P_0}{1 + \frac{\tau_R}{\tau_s}}$$

$$\frac{1}{T_s} = \frac{1}{\tau_s} + \frac{1}{\tau_R}$$

5.3 Data Analysis

We first characterized our samples using PL excitation and laser intensity dependence revealing features that are common in other studies of GaAsBi epilayers. We then performed a temperature dependent Hanle effect study on a single $GaAs_{0.992}Bi_{0.008}$ epilayer. We discuss our data and analysis below.

5.3.1 Photoluminescence Characterization

Figure 5.2a shows the laser intensity dependent behavior of the $GaAs_{0.992}Bi_{0.008}$ epilayer using ExB excitation. The PL peak emission monotonically blue shifts with increasing laser intensity, while retaining a low energy tail. In Fig. 5.2b we plot the PL peak emission energy associated with the GaAsBi epilayer versus laser intensity for both ExA and ExB excitation. Both excitation conditions show a blue shift in bismuthide emission with increasing laser intensity. However, ExA PL peak emission energies are consistently higher than ExB PL peak emission energies, and seem to plateau around 100 W/cm^2. In Fig. 5.2c we directly compare the PL spectra from the two excitation conditions allowing us to confirm that ExB does not excite carriers in the GaAs buffer layer, while also observing that $GaAs_{0.992}Bi_{0.008}$ epilayer PL excited by ExA has a broader emission spectra than for ExB excitation. PL measured at 10 K, 40 K, 80 K, and 120 K all exhibit the same laser intensity dependence, though PL intensity diminishes with increasing temperature.

The minimal dependence upon temperature for PL peak emission energy, allows us to discount sample heating as a cause for energy shifts in the peak location. Instead, we attribute the blue shift in GaAsBi emission to the filling of, first, defect and Bi cluster states, then the bandedge states, by photoexcited and migrating carriers. Bi is thought to form cluster sites in GaAs leading to energy states near the valence band. Such sites should lead to hole localization, with a variety of experiments that can be interpreted as having that behavior.[81, 82, 83, 84, 85, 86, 87] Our spin dependent

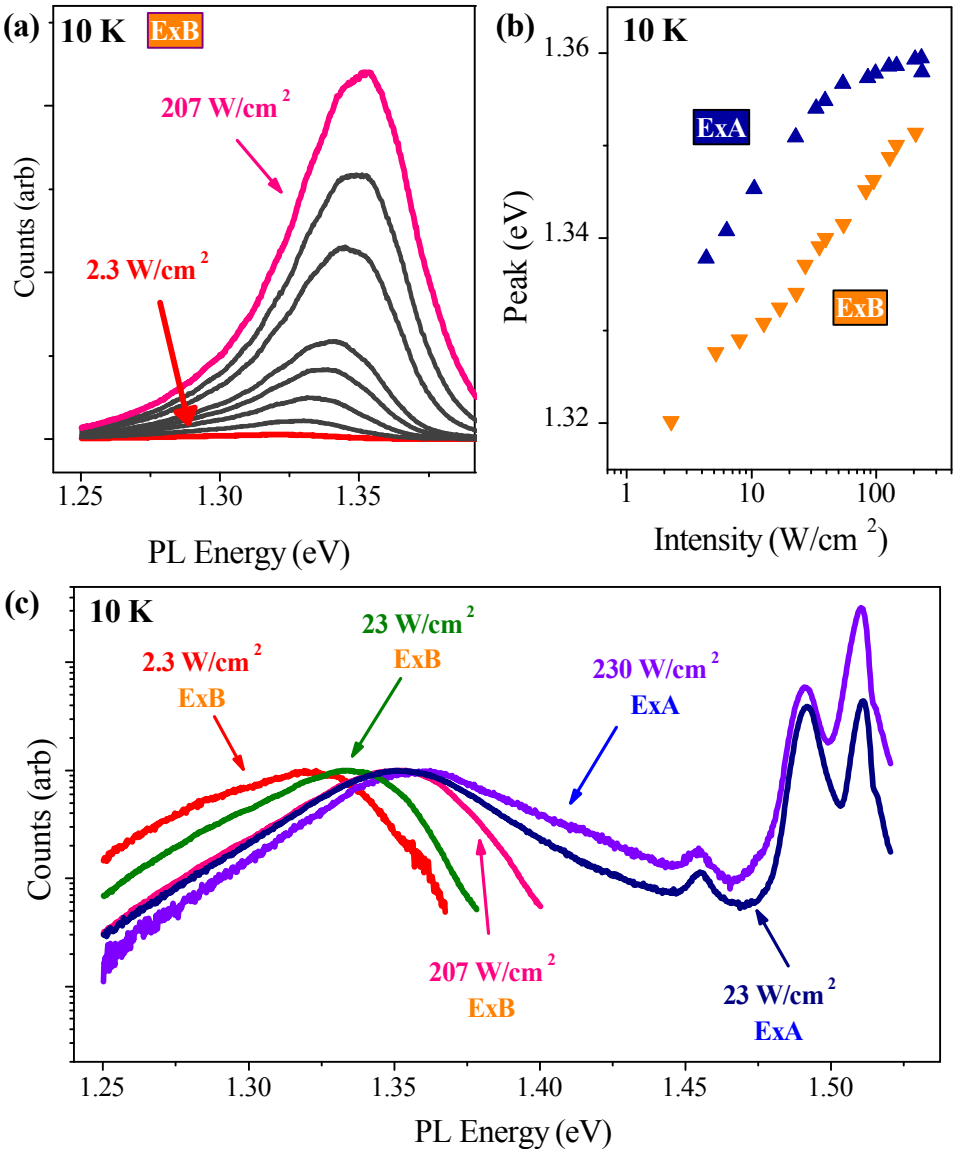

Figure 5.2: Bismuthide PL trends. Shown data collected at 10 K, although the behavior is representative of all PL data collected for 10 K, 40 K, 80 K and 120 K. (a) Laser intensity dependent bismuthide PL for ExB excitation. (b) Energy location of the bismuthide PL peak emission for ExA and ExB excitations as a function of incident laser intensity. (c) Comparison of bismuthide PL spectra for ExA and ExB excitations and selected laser intensities.

measurements show further evidence of hole localization in dilute GaAsBi.

We attribute the linewidth differences between ExA and ExB excitation conditions of the GaAsBi PL emission to carrier migration from the GaAs buffer layer into the GaAsBi epilayer. Carrier transfer is supported by theoretical prediction and experimental observation of Type I heterojunction behavior.[88, 89, 90] Carrier migration can also explain the different GaAsBi peak emission energies for different excitation energy but the same intensity. ExB is below the GaAs bandgap in energy, therefore it cannot excite carriers into the GaAs conduction band and no appreciable migration should occur. ExA is above the GaAs bandgap, therefore it can excite carriers into the GaAs conduction band that can migrate to the GaAsBi epilayer. The result is an increase in the number of carriers in the GaAsBi epilayer for ExA compared to ExB, with the same incident laser intensity. From our above analysis, this should lead to a larger number of defect and cluster states being filled for ExA relative to ExB, and a corresponding blue shift in bismuthide emission which is what we observe.

5.3.2 Hanle Effect Measurements

Figures 5.3a-b shows the temperature dependence of the Hanle curves under ExA and ExB excitation, both with an incident laser intensity of 23 W/cm^2. We observe that as temperature increases, so does the maximum polarization and linewidth of the Hanle curves. ExA Hanle curves are consistently lower in polarization and broader in linewidth than ExB Hanle curves, implying that electron spins dephase more rapidly with ExA compared to ExB. We can attribute such behavior to spin dependent scattering at the GaAs/GaAsBi interface, based on our analysis that carriers migrate from GaAs into the GaAsBi epilayer with ExA excitation. Spin scattering has previously been reported for GaAs/GaNAs and GaAs/ZnSe heterointerfaces.[91, 92]

Figures 5.3c-d show the temperature and emission energy dependence of the maximum polarization under ExA or ExB excitation respectively. Across the majority of

examined emission energies, there is a trend for an increase in polarization with temperature. For the peak emission energies, the polarization increases by over an order of magnitude, regardless of excitation. If we assume that the maximum obtainable PL polarization based on optical selection rules is constant with temperature, this implies that the ratio τ_R/τ_s decreases by over an order of magnitude between 10 K and 120 K (see Eq. 5.1). Moreover, it means that τ_R is at least an order of magnitude larger than τ_s at temperatures below 80 K, allowing us to make the approximation $T_s \simeq \tau_s$ for that low temperature range.

Figures 5.3e-f show the temperature dependent behavior of gT_s under ExA or ExB excitation and for various PL emission energies. The extracted values show a consistent trend of near constant behavior below 40 K followed by a steep decline in magnitude above 40 K, regardless of excitation energy. Such behavior is unexpected as the common D'yakonov-Perel and Elliot-Yafet spin dephasing mechanisms usually exhibit a power law temperature dependence.[93] We were unable to acquire Hanle data beyond 120 K, leaving us with insufficient data to determine if power law behavior is exhibited beyond 40 K. Therefore we focus our efforts on understanding the low temperature behavior.

As discussed above, hole localization appears to be a byproduct of dilute GaAsBi alloys, which we believe explains the temperature dependence of the spin dynamics. Ref. [87] conducted a hole diffusivity experiment for various levels of Bi incorporation and observed evidence of strong hole localization. They quantified the behavior of their sample's diffusion coefficient and radiative recombination time using an Arrhenius function. We will do the same using 5.2 to describe the behavior of gT_s in our sample.

$$\frac{1}{gT_s} = \alpha e^{-\Delta E/kT} + \frac{1}{g\tau_0} \tag{5.2}$$

ΔE is the activation energy, k is Boltzmann's constant, T is temperature in Kelvin,

α is the pre-exponential coefficient, and τ_0 is the 0 K limit of the spin lifetime. Upon fitting (solid black lines in Fig. 5.3), we extract $\Delta E = 33 \pm 8$ meV for ExA and $\Delta E = 40 \pm 6$ meV for ExB excitation Hanle data. These values are comparable to the value of $\Delta E = 46$ meV extracted by Ref. [87]'s Arrhenius function models for radiative recombination and hole diffusion, supporting our model and analysis. While it is possible defects or impurities other than Bi and Bi clusters play a role in localization, Ref. [83] found similar binding energies through PL analysis and, when accounting for phonon behavior, ruled out alternative explanations. Moreover, the growth temperature of 350° C for our samples has been shown to be sufficient for the suppression of As_{Ga} antisites, the leading alternative to Bi sites for carrier localization.[94] A literature search failed to materialize a direct comparison study of shallow localization effects in low temperature growth GaAs versus GaAsBi. If undertaken, such a study could give deeper insight to role of Bi incorporation.

5.4 Summary

In summary, we measured the spin dependent behavior of a 100 nm $GaAs_{0.992}Bi_{0.008}$ epilayer using the Hanle effect with PL detection. Our results show that spin dephasing in our sample is dominated at low temperatures (below 40 K) by hole localization. The hole localization Arrhenius activation energies are found to be $\Delta E = 33 \pm 8$ meV for ExA and $\Delta E = 40 \pm 6$ meV for ExB excitation, comparable to $\Delta E = 46$ meV extracted by Ref. [87] from radiative recombination and hole diffusion measurements. Hole localization is a common feature of dilute GaAsBi epilayers, and complicates the applicability of GaAsBi as a novel spintronic material.

Notes

[1]The sample discussed in this chapter is RMBE809C2

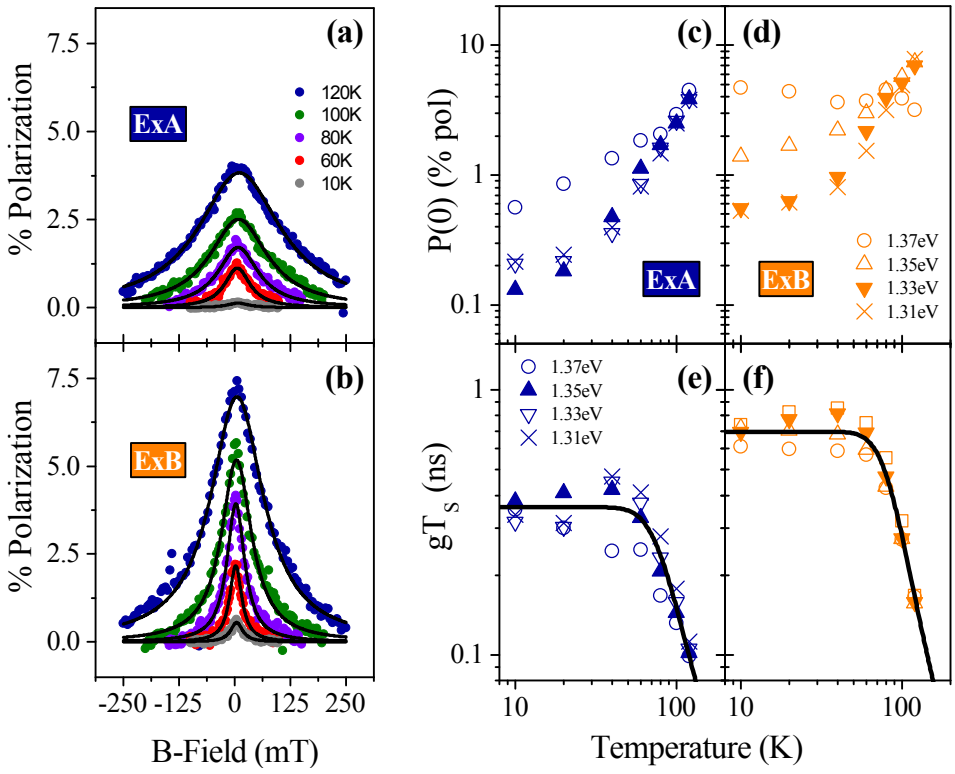

Figure 5.3: Temperature dependent bismuthide Hanle curves evaluated at (a) 1.35 eV PL emission for ExA excitation and (b) 1.33 eV PL emission for ExB excitation, both with an incident laser intensity of 23 W/cm^2. Temperature dependence of the fitting parameters (c,d) $P(0)$ and (e,f) gT_s. The solid black lines are fits to the temperature dependence using an Arrhenius function (Eq. 5.2). The solid navy blue up and orange down triangles respectively correspond to values extracted from Hanle data sets shown in (a) for ExA and (b) for ExB excitation.

CHAPTER VI

Robustness of n-GaAs Carrier Spins to Irradiation

In this chapter, we discuss Resonant Spin Amplification (RSA) measurements of bulk GaAs samples that were exposed to various fluences of 5 MeV protons. The results were published in an original paper, listed as Ref. [95]. We begin with the motivation for the experiment (Sec. 6.1), detail the measurement conditions (Sec. 6.2), analyze the data (Sec. 6.3), and then provide a summary (Sec. 6.4). Our measurements show that GaAs spin dependent optical properties are robust to 5 MeV proton radiation, up to a fluence of 1×10^{14} p/cm^2, even though PL intensity decreases by over two orders of magnitude.

6.1 Motivation

Modern electronics rely upon counting charges and shuffling them from one place to another. We can make digital electronics by labeling a given quantity of charge at a terminal "1" and a reduction of that quantity by more than half "0." As technology has progressed, the minimum quantities of charge required for proper labeling have decreased leading to improved computing speeds and lower power consumption. However, this makes electronic devices more susceptible to fluctuations in charge quantity when exposed to harsh, radiation filled environments.

Radiation, be it gamma rays or ionized particles, can induce large transient fluc-

tuations of charge in a circuit that can scramble digital logic or destroy circuit components. Long term, the energy imparted by radiation on a given device can degrade electronic properties beyond a useful level. Certain earth monitoring satellites can expect a fluence of approximately 10^{11} protons/cm^2 per year, while a detector on the CERN beamline may experience beyond 10^{13} particles/cm^2 per year, be they neutrons or protons.[95, 96]

If information were encoded with electron spins, rather than quantities of electrons themselves, the information should be robust to transient radiation driven events as randomly induced carriers should have a no net polarization. Circuitry could also be optimized for magnetic moment sensitivity while remaining capable of handling large charge fluctuations. There are already many options for spin based logic systems that are actively being pursued.[11, 12, 97, 98, 99, 100, 101, 102, 103] However, it is unclear how the spin properties of semiconductors fare with long-term exposure to irradiation, compared to the known degradation of electronic properties. Our work directly addresses the question of long term spin property stability in the technologically applicable material system of GaAs.

6.2 Experiment Details

All samples we will discuss were cleaved from a 2 in. diameter $\times$ 0.5 mm thick parent wafer of Si-doped n-type GaAs. The manufacturer specifications for the wafer are: (4.3-6.2)$\times10^{16}$/cm^3 carrier concentration, (3450-3880) cm^2/V s mobility, and (2.8-3.9)$\times10^{-2}$ Ω cm resistivity. Seven samples were cut into 4 mm $\times$ 4 mm $\times$ 0.5 mm chips with one held for reference and the other six irradiated at Western Michigan's Van de Graaf accelerator facility. The selected 5 MeV proton fluences were 2.5×10^{12}, 1×10^{13}, 1×10^{14}, 1×10^{15}, 1×10^{16}, and 1×10^{17} protons/cm^2.[1]

All samples were mounted in a continuous flow liquid helium cryostat in order to perform PL characterization at 10 K using 1 W/cm^2 of 1.96 eV emission from a

HeNe laser. PL intensity decreased monotonically with fluence by approximately two orders of magnitude from the reference value till the fluence of 1×10^{14} protons/cm^2. Negligible PL emission was observed for samples exposed to 1×10^{15} p/cm^2 fluence and higher. However, the highest fluence sample emit sufficient gamma radiation for spectral analysis over one month after exposoure. We kept the 1×10^{17} p/cm^2 sample at room temperature and recorded gamma spectra using a high purity Ge solid state detector at the University of Michigan Advanced Physics Teaching Laboratory.

Following PL and gamma characterization, we performed RSA measurements using the Kerr rotation geometry of Fig. 4.5. A wavelength tunable Ti:Sapphire laser with ∼3 ps pulsewidth and 76 MHz repetition rate was split into pump and probe paths. The pump path included a photoelastic modulator providing 50 kHz sinusoidal oscillation between right and left circular polarizations. The probe path included an optical chopper operating at 500 Hz, allowing for cascaded lock-in detection. Probe pulses of 60 W/cm^2 average intensity were delayed by 12.96 ns relative to 420 W/cm^2 average intensity pump pulses with overlapping 30 μm diameter spots on the sample surface. Incident laser energy dependence of the spin dependent material parameters was mapped out between 1.505 eV and 1.538 eV. All spin dependent parameters were extracted from fits using Eq. 4.15, shown below for reference.

$$\theta\left(\Delta t,\Omega\right)=\theta_0 e^{-\Delta t/\tau_s}\frac{\cos\left[\Omega\Delta t\right]-e^{-\Delta t/\tau_s}\cos\left[\Omega\left(\Delta t-t_{rep}\right)\right]}{\sin^2\left[\Omega t_{rep}\right]+\left(\cos\left[\Omega t_{rep}\right]-e^{t_{rep}/\tau_s}\right)^2} \tag{6.1}$$

Δt is fixed at 12.96 ns and $t_{rep}\simeq 13.2$ ns is the repetition period of the laser pulses. $\Omega = \mu_B\, g\, B/\hbar$ where μ_B is the Bohr magneton, g is the Lande g factor, $\hbar$ is the reduced Planck's constant, and B is the applied magnetic field strength.

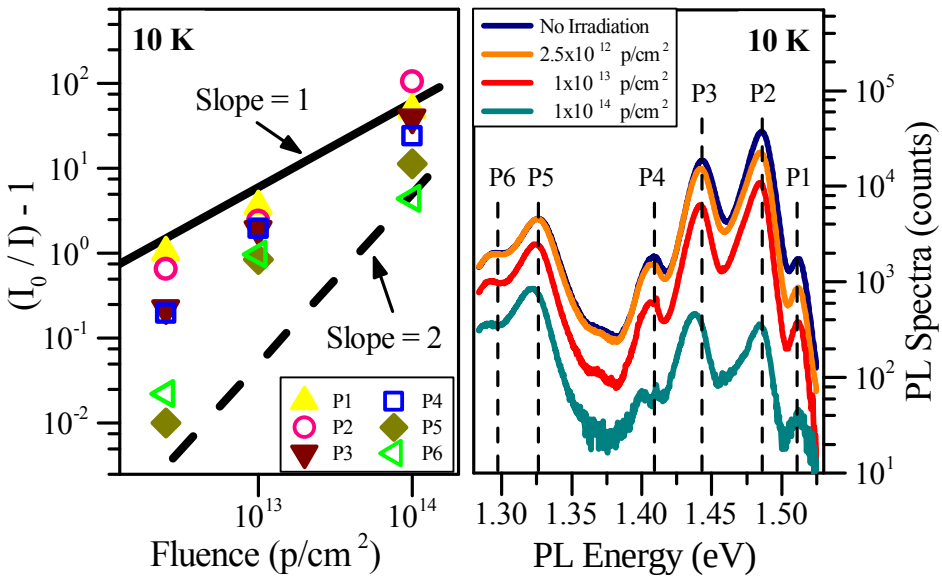

Figure 6.1: (left) Degradation of PL emission peak intensities as a function of fluence. (right) PL spectra of the reference and irradiated n-GaAs samples, up to a fluence of 1×10^{14} p/cm^2. Emission peaks are labeled P1-P6 and correspond to the symbols in the degradation trend figure on the left.

6.3 Data and Analysis

We first characterized our samples using PL and gamma spectra revealing our samples were damaged by irradiation in ways comparable to other reports in the literature. We then performed RSA measurements that show the remarkable resilience of optical spin dependent properties in 5 MeV irradiated n-GaAs. We discuss our data and analysis below.

6.3.1 Photoluminescence Characterization

The right side of Fig. 6.1 shows PL spectra collected from reference and irradiated samples up to a fluence of 1×10^{14} p/cm^2. The emission peaks are labeled P1-P6 and are associated with: band-to-band transitions (P1 = 1.512 eV), excitonic and shallow acceptor transitions (P2 = 1.485 eV), possible phonon replicas of P1 and P2 (P3 = 1.443 eV and P4 = 1.408 eV), and possible impurity bands (P5 = 1.326 eV and P6 = 1.297 eV). The identification of P1 is further supported by comparing the minima

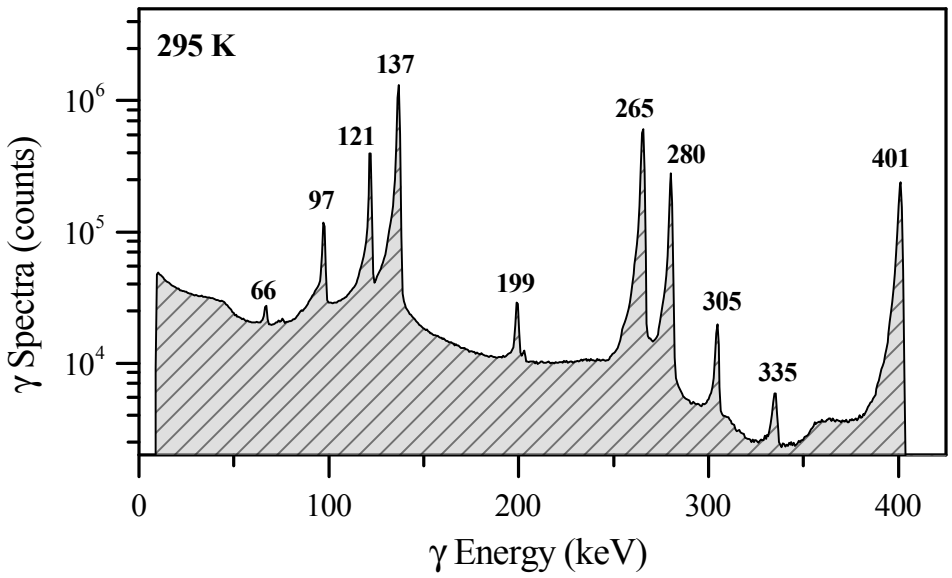

Figure 6.2: Gamma spectra of 10^{17} p/cm^2 fluence irradiated n-GaAs. Spectral peaks are identified by their energy in keV.

in Faraday rotation amplitude θ_0 observed at ∼1.512 eV shown in Fig. 6.3 with the expected behavior from induced linear birefringence shown in Fig. 2.8.

The left side of Fig. 6.1 allows us to evaluate the fluence dependent behavior of the emission peak intensity with Eq. 6.2 from Ref. [104] where I_0 is PL emission intensity *prior* to irradiation, I is the PL emission intensity *after* irradiation, K is the degradation constant, and ϕ is the corresponding fluence. The exponent m is determined by the degradation induced in the sample with $m = 1$ corresponding to mid gap state formation while $m = 2$ corresponds to radiation induced complexes.

$$\frac{I_0}{I} - 1 = K\phi^m \tag{6.2}$$

The degradation slope of PL emission with fluence is linear to modestly superlinear which agrees with the literature for 5 MeV proton irradiation of n-GaAs.[104] In other words, our sample was damaged as expected for the applied fluences.

6.3.2 Gamma Spectra Characterization

Figure 6.2 shows gamma spectra collected from the 10^{17} p/cm^2 fluence irradiated sample, allowing us to better understand any nuclear reactions that took place. The likely culprit of the gamma emission is the decay of ^{75}Se back to ^{75}As. There is only one stable isotope of As (^{75}As) which has a 1.6 MeV barrier for nuclear reaction between an incident proton and a neutron in the As nucleus.[105] ^{75}Se has a half-life of 120 days and the vast majority of the gamma spectra can be attributed to its decay.[106] This has the novel behavior of returning the sample to its original GaAs composition after sufficient time. It should be noted that higher energy protons ($\gtrsim$10 MeV) can lead to substantially more complex nuclear reactions that permanently alter the chemical composition in localized regions.[105]

6.3.3 Resonant Spin Amplification Measurements

Once we had confirmed that our samples were appropriately damaged, we performed RSA at 10 K. Figure 6.3 shows selected laser energy dependent RSA scans of the 1×10^{14} p/cm^2 fluence exposed sample, along with the fitting parameters θ_0, τ_s, and $|g|$ for all samples of exposed to lower fluences. RSA Signal was not obtained in samples exposed to higher fluences.

We can observe that all the samples exhibit an expected laser energy dependence to their maximum measured rotation angle θ_0 which is proportional to the induced linear birefringence (compare to Fig. 2.8). Surprisingly, there is no apparent dependence of the RSA signal upon fluence with the exception of τ_s at the lowest three laser energy data points. We briefly postpone further discussion of the anomalous data.

The magnitudes of g and τ_s, excluding the lowest three laser energies, experience a 2% and 40% increase respectively for the lowest two fluences when compared to the reference values. g and τ_s return to their reference values at the 1×10^{14} p/cm^2 fluence. Such modest behavior, when compared to the orders of magnitude degradation of PL,

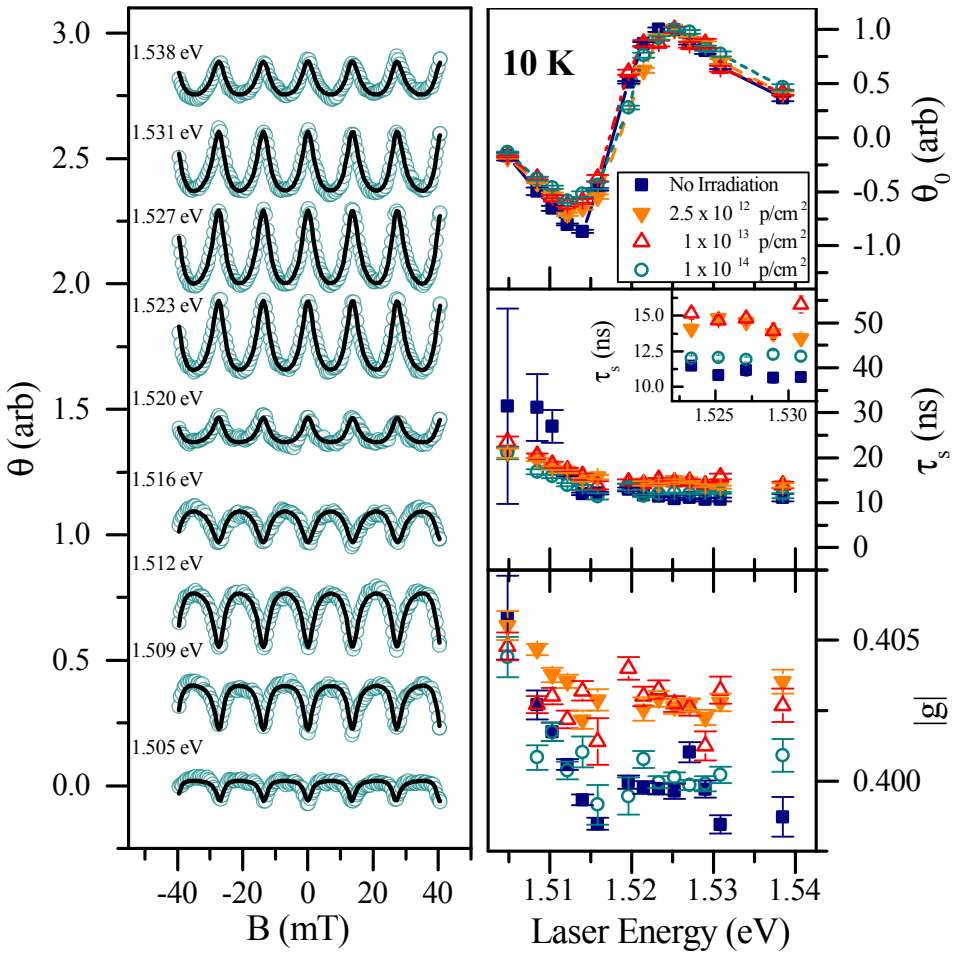

Figure 6.3: (left) Selected resonant spin amplification data for the 1×10^{14} p/cm^2 fluence sample. Fitting curves are shown as solid black lines. (right) Extracted fitting parameters for all samples up to the 1×10^{14} p/cm^2 fluence, as a function of laser energy.

could be attributed to the formation of charge traps via defect states that can alter a sample's carrier density. Low fluences of neutrons have been shown to yield modest improvement in electrical properties, supporting this argument.[107]

Addressing the lowest three laser energy data points, we specifically note the large error bars on the reference sample data points. All data shown for a particular sample was taken on one day with all but the explicitly referenced experiment parameters held constant. The three lowest laser energy data points were retaken on another day with finer resolution field scans, leading to a reduction in the error bar size (data

not shown). However, the central values of the data points did not shift appreciably. Therefore we treat the nearly 10 ns decrease of τ_s from the reference value to the exposed samples as real.

We can explain the behavior as stemming from an enhanced Bir-Aranov-Pikus mechanism due to radiation induced charge traps near the valence band. Beyond modifying the carrier density, the traps can also modify absorption behavior by creating new energy states within the original bandgap. It has been shown that a change in absorbed probe power can lead to a corresponding change in τ_s through an increase in the number of photo-excited holes.[73] The Bir-Aranov-Pikus mechanism improves in efficiency as the number of holes increases due to more efficient exchange interaction from improved wavefunction overlap of electrons and holes. Any changes in efficiency would be expected to be more pronounced for carriers near the bandedges as they have lower momenta leading to longer periods of interaction compared to carriers higher up the band. This could explain why only the three lowest laser energies underwent noticeable change, and at that, only appreciably between the reference sample and the lowest measured fluence.

6.4 Summary

In summary, we measured the spin dependent behavior of irradiated n-type GaAs samples at 10 K using RSA. Our results show that the optically accessible spin dependent properties of n-GaAs are robust to 5 MeV proton irradiation up to a 1×10^{14} p/cm^2 fluence. Dephasing near the bandedge may be influenced by radiation induced charge traps leading to an enhanced Bir-Aranov-Pikus mechanism. Our results show that GaAs is a promising material for further development of radiation resistant spintronic devices.

Notes

[1]The samples discussed in this chapter are:

MTI-001-C2 (reference)

MTI-001-D3 (2.5×10^{12} protons/cm^2)

MTI-001-D4 (1×10^{13} protons/cm^2)

MTI-001-C1 (1×10^{14} protons/cm^2)

MTI-001-C3 (1×10^{15} protons/cm^2)

MTI-001-B2 (1×10^{16} protons/cm^2)

MTI-001-B1 (1×10^{17} protons/cm^2)

CHAPTER VII

Resonant and Time Resolved Spin Noise

Spin noise measurements are powerful and relatively new techniques for accessing spin dependent material parameters (see Sec. 4.4). In this chapter, we discuss two novel implementations of optical spin noise measurements that use a pulsed laser system. Our techniques offer previously unobtainable capabilities including the ability to directly map out the correlation function and achieve significantly improved signal to *background* ratios. We name them as Resonant Spin Noise (RSN) and Time Resolved Spin Noise (TRSN) in direct analogy to Resonant Spin Amplification and Time Resolved Faraday/Kerr Rotation (see Sec. 4.3). The overlap between the conventional and novel techniques extends to much of the optical path. This allows for straightforward implementation through minimal modification of existing TRFR/KR systems.

We begin the chapter by motivating the development of the techniques (Sec. 7.1). We then discuss the overarching measurement concept and its unique standing among conventional methods (Sec. 7.2). We move on to discuss the basics of our model and electronic implementation (Sec. 7.3). From there, we discuss specific experimental cases and develop equations for fitting our data using a single evenly spaced pulse train or two pulse trains separated by a relative time delay (Sec. 7.4). Section 7.5 covers our proof-of-principle measurements for RSN and TRSN, including comparisons to

RSA and Time Resolved Faraday Rotation (TRFR) data collected from the same sample. We conclude the chapter with a summary of our results (Sec. 7.6).

7.1 Motivation

As we saw in Ch. IV, there are a wide variety of existing optical techniques for probing spin dynamics. Each has their own unique strengths and weaknesses, however they all share one trait: they have not shown the ability to measure the spin dynamics of silicon in a contactles, purely optical arrangement. This is not to say that one of the techniques will not improve to achieve such a capability. Nor is it to claim that silicon is the only useful material system that cannot be accessed by the optical methods in Ch. IV. Rather it is a glaring shortcoming that the most widely used material system in modern technology, with distinct promise for future spintronic system development, has not been accessed by the most robust optical methods available.

Lack of optical access hinders the advancement of spintronics by requiring alternate measurement techniques that have reduced spatial resolution (e.g. Electron Spin Resonance) or require extensive sample preparation (e.g. device behavior studies). Electronic device studies have proven useful but require complex and time consuming fabrication—it can take over a month to make working spin injectors *and* detectors for a single batch of devices. The number of components involved in a sample structure more than linearly increase the complexity of fabrication and the possibility of device failure. Moreover, the sample structures themselves can bring complexities and new physical phenomena that cloud the picture. It has been shown that four terminals, each with unique roles, are sufficient to explore novel spin dynamics in silicon.[12] Many measurements of devices with only three terminals have been made, but the validity of those measurements has been called into question with an uncertain outlook for future work.[60, 108, 59]

Therefore, we have sufficient impetus to try a new optical technique. The primary challenge facing optical methods for silicon comes from its indirect gap. An indirect gap requires a photon *and* a phonon, each of appropriate energy and momentum, in order to promote an electron to the conduction band. This translates into more complicated optical selection rules with a subsequently reduced efficiency in spin pumping. The end result is a smaller spin dependent signal that requires resolution beyond available capabilities. If we were to find a way to improve upon the signal to noise ratio of any of the available optical techniques, that may be sufficient to optically probe silicon. It may also open the door to study other difficult material systems with equally small optical signal.

Optical orientation PL studies are not practical in silicon due to weak spin dependent selection rules.[109, 110] Moreover, the measured carrier lifetimes in silicon exceed the predicted and measured spin lifetimes.[111, 112, 113] Recently, the indirect gap material germanium was successfully studied using TRFR.[65, 64, 114] The broad energy spectra of a pulsed laser system exploited the narrow energy separation of the direct and indirect transitions (less than 0.2 eV) in germanium. In this way, they could efficiently pump spins through direct transitions with comparable selection rules to Sec. 2.3.4, let the electrons quickly relax to the indirect conduction band without extensive loss of spin polarization, and then probe the spin behavior of the relaxed carriers. Such a novel experiment is not practical with silicon as the separation between direct and indirect transitions exceeds 2.0 eV with other indirect transitions at lower energies.

We are left with spin noise as a possible optical measurement candidate for silicon and other material systems with small spin dependent signals. Since there is no spin pumping involved, our probe signal should go linearly with optical selection rule efficiency compared to the square for pump-probe methods. This is a major improvement when working with low efficiency spin selection rules. However, as we

discussed in Sec. 4.4, digital processing limits the resolution capabilities of common spin noise techniques. We will now discuss an *analog* signal processing technique that bypasses the digital measurement issues of conventional spin noise, promising orders of magnitude signal to noise improvements while demonstrating novel capabilities.

7.2 The Measurement Concept

RSN and TRSN build off the success of numerous advancements in theory and measurement capabilities dating back to the first observation of Faraday rotation. Many aspects of the new techniques are not new on their own. Instead, it is the novel combination of components that lead to enhanced performance. For instance, the optical path of Ref. [15], including a novel filtering scheme immediately before detection, is the basis for our optical path (see Fig. 7.1). However, we should note that Ref. [15] used digital electronics for signal processing, they did not report their measurements of the correlation function, only its derivative, and their model does not agree with ours, nor most of the existing literature.

A pulsed laser system is required and for all measurements discussed in this chapter, we use a wavelength tunable Ti:Sapphire laser with $\sim$3 ps pulsewidth and 76 MHz repetition rate. An incident beam is split by a beamsplitter (BS) into *two* probe paths where the relative difference in path lengths is controllable. Both paths recombine at a second BS and are coupled into a polarization maintaining fiber optic cable (FOC). The FOC serves one main purpose: to guarantee that both probe pulses overlap spatially for the remainder of the optics path. After passing through a sample mounted in a cryostat, nestled between the poles of an electromagnet, the probe beams are sent through a set of detection optics. The Wollaston prism (WP) and photodiode bridge (PDB) are common to TRFR/KR and conventional spin noise experiments for the detection of a rotated linear polarization. The role of the electro-optic modulator (EOM) immediately *before* the WP and PDB is to filter for spin noise,

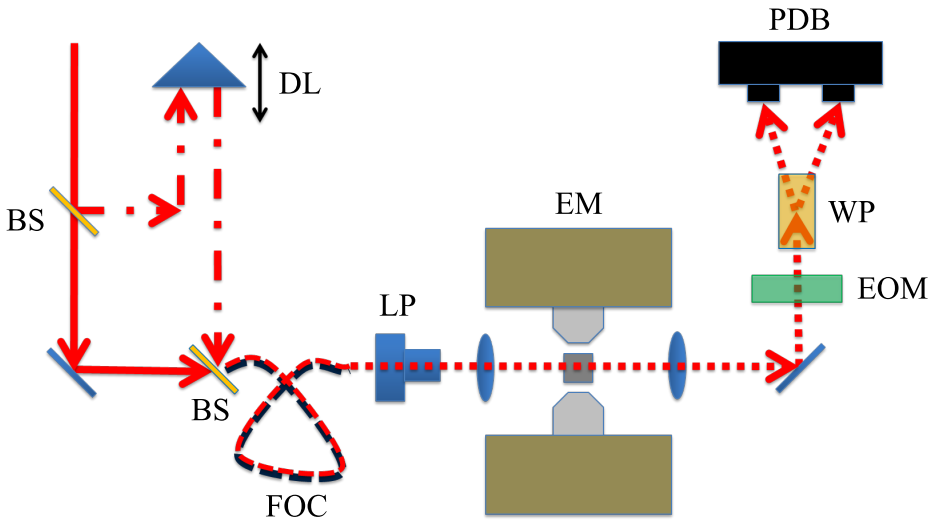

Figure 7.1: Resonant and Time Resolved Spin Noise optics path. The electro-optic modulator (EOM) immediately before the Walloston prism (WP) and photodiode bridge (PDB) acts as a spin noise filter. At 0-retardance, a linear polarization is allowed to propagate and be detected. At $\lambda/4$ retardance, linear polarization is broken into its constituent circularly polarized components leading to no net signal at the PDB. `BS = beamsplitter, DL = delay line, EM = electromagnet, EOM = electro-optic modulator, FOC = fiber optic cable, LP = linear polarizer, PDB = photodiode bridge, WP = Wollaston prism.`

allowing lock-in detection. This is accomplished by alternating the EOM between 0 retardance that allows a linear polarization through unmodified, and $\lambda/4$ retardance where a linear polarization is decomposed into circular polarizations whose intensity is split evenly at the PDB.

We cannot lock-in to a signal that is purely noise, even if we have modulated whether or not we can detect that type of noise. Therefore we require some sort of analog electronic processing that will allow us to achieve a lock-in measurement. For this, we utilize an analog root-mean-square (RMS) circuit that will output a square wave based on our modulation scheme. The processing is shown schematically in Fig. 7.2. We will see shortly that a *mean*-square calculation would yield better measurement results, however we require a circuit that can respond at the repetition

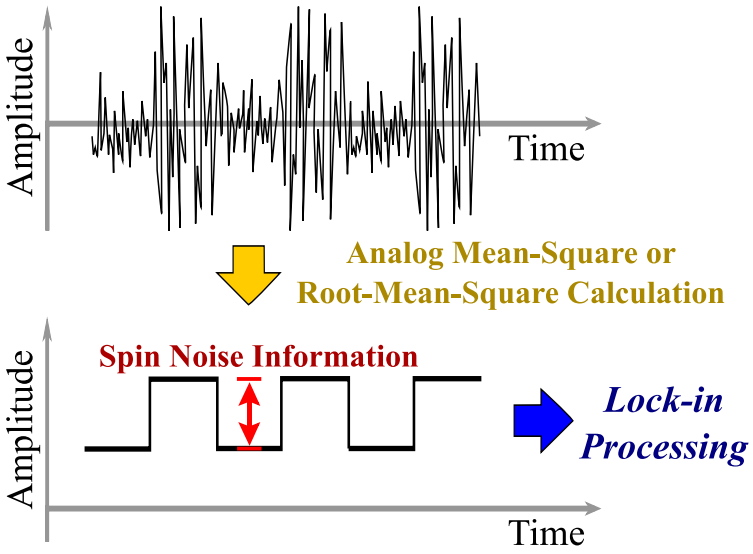

Figure 7.2: Electronic processing concept behind Resonant and Time Resolved Spin Noise. (top) An electrical signal is generated at a photodiode bridge where the presence of spin noise is modulated using a EOM. (bottom) After an analog RMS calculation, a square wave is generated where the amplitude of the modulation (red arrows) contains the spin noise information. The modulation amplitude can now be detected at a lock-in, directly accessing the spin noise information.

rate of the pulsed laser, or faster. We were able to acquire an off-the-shelf testing board from Analog Devices (ADL5511-EVALZ) that was within desired specifications, drastically reducing the time for development and testing of the measurement system.

Though we now have a method for measuring the spin noise *amplitude*, we would like to access the correlation function. This requires achieving a product of two separate measurements in our electrical signal (see Sub. 4.4.1). If we combine a weighted average of signal through the finite electronic response of our circuitry, then perform an analog RMS calculation of the weighted average, the result is a summation over many of our desired product of measurements.

We can visualize the finite response time of an electronic circuit with Fig. 7.3. On the left, we see an idealized pulse response where the electronics are infinitely fast. On the right, we show more realistic behavior where a pulse has a characteristic

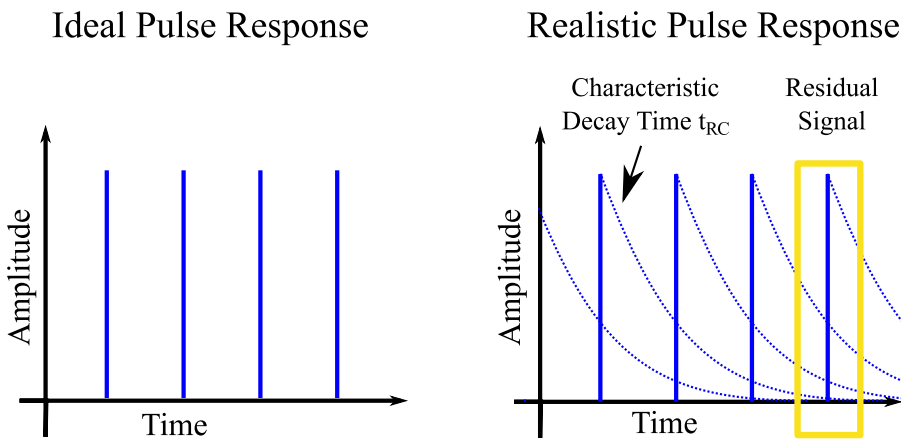

Figure 7.3: (left) An idealized electronic system response where pulsing is completely resolved. (right) Realistic behavior where there is a characteristic decay of the electrical signal after a pulse. The yellow box shows overlap of previous values that have decayed with the most recent pulse. This represents weighted averaging within the electronics of the pulsed signals.

decay in amplitude with a decay time t_{RC}. We choose the subscript "RC" as we consider the response coming from the effective RC-time constant of the combined electronics. We ignore finite rise times as our source of electrical signal is a very short pulse that does not interact with the system very long. We will see shortly that this approximation is acceptable to extract quantitative values from measurements. The yellow box shows overlap of previous pulse values that have decayed with the most recent pulse. This represents weighted averaging within the electronics of the pulsed signals. We assemble the core of our measurement mathematically below.

7.3 Basics of Modeling and Implementation

We only require a few core mathematical components in order to adequately perform our desired measurement. They are a weighted average (X_{WA}), a mean calcu-

lation (μ_X), and a RMS calculation (X_{RMS}), defined below.

$$\begin{aligned} X_{WA} &\equiv \left(\frac{1}{\delta}\int_0^{\delta} dt e^{-t/t_{RC}}\right)\frac{\sum_{n=0}^{\infty} X_n e^{-t_n/t_{RC}}}{\sum_{n=0}^{\infty} e^{-t_n/t_{RC}}} \\ &= \frac{t_{RC}}{\delta}\left(1-e^{-\delta/t_{RC}}\right)\frac{\sum_{n=0}^{\infty} X_n e^{-t_n/t_{RC}}}{\sum_{n=0}^{\infty} e^{-t_n/t_{RC}}} \end{aligned} \tag{7.1}$$

$$\begin{aligned} \mu_X &\equiv \langle X \rangle \\ &= \lim_{N\to\infty}\frac{1}{N}\sum_{n=0}^{N} X_n \end{aligned} \tag{7.2}$$

$$\begin{aligned} X_{RMS} &\equiv \sqrt{\langle X^2 \rangle} \\ &= \sqrt{\lim_{N\to\infty}\frac{1}{N}\sum_{n=0}^{N} X_n^2} \end{aligned} \tag{7.3}$$

There are two main factors to X_{WA}. The first is a scaling factor (integral over continuous time) for the average value obtained over the period δ, the spacing between pulses. The second factor is a *discrete* weighted average where the times t_n do not have to be evenly spaced. δ is dependent upon the time spacing between the 0-th pulse in the sum and the next *future* pulse. The summation is over all *previous* pulses. Both factors contain an exponentially decaying weight that depends upon the circuit response time (t_{RC}). μ_X and X_{RMS} are fairly standard definitions for an average and a RMS respectively.

If we let θ represent the magnitude of spin noise and ξ the magnitude of other sources of noise for a given measurement, we can write our expected signal after lock-in detection as:

$$Signal = [(\theta+\xi)_{WA}]_{RMS} - [\xi_{WA}]_{RMS} \tag{7.4}$$

We now assume $\mu_\theta \sim 0$, which is acceptable for GaAs and many other nonmagnetic semiconductors. We also note that $\langle \theta_{WA} \rangle \sim \mu_\theta$ regardless of how μ_θ is calculated. Assuming $\theta_{RMS} \gg \xi_{RMS}$ and $\mu_\theta \mu_\xi$ we can simplify Eq. 7.4 to

$$Signal = [\theta_{WA}]_{RMS} \tag{7.5}$$

Our assumptions about the size of θ_{RMS} do not help us long term with resolution issues, but they do allow us to perform a proof-of-principle experiment that directly accesses spin dependent behavior. If we were to replace our RMS with a mean-square calculation, than Eq. 7.5 becomes

$$\begin{aligned} Signal &= \left\langle \theta_{WA}^2 \right\rangle + 2\mu_\theta \mu_\xi \\ &\simeq \left\langle \theta_{WA}^2 \right\rangle \end{aligned} \tag{7.6}$$

The last approximation becomes exact if μ_θ *or* μ_ξ is 0. It is Eq. 7.6 that will allow for vast improvements in resolution over existing spin noise methods.

Implementing the necessary analog calculations is straightforward. The weighted averaging X_{WA} can be accomplished by a passive low pass filter or simply the inherent response of the electronic circuitry. The choice of the response time t_{RC} should be sufficiently large to overlap multiple pulse residues, but be kept small enough so as to not include many terms that are negligible due to dephasing. There are a variety of ways to implement analog square or square-root of a square calculations, for which we recommend Ref. [52]. The output of the squaring or root-squaring circuit should be followed by another low-pass filter with a response time much larger than t_{RC}, though not so large as to block the modulation frequency of the spin noise signal. We use a commercial circuit inside the Analog Devices AD5511 chip, more commonly used to measure wireless signal strength, to combine the last two capabilities in a single RMS calculation. We represent the analog calculations schematically in Fig. 7.4

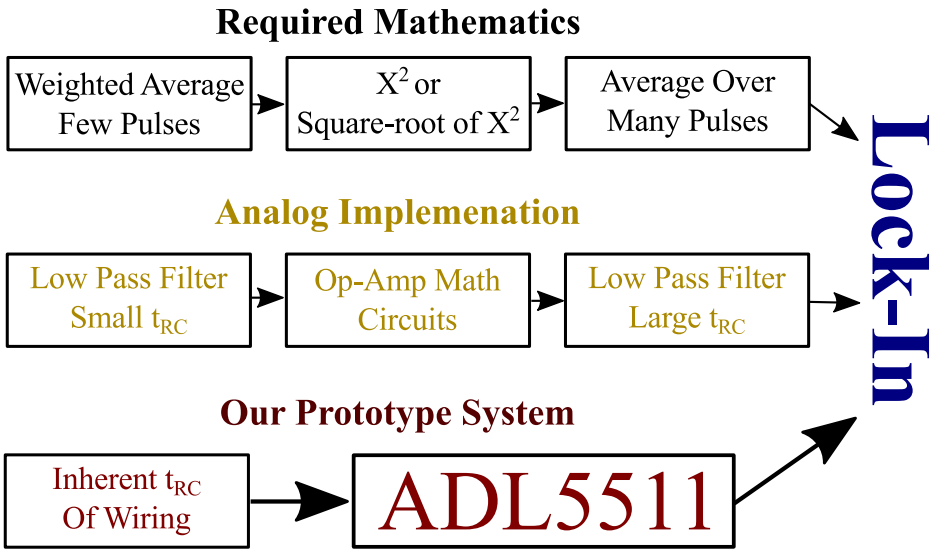

Figure 7.4: Analog calculation schematic showing. (top) A breakdown of the required mathematics. (middle) A rough guideline for analog circuit implementation. Available Op-amp math circuitry should be consulted using Ref. [52]. (bottom) Our implementation of the required components relying upon intrinsic system response and the Analog Devices ADL5511 chip.

7.4 Experiment Specific Models

We are now in a position to assemble a model for specific experimental cases, allowing us to analyze our proof-of-principle measurements. We begin by simplifying our optics path through the removal of the delay line. This yields a single train of equally spaced probe pulses to interrogate the sample. After discussing that simpler case and corresponding measurements, we incorporate the delay line and examine the more interesting signal from two pulse trains with a relative time delay.

7.4.1 Single Pulse Train

We start by combining Eq. 7.5 with our definition Eqs. 7.1, 7.2, and 7.3, along with letting $\delta \to t_{rep}$ where t_{rep} is the laser repetition period. Our resulting equation

is:

$$[\theta_{WA}]_{RMS} = \frac{t_{RC}}{t_{rep}}\left(1 - e^{-t_{rep}/t_{RC}}\right)\sqrt{\frac{\sum_{n,m=0}^{\infty} e^{-(t_n+t_m)/t_{RC}}\,\langle\theta_n\theta_m\rangle}{\sum_{n,m=0}^{\infty} e^{-(t_n+t_m)/t_{RC}}}}$$
$$= \frac{t_{RC}}{t_{rep}}\left(1 - e^{-t_{rep}/t_{RC}}\right)^2\sqrt{\sum_{n,m=0}^{\infty} e^{-(n+m)t_{rep}/t_{RC}}\,\langle\theta_n\theta_m\rangle} \tag{7.7}$$

We now have our desired $\langle\theta_n\theta_m\rangle$ allowing us to access the covariance of our measurements.

At this point, Eq. 7.7 is generally applicable. It is strictly dependent upon the electrical signal processing techniques and some assumptions about the behavior of the θ_i. To make our equation explicitly spin dependent, we note that (see Sec. 4.4)

$$\langle\theta_n\theta_m\rangle = Var(\theta)\, e^{-|t_n - t_m|/\tau_s}\cos\Omega|t_n - t_m| \tag{7.8}$$

Combining Eq. 7.8 with Eq. 7.7 we achieve:

$$[\theta_{WA}]_{RMS} = \frac{t_{RC}}{t_{rep}}\left(1 - e^{-t_{rep}/t_{RC}}\right)^2\sqrt{Var(\theta)}$$
$$\times\sqrt{\sum_{n,m=0}^{\infty}\left[\begin{array}{l} e^{-(n+m)t_{rep}/t_{RC}} \\ \qquad\times e^{-|n-m|t_{rep}/\tau_s}\cos\left(\Omega|n-m|t_{rep}\right)\end{array}\right]} \tag{7.9}$$

Our result is reminiscent of RSA with a sum over many decaying sinusoids. One major difference is the inclusion of the weighting factor:

$$e^{-(n+m)t_{rep}/t_{RC}}$$

If we did not have the weighted summation from a low pass filter, we would have no signal at all, so it plays a visible role in the mathematics. It is worth noting that the only practical tunable parameter for measurement is an applied magnetic field. Time

resolved experiments are not possible unless we have *two* pulse trains with a tunable delay spacing between them.

7.4.2 Two Pulse Trains with Relative Delay

Using the delay line complicates both the measurement system and the modeling, but our reward is a much richer signal and expanded capabilities. We can begin our modeling by thinking of the fixed and delay paths as containing two separate pulse trains with some relative delay. However, we must quickly note that our measurement is continuous since it is analog. Moreover, the relative delay between sequential pulses changes periodically between two values, requiring that we perform *two* weighted average calculations. Immediately after, our circuit will perform a root-square calculation, not RMS. The circuit *then* performs an average over many of the root-square calculations. Therefore we must take a different, but simpler, weighted average of two *separate* root-square calculations of weighted averages over pulses. For clarification, we show the process schematically in Fig. 7.5. The mathematical relationship is written below:

$$[\theta_{WA}]_{RMS} = \frac{\delta_1}{t_{rep}} \sqrt{\left\langle \left[\frac{t_{RC}}{\delta_1} \left(1 - e^{-\delta_1/t_{RC}}\right) \left(\frac{\sum_a \theta_a e^{-t_a/t_{RC}}}{\sum_a e^{-t_{a,n}/t_{RC}}} \right) \right]^2 \right\rangle} + \frac{\delta_2}{t_{rep}} \sqrt{\left\langle \left[\frac{t_{RC}}{\delta_2} \left(1 - e^{-\delta_2/t_{RC}}\right) \left(\frac{\sum_b \theta_b e^{-t_b/t_{RC}}}{\sum_b e^{-t_b/t_{RC}}} \right) \right]^2 \right\rangle} \tag{7.10}$$

with the following definitions

$$\delta_1 \equiv t_{rep} - |\Delta t| \tag{7.11}$$

$$\delta_2 \equiv |\Delta t| \tag{7.12}$$

$$t_a \in \{0, |\Delta t|, t_{rep}, t_{rep} + |\Delta t|, 2t_{rep}, ...\} \tag{7.13}$$

$$t_b \in \{0, t_{rep} - |\Delta t|, t_{rep}, 2t_{rep} - |\Delta t|, 2t_{rep}, ...\} \tag{7.14}$$

We use $\frac{\delta_1}{t_{rep}}$ and $\frac{\delta_2}{t_{rep}}$ as relative weighting factors for averaging over the two pulse spacing cases. We can pull factors out of the averaging and analytically evaluate the denominator summations of Eq. 7.10, leading to:

$$\begin{aligned}[\theta_{WA}]_{RMS} = \frac{t_{RC}}{t_{rep}} \left(1 - e^{-t_{rep}/t_{RC}}\right) \\ \times \left(\frac{1 - e^{-(t_{rep}-|\Delta t|)/t_{RC}}}{1 + e^{-|\Delta t|/t_{RC}}} \sqrt{\sum_{a1,a2} e^{-(t_{a1}+t_{a2})/t_{RC}} \langle \theta_{a1}\theta_{a2} \rangle} \right. \\ \left. + \frac{1 - e^{-|\Delta t|/t_{RC}}}{1 + e^{-(t_{rep}-|\Delta t|)/t_{RC}}} \sqrt{\sum_{b1,b2} e^{-(t_{b1}+t_{b2})/t_{RC}} \langle \theta_{b1}\theta_{b2} \rangle} \right)\end{aligned} \tag{7.15}$$

We use Eq. 7.15, combined with Eq. 7.8 to model two pulse RSN *and* TRSN. For the former, we tune magnetic field and the latter we vary the delay separation Δt.

7.5 Proof-of-Principle Measurements

All proof-of-principle measurements discussed in this chapter involve a single sample cut from a 2 in. diameter × 0.5 mm thick parent wafer of Si-doped n-type GaAs.[1] The manufacturer specifications for the wafer are: (4.3-6.2)×10^{16}/cm^3 carrier concentration, (3450-3880) cm^2/V s mobility, and (2.8-3.9)×10^{-2} Ω cm resistivity. The choice of sample stems from the extensive literature on its spin dependent behavior and the ability to use existing techniques as a reference.

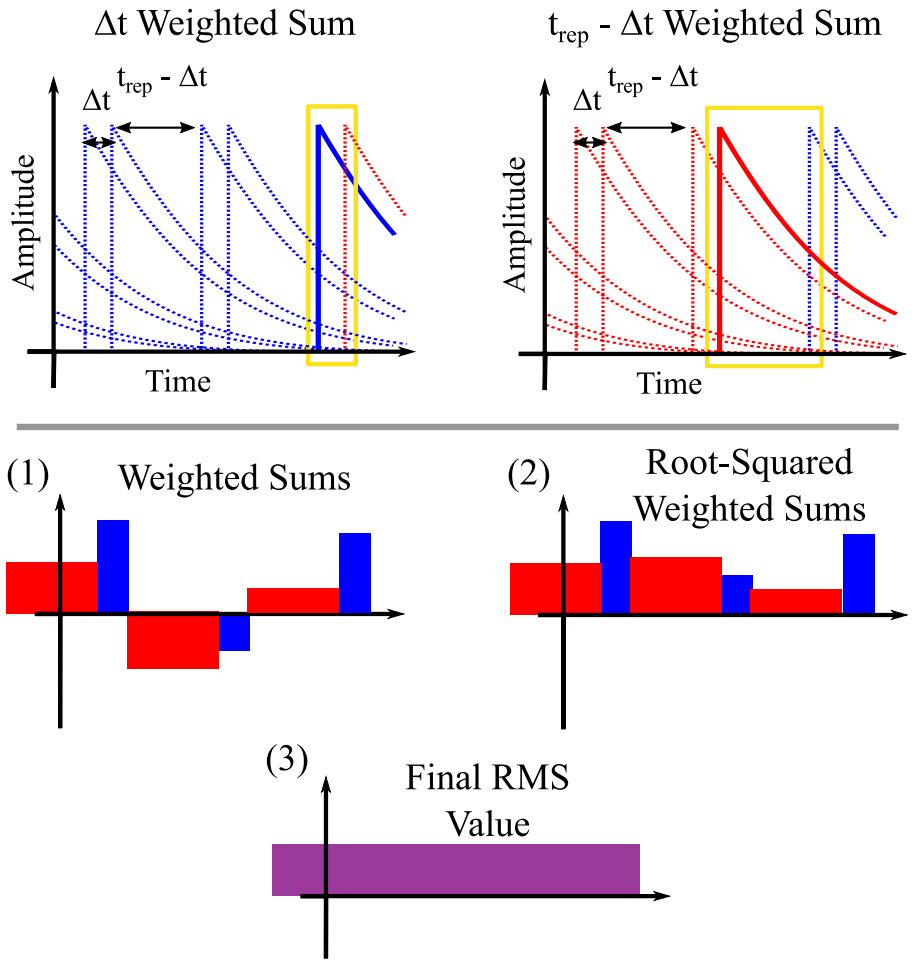

Figure 7.5: Schematic showing two pulse train intervals and calculation process. (top) The two different weighted sum conditions. (bottom) Evaluation process performed by analog electronics with numbers signifying the order of operations.

We used ∼10 mW of incident Ti:Sapphire laser power with ∼2 mW transmission for each linearly polarized laser pulse train. For two pulse train data, this means a total of ∼20 mW was incident upon the sample with ∼4 mW transmitted. We likely perturbed the sample, but our probing conditions kept us within the $\theta_{RMS} \gg \xi_{RMS}$ and $\mu_\theta \mu_\xi$ regime. From wavelength dependent measurements, we chose to operate with $\sim 50\%$ of maximum possible transmission. Therefore a sizable portion of the incident light was likely reflected by the sample and cryostat windows. Wavelengths were shifted appropriately to maintain that condition at all temperatures for all collected data.

At the moment, we have no independent way of determining our system's t_{RC}, therefore we performed RSA on the same sample to extract a dephasing time at 10 K (data not shown) and used t_{RC} as a fitting parameter. The t_{RC} used in all figures comes from an average of different two pulse train measurements at 10 K as the signal has more features leading to improved fitting.

7.5.1 Resonant Spin Noise

Figure 7.6 shows measurements for a single pulse train RSN experiment conducted at 10 K on an n-type GaAs sample. We extracted a g factor of 0.41 in good agreement with RSA extracted values. The model fit using Eq. 7.9, shown as a solid black line, follows the data set quite well.

We explore some of the variety of two pulse train measurements at 10 K in Fig. 7.7. For reference, a larger magnetic field range of single pulse train data with corresponding model are shown. For the two pulse train modeling, we used Eq. 7.15, and extracted $t_{RC} = 29$ ns from the data while holding τ_s fixed to an RSA measured value. The $\Delta t = 2$ ns data shows an interesting beating that our model picks up fairly well. The added features allow for improved extraction of fit parameters as they change at different rates for different dephasing times. Figure 7.8 show temperature dependent

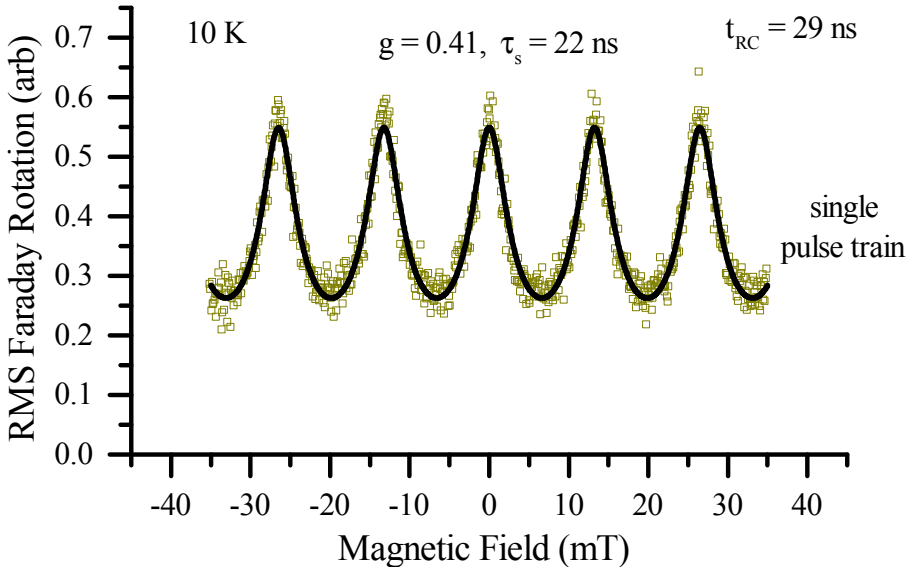

Figure 7.6: Single Pulse Train Resonant Spin Noise

$\Delta t = 2$ ns two pulse train data and associated modeling. We can see the diminishing features as the temperature rises corresponding to a decrease in the dephasing time. We can also see that beyond $\tau_s \sim 1$ ns, it is impractical to fit the data using RSN due to a convergence towards sinusoidal behavior. For large τ_s, RSN using a tunable magnetic field is ideal. Short τ_s require an alternative.

7.5.2 Time Resolved Spin Noise

TRSN is the ideal method to observe short timescale effects, similar to TRFR/KR. Like RSN, we use Eq. 7.9 for modeling, however we fix the applied magnetic field value and tune the relative delay spacing. Figure 7.9 shows temperature dependent TRSN and associated fitting curves. As evidence that only the relative delay matters, the data is symmetric about $\Delta t = 0$. Conceivably, the only limit on resolution is the strength of available magnetic fields and the laser pulsewidth in time.

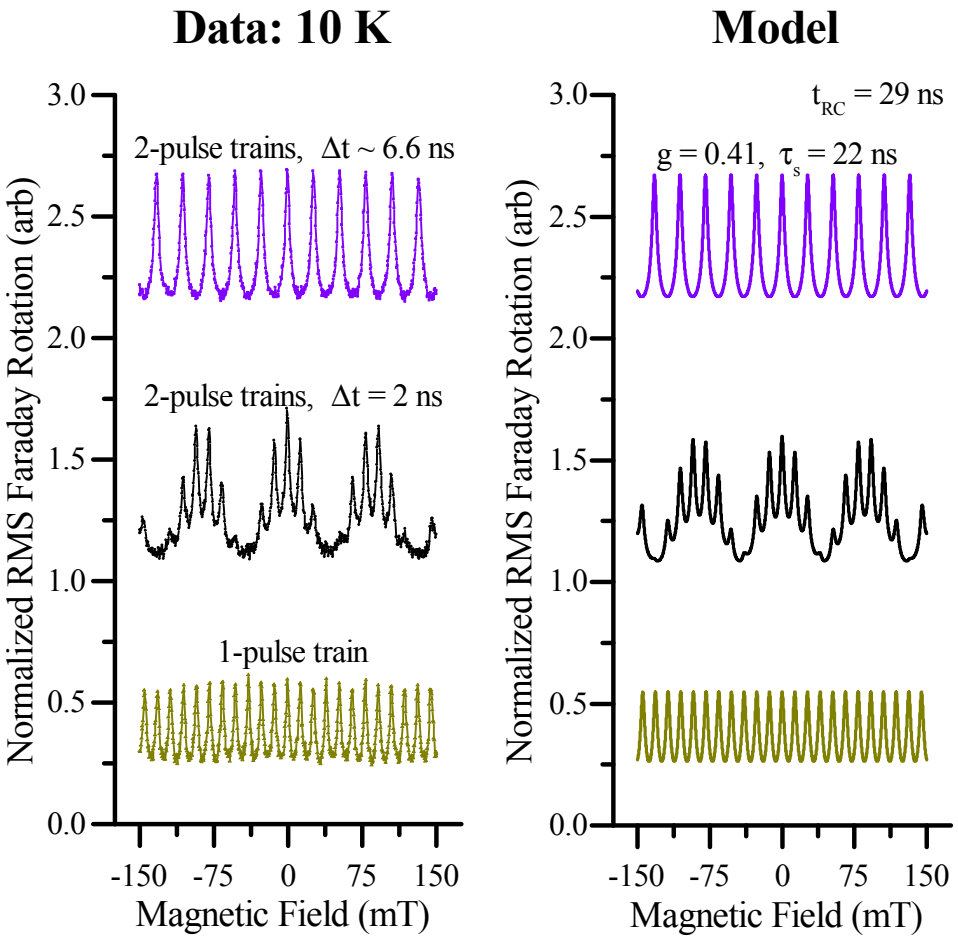

Figure 7.7: Resonant Spin Noise: 10 K, Various Δt. (top) Two pulse trains, $\Delta t \sim 6.6$ ns or half the repetition period. (middle) Two pulse trains, $\Delta t = 2$ ns. (bottom) One pulse train for reference.

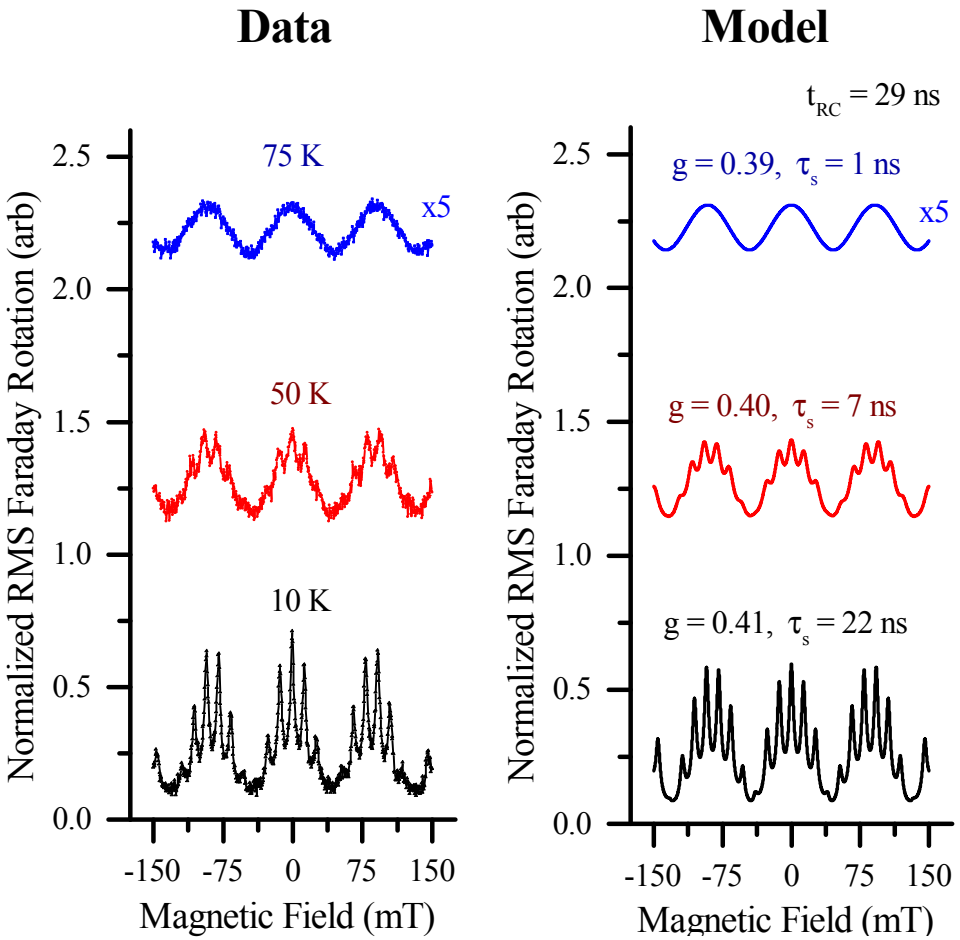

Figure 7.8: Temperature dependent Resonant Spin Noise with Δt = 2ns. (top) 75 K data, scaled by a factor of 5 to improve visibility, (middle) 50 K data, (bottom) 10 K data.

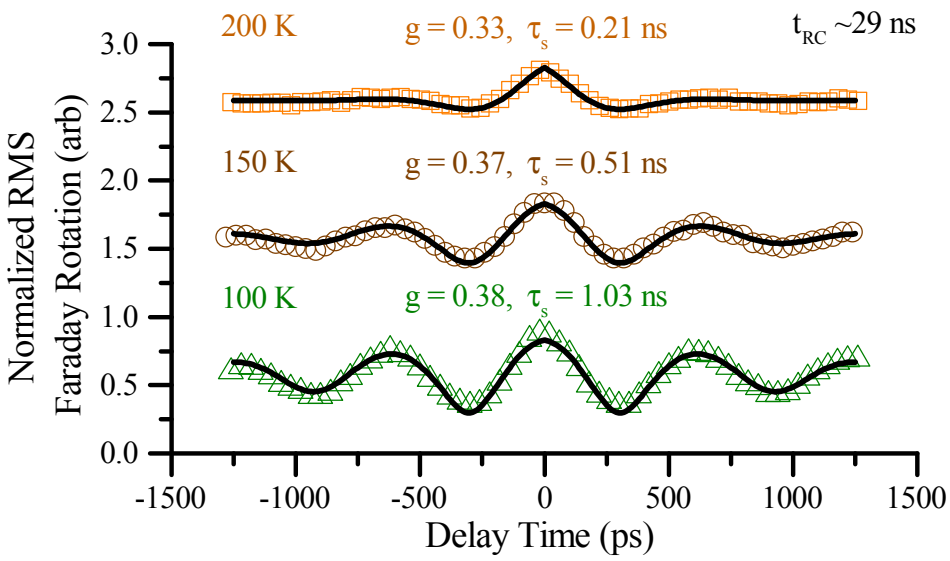

Figure 7.9: Time Resolved Spin Noise with temperature dependence and fits. All fitting curves are shown as black lines. (top) 200 K data and fit, (middle) 150 K data and fit, (bottom) 100 K data and fit.

7.5.3 Comparison with TRFR and RSA

Figure 7.10 compares conventional RSA and TRFR measurements to the novel RSN and TRSN techniques for parameter extraction. We note the use of 10 K RSA data for reference in the extraction of t_{RC}. An improved analog circuit design and access to appropriate test equipment could yield an alternative method for extracting t_{RC}. However, it appears that our use of a conventional method for calibration at a single temperature point gives acceptable results. As we can see, the agreement between methods is quite good through our explored temperature range. We also note the apparent power law behavior, shown as a dashed blue line in Fig. 7.10, where $\tau_s \sim T^{-5/2}$ for 50 K through 200 K. Such behavior implies the dominance of the D'yakonov-Perel dephasing mechanism, influenced by some mixture of phonon and ionized impurity momentum scattering.[93] Below 50 K, other mechanisms for dephasing and momentum scattering are expected to play more prominent roles. Our single data point at 10 K from RSA is insufficient for extraction of details in the low temperature regime. Future work could address the relevant phenomena in more

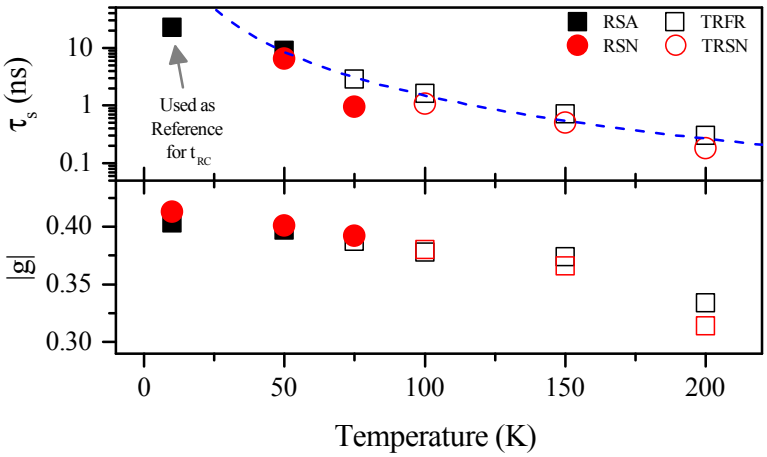

Figure 7.10: A comparison of fit values for RSA and TRFR versus RSN and TRSN. Extracted (top) dephasing times and (bottom) g factors as functions of temperature. The blue dashed line is a power law trend line with $\tau_s \sim T^{-5/2}$ from 50 K to 200 K.

detail, supplementing experimental results in the literature.[115, 116, 63]

At 200 K, the extracted g factor magnitudes are likely less accurate due to the limited strength of our electromagnet. For adequate fitting, the precession period should be at least a factor of two *smaller* than the dephasing time. A field of a few Tesla should be sufficient for extracting g factors up to, and possibly beyond, room temperature in n-GaAs. At 75 K, we note the discrepancy in τ_s between RSN and TRFR. We were restricted to attempting data collection with RSN at 75 K as our stable delay path was too short to acquire a time resolved scan for fitting. This analysis makes our extracted value of τ_s a lower bound with a corresponding upper bound extracted for the amplitude. We will discuss the amplitude in more detail shortly. We were still able to acquire an accurate g factor as, unlike the amplitude, discrepancies in τ_s should not affect its extraction from fitting. Future systems should incorporate modifications that will lead to improved time resolved scanning ranges.

We conclude our analysis with a discussion of the temperature dependence of the RMS Faraday rotation from the spin noise measurements. In Fig. 7.11, if we neglect the 75 K data point, we see an increase in the RMS rotation noise from ~34 μrad to an

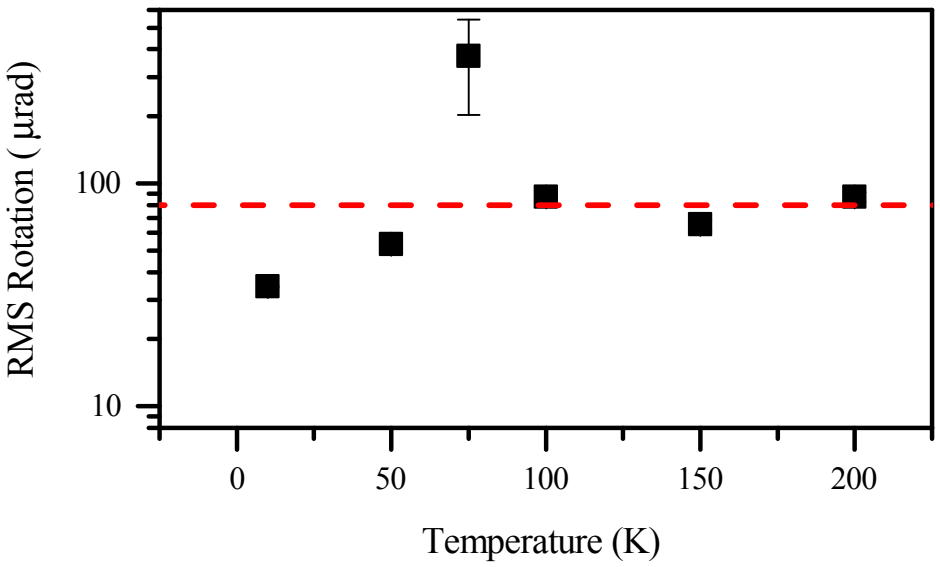

Figure 7.11: Root mean square (RMS) Faraday rotation amplitude temperature dependence for Resonant and Time Resolved Spin Noise data. The red dashed line represents the average maximum RMS rotation, evaluated using 100, 150, and 200 K data. The data point at 75 K is treated as an upper bound for the rotation at that temperature and is neglected from the average maximum rotation calculation.

average peak of ∼80 μrad. The increase in rotation noise below 75 K with subsequent saturation above 75 K agrees with behavior reported and predicted respectively by Ref. [73]. Since our sample doping is near the metal-to-insulator transition, we can assume that the saturation behavior stems from the complete ionization of donor Si atoms, thereby providing a temperature independent carrier density beyond 75 K. Combined with our data, this would imply that our sample's Faraday cross-section, σ_F, can be treated as a constant for the same temperature range. Using Eq. 4.36 with $f = 1$, $n = 5 \times 10^{16}$ cm^{-3}, $d = 500$ μm, and $A = 500$ μm^2, we arrive at an estimate: $\sigma_F \simeq 1 \times 10^{-14}$ rad·cm^2. Our value appears to be in agreement with Ref. [45] and, to the best of our knowledge, is the only other instance of extraction of σ_F. With improved equipment, we believe that models for σ_F could be tested rigorously using RSN and TRSN, leading to a better understanding of Faraday rotation, along with providing key material parameter measurements useful for spintronic engineering.

7.6 Summary

We have discussed the concepts behind RSN and TRSN experiments, along with the mathematical modeling. Proof-of-principle measurements using spin noise in n-GaAs show that the data and modeling agree quite well. Comparison of extracted fitting parameters between RSN/TRSN and RSA/TRFR further show that measurements are quantitatively accurate.

Our novel analog signal processing scheme, the core of our measurement system, is quite general and should be applicable to fields beyond the scope of our expertise. In principle, one must have a pulsed sampling scheme that results in an analog electronic signal, a way to modulate the detection of the desired noise component, a tunable parameter that varies the noise amplitude in an experiment, and the electronic processing outlined in Fig. 7.4. For modeling, all derived equations are applicable, so long as the relevant covariance function is substituted in for $\langle \theta_n \theta_m \rangle$. It is our hope that improvements in the near future will lead to large advancements in the field of spintronics and beyond.

Notes

[1]The sample discussed in this chapter is MTI-001-A2

CHAPTER VIII

Summary and Outlook

In this dissertation, we have revealed an intrinsic material challenge in the promising spintronic system of GaAsBi (Ch. V), highlighted exciting results for future radiation resistant spintronics made from n-GaAs (Ch. VI), and demonstrated a measurement system that may be the key to implementing practical silicon spintronics (Ch. VII). We have attempted to give context to these developments through a discussion of the relevant physics (Ch. II), along with the present state of measurement capabilities (Chs. III and IV). We will now briefly look towards the future.

The right material system is key to the eventual implementation of spintronics. It is safe to say that we have not yet demonstrated the ideal candidate nor the tools necessary to utilize ones that are already available. However, this dissertation has made progress on both fronts. By exploring GaAsBi, we have enhanced the list of available material systems. Even though carrier localization seems to dominate any changes to the dephasing time in GaAsBi, the reduction in hole diffusivity and large changes to spin-orbit coupling may provide a unique platform to study spin helix phenomena.[117] As new growth techniques are attempted and perfected, it may become possible to minimize or remove localization due to Bi clusters, thereby enabling the full spintronic engineering potential of this unique material.

Our work on irradiated n-GaAs provides an encouraging outlook for the replace-

ment of conventional electronics with spin based systems in harsh environments. In performing our study, we have also created an entirely new field with a sea of unanswered questions. Due to the apparent detachment of spin properties from electrical properties in our n-GaAs samples, it is unclear what predictions we can make about the behavior of other irradiated material systems at this point in time. We expect that as the body of experimental knowledge grows regarding the spin behavior of irradiated materials, improvements to our theoretical understanding of spin dephasing mechanisms and defect physics will improve by leaps and bounds.

Our development of Resonant and Time Resolved Spin Noise (RSN and TRSN) is on the leading edge of a new age in optical spin dependent measurements. Our technique is capable of acquiring spin dynamics *and* noise amplitude information in a straightforward manner over a 10 THz bandwidth with existing equipment. Moreover, the ideal sensitivity of our measurement system should allow the study of previously inaccessible materials. We are already attempting measurements of bulk silicon, a long sought after but difficult system for optical study due to predicted properties and robust device fabrication techniques. It is the opinion of the author that it is simply a matter of when, not if, we will be able to optically measure the spin properties of silicon and other difficult materials.

In the near term, the implementation of mean-square circuitry should lead to vast improvements in our signal resolution. Off-the-shelf components are widely available and consultation with practicing electrical engineers could lead to high quality circuitry. In the long term, RSN, TRSN, or a future alternative, could be the workhorse of production lines. It is impractical to test material quality with the fabrication of devices. Realistic assembly lines demand non-demolition characterization and we believe our method currently delivers the widest range of capabilities.

Beyond spintronics development, spin noise measurements have shown that they can provide 3-dimensional resolution of material properties (see Sec. 4.4). We be-

lieve that continuous improvements to spin noise measurement systems will make them a standard tool for conventional electronics development and production. This could potentially simplify a transition to large scale assembly of spintronic devices as the quality control elements would already be in place. A technology revolution is approaching and it will inevitably revolve around spins.

APPENDICES

APPENDIX A

Jones Vectors and Matrices

Jones vectors and matrices allow relatively straightforward calculation of polarization states, assuming the direction of light propagation is constant and that we can neglect the field component along the optical axis. Taking E_X and E_Y to be in the plane orthogonal to propagation, we write

$$\begin{pmatrix} E_X(t) \\ E_Y(t) \end{pmatrix} = e^{i(kz-\omega t)} \begin{pmatrix} E_{0X}e^{i\phi_X} \\ E_{0Y}e^{i\phi_Y} \end{pmatrix} \tag{A.1}$$

where the Jones vector is

$$\begin{pmatrix} E_{0X}e^{i\phi_X} \\ E_{0Y}e^{i\phi_Y} \end{pmatrix} \tag{A.2}$$

We now list various Jones vectors and the matrices that operate on them.

$$\text{Horizontal} \qquad \begin{pmatrix} 1 \\ 0 \end{pmatrix} = \tfrac{1}{2}\left[\begin{pmatrix} 1 \\ i \end{pmatrix} + \begin{pmatrix} 1 \\ -i \end{pmatrix}\right]$$

$$\text{Vertical} \qquad \begin{pmatrix} 0 \\ 1 \end{pmatrix} = \tfrac{1}{2i}\left[\begin{pmatrix} 1 \\ i \end{pmatrix} - \begin{pmatrix} 1 \\ -i \end{pmatrix}\right]$$

$$\text{Right Circular} \quad \tfrac{1}{\sqrt{2}}\begin{pmatrix} 1 \\ -i \end{pmatrix} = \tfrac{1}{\sqrt{2}}\left[\begin{pmatrix} 0 \\ 1 \end{pmatrix} - i\begin{pmatrix} 1 \\ 0 \end{pmatrix}\right]$$

$$\text{Left Circular} \quad \tfrac{1}{\sqrt{2}}\begin{pmatrix} 1 \\ i \end{pmatrix} = \tfrac{1}{\sqrt{2}}\left[\begin{pmatrix} 0 \\ 1 \end{pmatrix} + i\begin{pmatrix} 1 \\ 0 \end{pmatrix}\right]$$

Horizontal Polarizer	$\begin{pmatrix} 1 & 0 \\ 0 & 0 \end{pmatrix}$	Vertical Polarizer	$\begin{pmatrix} 0 & 0 \\ 0 & 1 \end{pmatrix}$
phase retarder	$\begin{pmatrix} e^{i\phi_X} & 0 \\ 0 & e^{i\phi_Y} \end{pmatrix}$	$\frac{\lambda}{2}$-waveplate, fast→horizontal	$\begin{pmatrix} -1 & 0 \\ 0 & 1 \end{pmatrix}$
$\frac{\lambda}{4}$-waveplate, fast→horizontal	$e^{i\pi/4}\begin{pmatrix} 1 & 0 \\ 0 & i \end{pmatrix}$	$\frac{\lambda}{4}$-waveplate, fast→vertical	$e^{i\pi/4}\begin{pmatrix} 1 & 0 \\ 0 & -i \end{pmatrix}$
Counterclockwise Rotation	$\begin{pmatrix} \cos\theta & -\sin\theta \\ \sin\theta & \cos\theta \end{pmatrix}$	Clockwise Rotation	$\begin{pmatrix} \cos\theta & \sin\theta \\ -\sin\theta & \cos\theta \end{pmatrix}$

APPENDIX B

Tips for Acquiring Spin Noise

1. Before fiber coupling on incident path

    - Collimation is key
        - Fiber coupling is one of the trickiest parts of the system, especially with a moving delay line. If the delay path is not collimated *very* well, then the intensity will fluctuate considerably between delay positions.
    - Defocusing can help with fiber coupling
        - By moving the fiber input away from the focus, slight changes in the exact focal position (likely from slight errors in collimation) will have a reduced impact. The cost is attenuation of the output beam due to coupling losses.
        - In some cases, moving the fiber away from the focal point is required. This is especially true with losing mode-lock of the laser from back-reflections. By moving the fiber along the optical path, but away from the focus, any back-reflections become diffuse scatter and do not affect mode-lock.

2. After fiber coupling on incident path

    - Recollimate
        - One cannot count on the fiber output coupler to provide a collimated beam. Place a lens pair after the output coupler and recollimate in order to achieve the smallest spot size possible.
    - Make sure the linear polarizer is at a 45° angle to the Wollaston prism axes.
        - The orientation is critical for achieving the best signal and aligning the polarizer appropriately, as opposed to using a half-wave plate for adjustment, improves stability.

3. At the sample

    - Make sure the sample is at the focal point
        - This is good advice for optics experiments in general, but can be difficult achieve. Note that the sample *center* should be at the focal point, not simply a surface. For transmission of a laser through GaAs at high laser intensity (10 - 20 mW at the sample), a linear polarized beam undegoes a visible rotation and stretching as the sample is moved through the focal point. This provides an excellent reference for alignment. If the sample is at a known focal point, and then imaging with a shallow depth of field is put in place, finding the optimal sample position can become relatively easy–simply move the sample into a position where the image is clear.

4. After the sample

    - Always block the optics path after the sample, until the laser power can be verified to be low enough for safe detection.

  - Damage can occur to the variable retarder and/or the photo-diode bridge if they are exposed to excessive power. A potential damage situation is easily possible during alignment and wavelength adjustment so it is best to put up a beam block *after* the sample, but *before* the retarder and photo-diode bridge when tweaking alignment.

- Alignment of the variable retarder axes, relative to the Wollaston prism axes, is critical.
  - The fast and slow axes should be at a 45° angle relative to the Wollaston prism axes. The probe linear polarization should be oriented along either the fast or slow axes. Any other configuration will lead to reductions in signal. Nothing can be aligned perfectly so the goal is to minimize the signal loss.

- Always check to make sure fiber coupling to the photo-diode bridge is maximized.
  - Slight changes in the probe beam location can lead to losses in signal and skewed rotation values. The same losses and skew can also happen if the fiber positioners migrate. Temperature fluctuations can cause noticeable problems so it is advised to check the positioning periodically throughout a day of data collection, and even better, use thermal insulation.

5. The Electronics

- Unplug BNC cables connected to the analog circuitry while aligning optics
  - The circuitry is sensitive so a spike in signal could fry a component and ruin the board.

- Maximize the gain

– As long as the voltage is not pinned for the output of the board, the measurement has a chance be successful. The larger the final output signal, the better measurements overall.

APPENDIX C

Modeling and Fitting: Mathematica Code

A printout of the Mathematica Code used for modeling and fitting spin noise data makes up the next several pages as reference for future work.

```
Clear["Global`*"]
```

Definitions

Creating a list of pulse times

In[1]:=
```
tsingle[np_, trep_] := Table[i * trep, {i, 0, np}]
ta[np_, trep_, dt_] := Flatten[Table[{i * trep, i * trep + Abs[dt]}, {i, 0, np}]]
tb[np_, trep_, dt_] :=
 Flatten[Table[{i * trep , (i + 1) * trep - Abs[dt]}, {i, 0, np}]]
```

Implementing the single pulse train model

In[4]:=
```
fsingle[trep_, tau_, w_, trc_, sumLim_] :=
 (trc / trep) * (1 - Exp[- trep / trc]) ^ 2 * Sqrt[Total[Flatten[ParallelTable[
      Exp[- (tsingle[sumLim, trep][[i]] + tsingle[sumLim, trep][[j]]) / trc] *
       Exp[- Abs[tsingle[sumLim, trep][[i]] - tsingle[sumLim, trep][[j]]] / tau] *
       Cos[w * Abs[tsingle[sumLim, trep][[i]] - tsingle[sumLim, trep][[j]]]],
      {i, 1, sumLim}, {j, 1, sumLim}]]]]
```

Implementing the two pulse train model

In[5]:=
```
fdouble[dt_, trep_, tau_, w_, trc_, sumLim_] :=
 (trc / trep) * (1 - Exp[- trep / trc]) *
   ((1 - Exp[- (trep - Abs[dt]) / trc]) / (1 + Exp[- Abs[dt] / trc])) * Sqrt[
    (Total[Flatten[ParallelTable[
        Exp[- (ta[sumLim, trep, dt][[i]] + ta[sumLim, trep, dt][[j]]) / trc] *
         Exp[- Abs[ta[sumLim, trep, dt][[i]] - ta[sumLim, trep, dt][[j]]] / tau] *
         Cos[w * Abs[ta[sumLim, trep, dt][[i]] - ta[sumLim, trep, dt][[j]]]],
        {i, 1, sumLim}, {j, 1, sumLim}]]])] +
  (trc / trep) * (1 - Exp[- trep / trc]) * ((1 - Exp[- Abs[dt] / trc]) /
     (1 + Exp[- (trep - Abs[dt]) / trc])) * Sqrt[
    (Total[Flatten[ParallelTable[
        Exp[- (tb[sumLim, trep, dt][[i]] + tb[sumLim, trep, dt][[j]]) / trc] *
         Exp[- Abs[tb[sumLim, trep, dt][[i]] - tb[sumLim, trep, dt][[j]]] / tau] *
         Cos[w * Abs[tb[sumLim, trep, dt][[i]] - tb[sumLim, trep, dt][[j]]]],
        {i, 1, sumLim}, {j, 1, sumLim}]]])]
```

Defining functions with a finite number of pulses in the summation

In[6]:=
```
fSingle16[trep_, tau_, w_, trc_] = fsingle[trep, tau, w, trc, 16];
```

In[7]:=
```
fDouble32[dt_, trep_, tau_, w_, trc_] = fdouble[dt, trep, tau, w, trc, 32];
```

Function Behavior

Amplitude behavior as function of trc in units of trep

In[9]:=
```
Plot[ (trc) * (1 - Exp[-1 / trc]) ^2, {trc, 0.0001, 10}]
```

Out[9]=

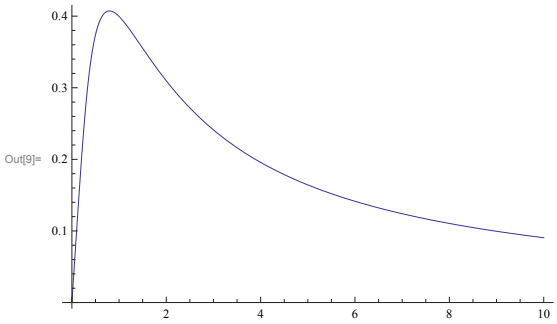

In[8]:=
```
Plot[fDouble32[2000, 13157.89, 22360, (8.7941 * 10^-5) * 0.4 * (w), 30000]^2,
 {w, -150, 150}]
```

Out[8]=

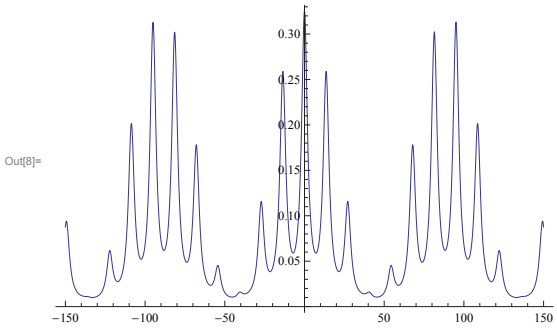

In[12]:=
```
Plot[{fDouble32[dt, 1, 0.05, 0, 3]}, {dt, -1, 1}, PlotRange → All]
```

Out[12]=

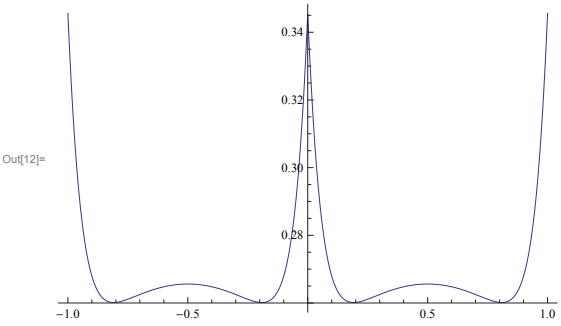

Data

```
highRes10K = Import["C:\\Users\\bpursley\\Box
      Sync\\SihLab-Selected\\Publications\\Papers\\SpinNoise_2014-2015\\
      Figures\\RSN_10K_HiRes_ForFits.dat"];
```

```
ListPlot[highRes10K, PlotRange → All]
```

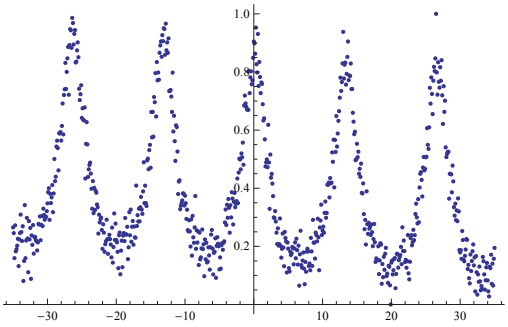


```
RSNvaried10K = Import["C:\\Users\\bpursley\\Box
      Sync\\SihLab-Selected\\Publications\\Papers\\SpinNoise_2014-2015\\
      Figures\\RSN_10K_varied_ForFits.dat"];
```

```
RSNsinlgle10K = Table[{RSNvaried10K[[i]][[1]], RSNvaried10K[[i]][[2]]},
   {i, 1, Length[RSNvaried10K]}];
RSNdouble2ns10K = Table[{RSNvaried10K[[i]][[1]], RSNvaried10K[[i]][[3]]},
   {i, 1, Length[RSNvaried10K]}];
RSNdoubleTwiceRep10K = Table[{RSNvaried10K[[i]][[1]], RSNvaried10K[[i]][[4]]},
   {i, 1, Length[RSNvaried10K]}];
```

```
ListPlot[
 {RSNsinlgle10K, RSNdouble2ns10K + 1, RSNdoubleTwiceRep10K + 2}, PlotRange → All]
```

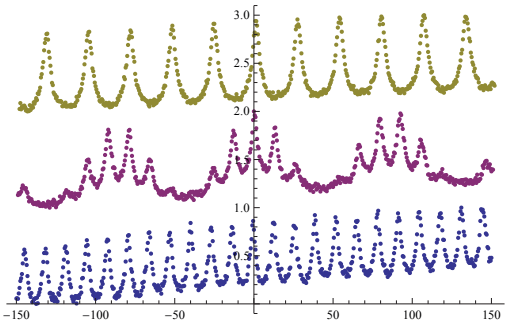

```
RSNvaried50and75K = Import["C:\\Users\\bpursley\\Box
      Sync\\SihLab-Selected\\Publications\\Papers\\SpinNoise_2014-2015\\
      Figures\\RSN_50K_and_75K_varied_ForFits.dat"];

RSNdouble2ns50K =
  Table[{RSNvaried50and75K[[i]][[1]], RSNvaried50and75K[[i]][[2]]},
   {i, 1, Length[RSNvaried50and75K]}];
RSNdouble2ns75K = Table[{RSNvaried50and75K[[i]][[1]],
    RSNvaried50and75K[[i]][[3]]}, {i, 1, Length[RSNvaried50and75K]}];

ListPlot[{RSNdouble2ns50K, RSNdouble2ns75K + 1}, PlotRange → All]
```

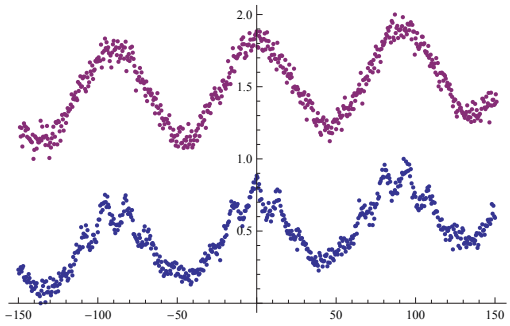


```
TRSNfrom100to200K = Import["C:\\Users\\bpursley\\Box
      Sync\\SihLab-Selected\\Publications\\Papers\\SpinNoise_2014-2015\\
      Figures\\TRSN_100-200K_DataForFits.dat"];

TRSNdouble100K =
  Table[{TRSNfrom100to200K[[i]][[1]], TRSNfrom100to200K[[i]][[2]]},
   {i, 1, Length[TRSNfrom100to200K]}];
TRSNdouble150K = Table[{TRSNfrom100to200K[[i]][[1]],
    TRSNfrom100to200K[[i]][[3]]}, {i, 1, Length[TRSNfrom100to200K]}];
TRSNdouble200K = Table[{TRSNfrom100to200K[[i]][[1]],
    TRSNfrom100to200K[[i]][[4]]}, {i, 1, Length[TRSNfrom100to200K]}];

ListPlot[{TRSNdouble100K, TRSNdouble150K + 1, TRSNdouble200K + 2}, PlotRange → All]
```

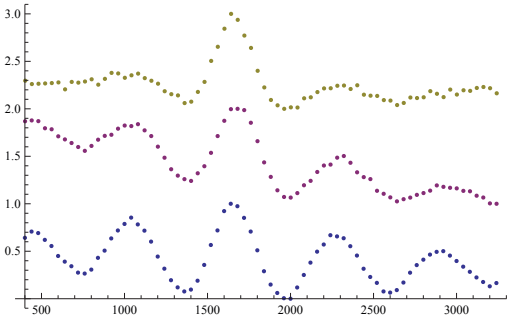

Fitting

10 K Two Pulse Train RSN 2 ns -- tau = 22.360 ns (Xin's data, April 8)

```
modelDoubleTau = mag * fDouble32[2000, 13157.89, 22360,
      (8.7941 * 10^-5) * g * (bfield - b0), trc] + y0 + y1 * bfield;

fitForRSNdouble2ns10KTau = NonlinearModelFit[RSNdouble2ns10K, {modelDoubleTau,
    {mag > 0, 0.30 <= g <= 0.45, trc > 13157.89, -2 <= b0 <= 2}},
  {{mag, 1.4}, {g, 0.41}, {trc, 60000}, {y0, 0}, {b0, -1}, {y1, 0}},
  bfield, MaxIterations -> 5000, PrecisionGoal -> 10]
fitForRSNdouble2ns10KTau["ParameterTable"]
Show[ListPlot[RSNdouble2ns10K, PlotRange -> All],
 Plot[fitForRSNdouble2ns10KTau[bfield],
  {bfield, -150, 150}, PlotStyle -> Directive[Thick, Red]]]
ListPlot[fitForRSNdouble2ns10KTau["FitResiduals"], Filling -> Axis]
```

FittedModel[

$$-0.0594498 + \ll 22 \gg \ll 6 \gg + 1.52468\left(0.149983\sqrt{(2.75427 + 2.50971\,\text{Cos}[0.0723869\,(0.704932 + \text{bfield})] + \ll 44 \gg + 6.05915\times10^{-8}\,\text{Cos}[7.21583\,(0.704932 + \text{bfield})]) + 0.0381617\sqrt{\ll 19 \gg + \ll 45 \gg + \ll 23 \gg \ll 1 \gg}}\right)$$

]

FittedModel::constr :

The property values (ParameterTable) assume an unconstrained model. The results for these properties may not be valid, particularly if the fitted parameters are near a constraint boundary. ≫

	Estimate	Standard Error	t-Statistic	P-Value
mag	1.52468	0.0153444	99.364	$1.081663321960\times10^{-372}$
g	0.411565	0.000168196	2446.94	$4.893775706940\times10^{-1193}$
trc	23745.7	921.502	25.7685	6.48934×10^{-99}
y0	−0.0594498	0.00592237	−10.0382	5.20091×10^{-22}
b0	−0.704932	0.0316195	−22.2942	1.69141×10^{-80}
y1	0.000901125	0.0000199399	45.192	1.55882×10^{-194}

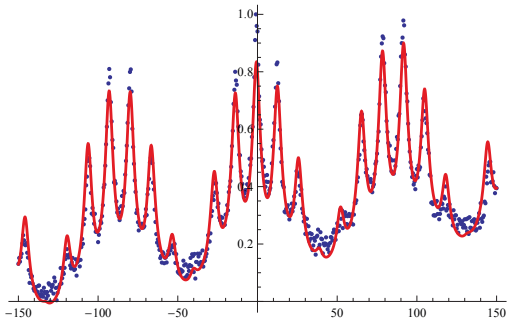

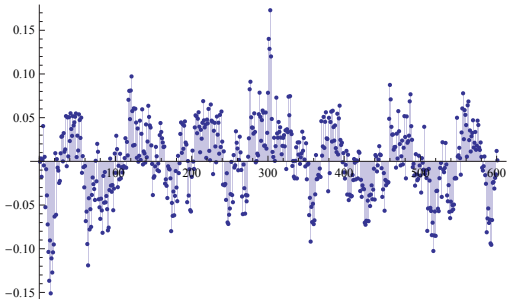

10 K Twice Rep Rate Two Pulse RSN -- tau = 22.360 ns (Xin's data, April 8) **Double Model**

```
13157.89 / 2
```

```
6578.95
```

```
modelDoubleTwiceRepTau = mag * fDouble64[6578.95, 13157.89,
      22360, (8.7941 * 10^-5) * g * (bfield - b0), trc] + y0 + y1 * bfield;

fitForRSNdoubleTwiceRep10KTau =
 NonlinearModelFit[RSNdoubleTwiceRep10K, {modelDoubleTwiceRepTau,
    {mag > 0, 0.30 <= g <= 0.45, trc > 10000, -2 <= b0 <= 2}},
  {{mag, 1}, {g, 0.41}, {trc, 30000}, {y0, 0}, {b0, -1}, {y1, 0}},
  bfield, MaxIterations -> 1000, PrecisionGoal -> 10]
fitForRSNdoubleTwiceRep10KTau["ParameterTable"]
Show[ListPlot[RSNdoubleTwiceRep10K, PlotRange -> All],
 Plot[fitForRSNdoubleTwiceRep10KTau[bfield],
  {bfield, -150, 150}, PlotStyle -> Directive[Thick, Red]]]
ListPlot[fitForRSNdoubleTwiceRep10KTau["FitResiduals"], Filling -> Axis]
```

$$\text{FittedModel}\left[\begin{array}{l} -0.111179 + \ll 22 \gg \text{ bfield} + \\ 1.79757\left(0.0797124\sqrt{(3.12661 + 2.28706\,\text{Cos}[0.237324\,(0.656846 + \text{bfield})] + \ll 92 \gg +} \right. \\ \left. \qquad 9.50866\times 10^{-14}\,\text{Cos}[14.9515\,(0.656846 + \text{bfield})]\right) + 0.0797123\sqrt{\ll 1 \gg}\,\Big) \end{array}\right]$$

FittedModel::constr :

The property values {ParameterTable} assume an unconstrained model. The results for these properties may not be valid, particularly if the fitted parameters are near a constraint boundary. ≫

	Estimate	Standard Error	t-Statistic	P-Value
mag	1.79757	0.0117531	152.944	$7.87730614535\times 10^{-480}$
g	0.4102	0.0000552147	7429.18	$5.275114805391\times 10^{-1480}$
trc	34139.	974.275	35.0405	8.84129×10^{-147}
y0	−0.111179	0.00412606	−26.9456	3.86758×10^{-105}
b0	−0.656846	0.011279	−58.236	6.22852×10^{-248}
y1	0.000793587	0.0000107499	73.8227	9.88402×10^{-302}

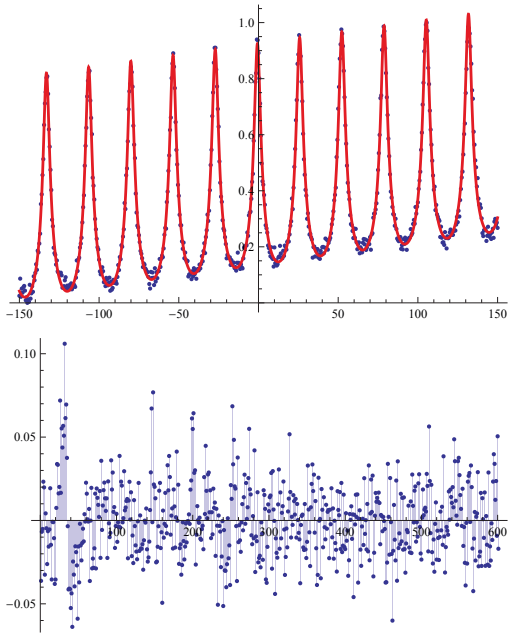

10 K Twice Rep Rate Two Pulse RSN -- tau = 22.360 ns (Xin's data, April 8) **Single Model**

```
modelSingleTwiceRepTau =
  mag * fSingle64[6578.95, 22 360, (8.7941 * 10^-5) * g * (bfield - b0), trc] +
   y0 + y1 * bfield;
```

```
fitForRSNsingleTwiceRep10KTau =
 NonlinearModelFit[RSNdoubleTwiceRep10K, {modelSingleTwiceRepTau,
    {mag > 0, 0.30 <= g <= 0.45, trc > 10 000, -2 <= b0 <= 2}},
  {{mag, 1}, {g, 0.41}, {trc, 30 000}, {y0, 0}, {b0, -1}, {y1, 0}},
  bfield, MaxIterations -> 1000, PrecisionGoal -> 10]
fitForRSNsingleTwiceRep10KTau["ParameterTable"]
Show[ListPlot[RSNdoubleTwiceRep10K, PlotRange -> All],
 Plot[fitForRSNsingleTwiceRep10KTau[bfield],
  {bfield, -150, 150}, PlotStyle -> Directive[Thick, Red]]]
ListPlot[fitForRSNsingleTwiceRep10KTau["FitResiduals"], Filling -> Axis]
```

FittedModel[−0.111179 + 0.000793587 bfield + 0.286577 √(3.12661 + 3.84263 Cos[0.237325 (0.656846 + bfield)] + ≪61≫ + 9.50865×10^−14 Cos[14.9515 (0.656

FittedModel::constr :
The property values (ParameterTable) assume an unconstrained model. The results for these properties may not be valid, particularly if the fitted parameters are near a constraint boundary. ≫

	Estimate	Standard Error	t-Statistic	P-Value
mag	1.79757	0.0117531	152.944	$7.88645447629\times10^{-480}$
g	0.410199	0.0000552146	7429.18	$5.275120234344\times10^{-1480}$
trc	34 139.1	974.278	35.0404	8.84539×10^{-147}
y0	−0.111179	0.00412606	−26.9456	3.86757×10^{-105}
b0	−0.656846	0.011279	−58.236	6.22855×10^{-248}
y1	0.000793587	0.0000107499	73.8227	9.88402×10^{-302}

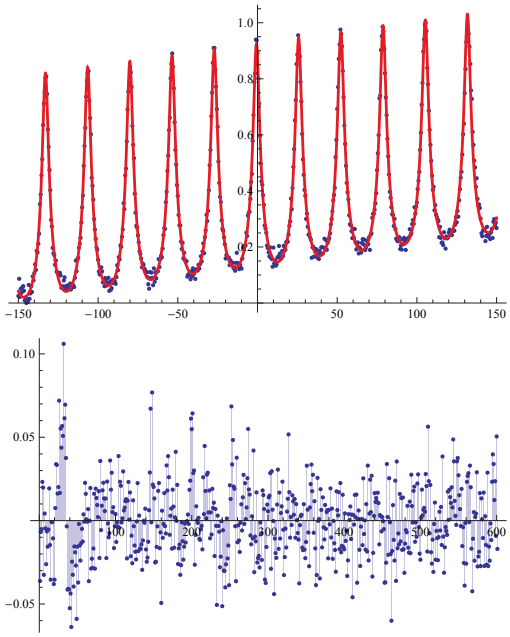

10 K Twice Rep Rate Two Pulse RSN -- tau = 22.360 ns (Xin's data, April 8) **Double Model** **trc = 29 +/-1 ns

```
modelDoubleTwiceRepTau29 = mag * fDouble64[6578.95, 13157.89, 22360,
      (8.7941 * 10^-5) * g * (bfield - b0), 29000] + y0 + y1 * bfield;

fitForRSNdoubleTwiceRep10KTau29 = NonlinearModelFit[RSNdoubleTwiceRep10K,
  {modelDoubleTwiceRepTau29, {mag > 0, 0.30 <= g <= 0.45, -2 <= b0 <= 2}},
  {{mag, 1}, {g, 0.41}, {y0, 0}, {b0, -1}, {y1, 0}},
  bfield, MaxIterations -> 5000, PrecisionGoal -> 10]
fitForRSNdoubleTwiceRep10KTau29["ParameterTable"]
Show[ListPlot[RSNdoubleTwiceRep10K, PlotRange -> All],
 Plot[fitForRSNdoubleTwiceRep10KTau29[bfield],
  {bfield, -150, 150}, PlotStyle -> Directive[Thick, Red]]]
ListPlot[fitForRSNdoubleTwiceRep10KTau29["FitResiduals"], Filling -> Axis]
```

NonlinearModelFit::eit :

The algorithm does not converge to the tolerance of 4.806217383937354`*^-6 in 5000 iterations. The best estimated solution, with feasibility residual, KKT residual, or complementary residual of $\{7.40313\times10^{-7}, 0.0000313379, 2.15894\times10^{-7}\}$, is returned. ≫

FittedModel[

$$-0.133661 + \ll22\gg \ll6\gg + 1.75189\left(0.0907959\sqrt{(2.74168 + 1.99138\,\text{Cos}[0.237324\,(0.656348 + \text{bfield})] + \ll92\gg + 1.10602\times10^{-14}\,\text{Cos}[14.9514\,(0.656348 + \text{bfield})]) + 0.0907958\sqrt{\ll19\gg + \ll93\gg + \ll1\gg}}\right)$$

]

FittedModel::constr :

The property values {ParameterTable} assume an unconstrained model. The results for these properties may not be valid, particularly if the fitted parameters are near a constraint boundary. ≫

	Estimate	Standard Error	t-Statistic	P-Value
mag	1.75189	0.00718028	243.986	$2.402868900305\times10^{-599}$
g	0.410198	0.0000588692	6967.96	$1.108820673392\times10^{-1465}$
y0	−0.133661	0.00213487	−62.6085	2.86082×10^{-264}
b0	−0.656348	0.0120299	−54.5598	6.04629×10^{-234}
y1	0.000793724	0.0000110754	71.6652	3.87402×10^{-295}

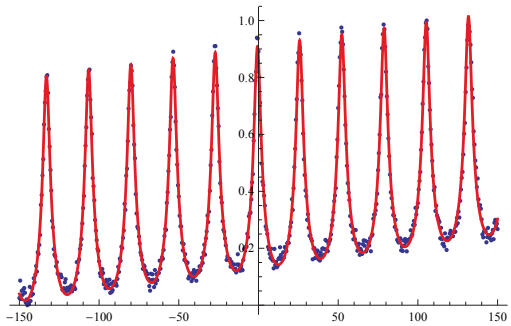

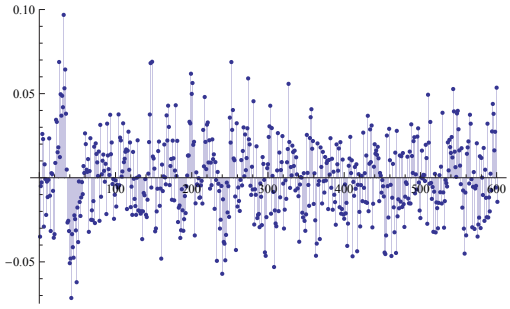

Export Model Fits

10 K Double 2 ns

```
fitForRSNdouble2ns10KTau["BestFitParameters"]
```

```
{mag → 1.52468, g → 0.411565, trc → 23745.7,
 y0 → -0.0594498, b0 → -0.704932, y1 → 0.000901125}
```

```
Export["C:\\Users\\bpursley\\Box
    Sync\\SihLab-Selected\\Publications\\Papers\\SpinNoise_2014-2015\\
    MathematicaExports\\RSN_Double_2ns_10K_table.dat",
  Table[{bfield, fDouble64[2000, 13157.89, 22360, (8.7941*10^-5)*
      fitForRSNdouble2ns10KTau["BestFitParameters"][[2]][[2]]*bfield,
     fitForRSNdouble2ns10KTau["BestFitParameters"][[3]][[2]]]},
   {bfield, -150, 150, 0.05}], "Table"];
```

10 K Double Twice Rep

```
fitForRSNdoubleTwiceRep10KTau29["BestFitParameters"]
```

```
{mag → 1.75189, g → 0.410198, y0 → -0.133661, b0 → -0.656348, y1 → 0.000793724}
```

```
Export["C:\\Users\\bpursley\\Box
    Sync\\SihLab-Selected\\Publications\\Papers\\SpinNoise_2014-2015\\
    MathematicaExports\\RSN_Double_TwiceRep_10K_table.dat",
  Table[{bfield, fDouble64[6578.95, 13157.89, 22360, (8.7941*10^-5)*
      fitForRSNdoubleTwiceRep10KTau29["BestFitParameters"][[2]][[2]]*bfield,
     29000]}, {bfield, -150, 150, 0.05}], "Table"];
```

TRSN Fitting trc = 29 +/- 1 ns from two-pulse 2ns and twice rep fits using 10K tau = 22.360 ns

```
modelTime29 =
  mag*fDouble16[dt - t0, 13157.89, tau, (8.7941*10^-5)*g*(300), 29000] +
   y0 + y1*dt;
```

100 K -- 16 terms

```
fitForTRSNdouble100K29 = NonlinearModelFit[TRSNdouble100K,
  {modelTime29, {mag > 0 , 0.30 < g < 0.42,  10 000 > tau > 0, 0 > y1}},
  {{mag, 5}, {g, 0.38}, {tau, 1000}, {t0, 1650}, {y0, 0}, {y1, 0}},
  dt, MaxIterations -> 5000, PrecisionGoal -> 10]
fitForTRSNdouble100K29["ParameterTable"]
Show[ListPlot[TRSNdouble100K, PlotRange -> All],
 Plot[fitForTRSNdouble100K29[dt], {dt, 400, 3240},
  PlotStyle -> Directive[Thick, Red]], PlotRange -> All]
ListPlot[fitForTRSNdouble100K29["FitResiduals"], Filling -> Axis]
```

FittedModel[

$$-0.390669 - 0.000128048\,dt + 3.88193\left(\left(0.803886\,(1 - \ll 1\gg)\sqrt{\left(1.67543 + \ll 156\gg + e^{\frac{-\ll 10\gg + \ll 1\gg}{29000} - \ll 22\gg \text{Abs}[\ll 1\gg]}\right.}\right.\text{Cos}[0.0100425\,\text{Ab}\right.$$

$$\left.\left.\left(1 + e^{\frac{-13157.9 + \text{Abs}[\ll 1\gg]}{29000}}\right) + \frac{0.803886\left(1 - e^{\frac{\ll 1\gg}{\ll 5\gg}}\right)\sqrt{\ll 1\gg}}{1 + e^{-\frac{\text{Abs}\,\ll 1\gg\,\ll 1\gg|}{29000}}}\right)\right)$$

]

FittedModel::constr :

The property values {ParameterTable} assume an unconstrained model. The results for these properties may not be valid, particularly if the fitted parameters are near a constraint boundary. ≫

	Estimate	Standard Error	t-Statistic	P-Value
mag	3.88193	0.207742	18.6863	4.67921×10^{-28}
g	0.380651	0.0021814	174.499	1.11316×10^{-89}
tau	1064.17	103.814	10.2507	2.76715×10^{-15}
t0	1657.5	2.99946	552.601	1.07963×10^{-122}
y0	−0.390669	0.0592326	−6.59551	8.4324×10^{-9}
y1	−0.000128048	8.46773×10^{-6}	−15.1219	3.98632×10^{-23}

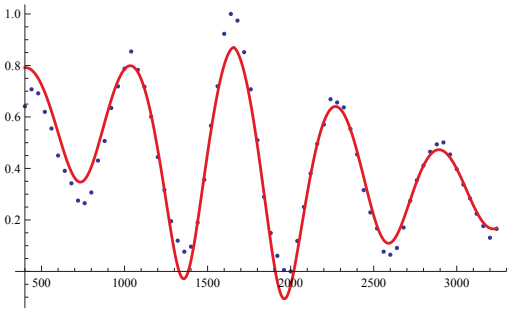

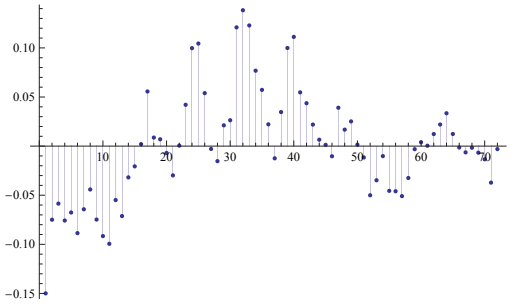

Export Model Fits

100 K 16-terms

```
fitForTRSNdouble100K29["BestFitParameters"]
```

```
{mag → 3.88193, g → 0.380651, tau → 1064.17,
 t0 → 1657.5, y0 → -0.390669, y1 → -0.000128048}
```

```
Export["C:\\Users\\bpursley\\Box
    Sync\\SihLab-Selected\\Publications\\Papers\\SpinNoise_2014-2015\\
    MathematicaExports\\TRSN_100K_16terms_table.dat",
  Table[{dt, fDouble16[dt , 13157.89,
     fitForTRSNdouble100K29["BestFitParameters"][[3]][[2]],
     (8.7941 * 10^-5) * fitForTRSNdouble100K29["BestFitParameters"][[2]][[2]] *
      (300), 29000]}, {dt, -1250, 1250, 10}], "Table"];
```

BIBLIOGRAPHY

BIBLIOGRAPHY

[1] Immanuel Estermann. History of molecular beam research: Personal reminiscences of the important evolutionary period 19191933. *American Journal of Physics*, 43(8):661, 1975.

[2] Bretislav Friedrich and Dudley Herschbach. Stern and Gerlach: How a Bad Cigar Helped Reorient Atomic Physics. *Physics Today*, 56(12):53, 2003.

[3] Alberto Guillen Salas, Watson Attai, Ken Y. Oyadomari, Cedric Priscal, Rogan S. Schimmin, Oriol Tintore Gazulla, and Jasper L. Wolfe. Phonesat In-Flight Experience Results. In *Small Satellites and Services Symposium; 26-30 May 2014; Porto Petro, Majorca ; Spain*, number 2, pages 1–19, Porto Petro, Majorca ; Spain, 2014.

[4] William F. Brinkman, Douglas E. Haggan, and William W. Troutman. A history of the invention of the transistor and where it will lead us. *IEEE Journal of Solid-State Circuits*, 32(12):1858–1864, 1997.

[5] Semiconductor Industry Association. International technology roadmap for semiconductors: Executive summary. *Semiconductor Industry Association, Tech. Rep*, 2013.

[6] Steve S Chung. (Invited) The Random Dopant Fluctuations of Ultra-Scaled CMOS Devices. *ECS Transactions*, 60(1):1027–1032, 2014.

[7] Borkar Shekhar and Andrew A. Chien. The future of microprocessors. *Communications of the ACM*, 54(5), 2011.

[8] Danny Kim, Samuel G. Carter, Alex Greilich, Allan Bracker, and Daniel Gammon. Ultrafast optical control of entanglement between two quantum dot spins. *Nature Physics*, 7(3):24, 2010.

[9] T. Lanting, a. J. Przybysz, a. Yu Smirnov, F. M. Spedalieri, M. H. Amin, a. J. Berkley, R. Harris, F. Altomare, S. Boixo, P. Bunyk, N. Dickson, C. Enderud, J. P. Hilton, E. Hoskinson, M. W. Johnson, E. Ladizinsky, N. Ladizinsky, R. Neufeld, T. Oh, I. Perminov, C. Rich, M. C. Thom, E. Tolkacheva, S. Uchaikin, a. B. Wilson, and G. Rose. Entanglement in a quantum annealing processor. *Physical Review X*, 4(2):1–14, 2014.

[10] Claude Chappert, Albert Fert, and Frédéric Nguyen Van Dau. The emergence of spin electronics in data storage. *Nature materials*, 6(11):813–23, November 2007.

[11] Igor Žutić, Jaroslav Fabian, and S. Das Sarma. Spintronics: Fundamentals and applications. *Reviews of Modern Physics*, 76(2):323–410, April 2004.

[12] Biqin Huang, Douwe J. Monsma, and Ian Appelbaum. Experimental realization of a silicon spin field-effect transistor. *Applied Physics Letters*, 91(7):072501, 2007.

[13] M. Romer, J. Hubner, and M. Oestreich. Spatially resolved doping concentration measurement in semiconductors via spin noise spectroscopy. *Applied Physics Letters*, 94(11):112105, 2009.

[14] Luyi Yang, P Glasenapp, A Greilich, D. Reuter, A. D. Wieck, D. R. Yakovlev, M. Bayer, and S. A. Crooker. Two-colour spin noise spectroscopy and fluctuation correlations reveal homogeneous linewidths within quantum-dot ensembles. *Nature Communications*, 5:4949, September 2014.

[15] Fabian Berski, Hendrik Kuhn, Jan G. Lonnemann, Jens Hübner, and Michael Oestreich. Ultrahigh Bandwidth Spin Noise Spectroscopy: Detection of Large g-Factor Fluctuations in Highly n-Doped GaAs. *Physical Review Letters*, 111(18):5, June 2013.

[16] Jens Hübner, JG Lonnemann, and Petrissa Zell. Rapid scanning of spin noise with two free running ultrafast oscillators. *Optics ...*, 21(5):5872–5878, 2013.

[17] Georg M. Müller, Michael Römer, Jens Hübner, and Michael Oestreich. Gigahertz spin noise spectroscopy in n-doped bulk GaAs. *Physical Review B*, 81(12):121202, March 2010.

[18] Sebastian Starosielec and Daniel Hagele. Ultrafast spin noise spectroscopy. *Applied Physics Letters*, 93(5):051116, 2008.

[19] P. A. M. Dirac. The Quantum Theory of the Electron. *Proceedings of the Royal Society A: Mathematical, Physical and Engineering Sciences*, 117(778):610–624, 1928.

[20] Walther Gerlach and Otto Stern. Der experimentelle Nachweis der Richtungsquantelung im Magnetfeld. *Zeitschrift fur Physik*, 9(1):349–352, 1922.

[21] Otto Stern. A way towards the experimental examination of spatial quantisation in a magnetic field. *Zeitschrift für Physik D Atoms, Molecules and Clusters*, 10(2-3):114–116, 1988.

[22] J. J. Sakurai. *Modern Quantum Mechanics*. Addison Wesley, revised edition, 1993.

[23] J. C. Slater and G. F. Koster. Simplified LCAO method for the periodic potential problem. *Physical Review*, 94(6):1498–1524, 1954.

[24] J Singh. *Electronic and optoelectronic properties of semiconductor structures*. Cambridge University Press, New York, NY, USA, 1st edition, 2007.

[25] Charles Kittel. *Introduction to Solid State Physics*. John Wiley and Sons, Inc., 8th edition, 2005.

[26] Nobelprize.org. The Nobel Prize in Physics 1915, 2014.

[27] J. M. Luttinger and W Kohn. Motion of Electrons and Holes in Perturbed Periodic Fields. *Physical Review*, 97(4):869–883, 1955.

[28] Y. Qi and S. Zhang. Spin diffusion at finite electric and magnetic fields. *Physical Review B*, 67(5):052407, February 2003.

[29] Paul R. Bermin and Vladimir S. Malinovsky. *Principles of Laser Spectroscopy and Quantum Optics*. Princeton University Press, 1rst edition, 2011.

[30] S. Mazzucato, T. T. Zhang, H. Carrère, D. Lagarde, P. Boonpeng, a. Arnoult, G. Lacoste, A. Balocchi, T. Amand, C. Fontaine, X. Marie, H. Carrere, D. Lagarde, P. Boonpeng, a. Arnoult, G. Lacoste, A. Balocchi, T. Amand, C. Fontaine, and X. Marie. Electron spin dynamics and g-factor in GaAsBi. *Applied Physics Letters*, 102(25):252107, 2013.

[31] B. M. Norman, C. J. Trowbridge, D D Awschalom, and V. Sih. Current-Induced Spin Polarization in Anisotropic Spin-Orbit Fields. *Physical Review Letters*, 112(5):056601, February 2014.

[32] F. Bloch, W. Hansen, and M. Packard. The Nuclear Induction Experiment. *Physical Review*, 70(7-8):474–485, October 1946.

[33] F. Bloch. Nuclear Induction. *Physical Review*, 70(7-8):460–474, October 1946.

[34] H. Torrey. Bloch Equations with Diffusion Terms. *Physical Review*, 104(3):563–565, November 1956.

[35] M M Glazov and E L Ivchenko. Resonant spin amplification in nanostructures with anisotropic spin relaxation and spread of the electronic g factor. *Semiconductors*, 42(8):951–957, August 2008.

[36] M. Griesbeck, M. M. Glazov, E. Ya. Sherman, D. Schuh, W. Wegscheider, C. Schüller, and T. Korn. Strongly anisotropic spin relaxation revealed by resonant spin amplification in (110) GaAs quantum wells. *Physical Review B*, 85(8):085313, February 2012.

[37] MI D'yakonov and VI Perel. Spin relaxation of conduction electrons in noncentrosymmetric semiconductors. *Sov. Phys. Solid State*, 13(12):3023–3026, 1972.

[38] R. J. Elliott. Theory of the Effect of Spin-Orbit Coupling on Magnetic Resonance in Some Semiconductors. *Phys. Rev.*, 96(2):266–279, October 1954.

[39] Y Yafet. g Factors and Spin-Lattice Relaxation of Conduction Electrons. *Solid State Physics*, 14:1–98, 1963.

[40] G L Bir, A G Aronov, and G E Pikus. Spin relaxation of electrons due to scattering by holes. *Zh. Eksp. Teor. Fiz*, 69:1382–1397, 1975.

[41] AG Aronov, GE Pikus, and AN Titkov. Spin relaxation of conduction electrons in p-type III-V compounds. *Sov. Phys. JETP*, 1983.

[42] D. Hilton and C. Tang. Optical Orientation and Femtosecond Relaxation of Spin-Polarized Holes in GaAs. *Physical Review Letters*, 89(14):146601, September 2002.

[43] P. R. Berman. Optical Faraday rotation. *American Journal of Physics*, 78(3):270, 2010.

[44] Eugene Hect. *Optics*. Adison Wesley Longman, Inc., 3rd edition, 1998.

[45] R. Giri, S. Cronenberger, M. Vladimirova, D. Scalbert, K. V. Kavokin, M. M. Glazov, M. Nawrocki, A. Lemaître, and J. Bloch. Giant photoinduced Faraday rotation due to the spin-polarized electron gas in an n-GaAs microcavity. *Physical Review B*, 85(19):195313, May 2012.

[46] David J. Griffiths. *Introduction to Electrodynamics*. Prentice-Hall, Inc., Upper Saddle River, New Jersey, 3rd edition, 1999.

[47] Sajeev John, Costas Soukoulis, Morrel H. Cohen, and E. N. Economou. Theory of electron band tails and the urbach optical-absorption edge. *Physical Review Letters*, 57(14):1777–1780, 1986.

[48] T.D. Visser, D. Kuebel, M. Lahiri, T. Shirai, and E. Wolf. Unpolarized light beams with different coherence properties. *Journal of Modern Optics*, 56(12):1369–1374, 2009.

[49] Anthony E. Siegman. *Lasers*. University Science Books, 1rst edition, 1986.

[50] H G Berry, G Gabrielse, and a E Livingston. Measurement of the Stokes parameters of light. *Applied optics*, 16(12):3200–3205, 1977.

[51] C. J. Trowbridge, B. M. Norman, Y. K. Kato, D D Awschalom, and V. Sih. Dynamic nuclear polarization from current-induced electron spin polarization. *Physical Review B*, 90(8):085122, August 2014.

[52] Paul Horowitz and Winfield Hill. *The Art of Electronics*. Cambridge University Press, 3rd edition, 2015.

[53] R. W. Wood and A. Ellett. On the Influence of Magnetic Fields on the Polarisation of Resonance Radiation. *Proceedings of the Royal Society A: Mathematical, Physical and Engineering Sciences*, 103(722):396–403, 1923.

[54] Wilhelm Hanle. Uber magnetische Beeinflussung der Polarisation der Resonanzfluoreszenz. *Zeitschrift fur Physik*, 30(1):93–105, December 1924.

[55] W Hanle. The Hanle-Effect - Level Crossing. *Zeitschrift für Physik D Atoms, Molecules and Clusters*, 18(1):3–4, 1991.

[56] Wilhelm Hanle. Magnetic influence on the polarization of resonance fluorescence. *Atoms, Molecules, and Clusters*, 18(1):5–10, 1991.

[57] John A. Eldridge. Theoretical interpretation of the polarization experiment of Wood and Ellett. *Physical Review*, 24(3):234–242, 1924.

[58] B. Pursley, M. Luengo-Kovac, G. Vardar, R. S. Goldman, and V. Sih. Spin lifetime measurements in GaAsBi thin films. *Applied Physics Letters*, 102(2):022420, November 2013.

[59] Yang Song and Hanan Dery. Magnetic-Field-Modulated Resonant Tunneling in Ferromagnetic-Insulator-Nonmagnetic Junctions. *Physical Review Letters*, 113(4):047205, July 2014.

[60] Ron Jansen. Silicon spintronics. *Nature materials*, 11(5):400–8, May 2012.

[61] J. J. Baumberg, S. A. Crooker, D. D. Awschalom, N. Samarth, H. Luo, and J. K. Furdyna. Ultrafast Faraday spectroscopy in magnetic semiconductor quantum structures. *Physical Review B*, 50(11):7689–7700, 1994.

[62] Kun Zhao, Qi Zhang, Michael Chini, Yi Wu, Xiaowei Wang, and Zenghu Chang. Tailoring a 67 attosecond pulse through advantageous. *Optics Letters*, 37(18):3891–3893, 2012.

[63] J. Kikkawa and D. Awschalom. Resonant Spin Amplification in n-Type GaAs. *Physical Review Letters*, 80(19):4313–4316, May 1998.

[64] C. Hautmann and M. Betz. Magneto-optical analysis of the effective g tensor and electron spin decoherence in the multivalley conduction band of bulk germanium. *Physical Review B*, 85(12):121203, March 2012.

[65] C. Hautmann, B. Surrer, and M. Betz. Ultrafast optical orientation and coherent Larmor precession of electron and hole spins in bulk germanium. *Physical Review B*, 83(16):161203, April 2011.

[66] J Weber. Fluctuation Dissipation Theorem. *Physical Review*, 101(6):1620–1626, March 1956.

[67] Tycho Sleator, Erwin Hahn, Claude Hilbert, and John Clarke. Nuclear-spin noise. *Physical Review Letters*, 55(17):1742–1745, October 1985.

[68] E B Aleksandrov and V S Zapasskil. Magnetic resonance in the Faraday-rotation noise spectrum. *Sov. Phys. JETP*, 54:64–67, 1981.

[69] S. A. Crooker, D G Rickel, a V Balatsky, and D L Smith. Spectroscopy of spontaneous spin noise as a probe of spin dynamics and magnetic resonance. *Nature*, 431(7004):49–52, September 2004.

[70] M. Oestreich, M. Römer, R. Haug, and D. Hägele. Spin Noise Spectroscopy in GaAs. *Physical Review Letters*, 95(21):216603, November 2005.

[71] Georg M. Müller, Michael Oestreich, Michael Römer, and Jens Hübner. Semiconductor spin noise spectroscopy: Fundamentals, accomplishments, and challenges. *Physica E: Low-dimensional Systems and Nanostructures*, 43(2):569–587, December 2010.

[72] Valerii S Zapasskii. Spin-noise spectroscopy: from proof of principle to applications. *Advances in Optics and Photonics*, 5(2):131, June 2013.

[73] S. A. Crooker, Lili Cheng, and Darryl Smith. Spin noise of conduction electrons in n-type bulk GaAs. *Physical Review B*, 79(3):035208, January 2009.

[74] M. Römer, J. Hübner, and M. Oestreich. Spin noise spectroscopy in semiconductors. *The Review of scientific instruments*, 78(10):103903, October 2007.

[75] Georg M. Muller, Michael Romer, Jens Hubner, and Michael Oestreich. Efficient data averaging for spin noise spectroscopy in semiconductors. *Applied Physics Letters*, 97(19):192109, 2010.

[76] D. G. Cooke, F. A. Hegmann, E. C. Young, and T. Tiedje. Electron mobility in dilute GaAs bismide and nitride alloys measured by time-resolved terahertz spectroscopy. *Appl. Phys. Lett.*, 89(12):122103, 2006.

[77] T. Tiedje, E.C. Young, and A. Mascarenhas. Growth and properties of the dilute bismide semiconductor GaAs1xBix a complementary alloy to the dilute nitrides. *Int. J. Nanotechnol.*, 5(9/10/11/12):963, 2008.

[78] R. N. Kini, L. Bhusal, A. J. Ptak, R. France, and A. Mascarenhas. Electron Hall mobility in GaAsBi. *J. Appl. Phys.*, 106(4):043705, 2009.

[79] B. Fluegel, S. Francoeur, A. Mascarenhas, S. Tixier, E. Young, and T. Tiedje. Giant Spin-Orbit Bowing in GaAs1-xBix. *Phys. Rev. Lett.*, 97(6):067205, August 2006.

[80] G. Vardar, S. W. Paleg, M. V. Warren, M. Kang, S. Jeon, and R. S. Goldman. Mechanisms of droplet formation and Bi incorporation during molecular beam epitaxy of GaAsBi. *Applied Physics Letters*, 102(4):042106, 2013.

[81] R. Kudrawiec, M. Syperek, P. Poloczek, J. Misiewicz, R. H. Mari, M. Shafi, M. Henini, Y. Galvao Gobato, S. V. Novikov, J. Ibanez, M. Schmidbauer, and S. I. Molina. Carrier localization in GaBiAs probed by photomodulated transmittance and photoluminescence. *J. Appl. Phys.*, 106(2):023518, 2009.

[82] S. Imhof, A. Thranhardt, A. Chernikov, M. Koch, N. S. Koster, K. Kolata, S. Chatterjee, S. W. Koch, X. Lu, S. R. Johnson, D. A. Beaton, T. Tiedje, and O. Rubel. Clustering effects in Ga(AsBi). *Appl. Phys. Lett.*, 96(13):131115, 2010.

[83] S. Francoeur, S. Tixier, E. Young, T. Tiedje, and A. Mascarenhas. Bi isoelectronic impurities in GaAs. *Phys. Rev. B*, 77(8):085209, February 2008.

[84] D. L. Sales, E. Guerrero, J. F. Rodrigo, P. L. Galindo, A. Yanez, M. Shafi, A. Khatab, R. H. Mari, M. Henini, S. Novikov, M. F. Chisholm, and S. I. Molina. Distribution of bismuth atoms in epitaxial GaAsBi. *Appl. Phys. Lett.*, 98(10):101902, 2011.

[85] G. Ciatto, E. Young, F. Glas, J. Chen, R. Mori, and T. Tiedje. Spatial correlation between Bi atoms in dilute GaAs1xBix: From random distribution to Bi pairing and clustering. *Phys. Rev. B*, 78(3):035325, July 2008.

[86] R. Kini, A. Ptak, B. Fluegel, R. France, R. Reedy, and A. Mascarenhas. Effect of Bi alloying on the hole transport in the dilute bismide alloy GaAs_{1-x}Bi_{x}. *Phys. Rev. B*, 83(7):075307, February 2011.

[87] S. Nargelas, K. Jarasiunas, K. Bertulis, and V. Pacebutas. Hole diffusivity in GaAsBi alloys measured by a picosecond transient grating technique. *Appl. Phys. Lett.*, 98(8):082115, 2011.

[88] C. A. Broderick, M. Usman, A. Lindsay, and E. P. O'Reilly. Tight binding analysis of the electronic structure of dilute bismide and nitride alloys of GaAs. In *2011 13th International Conference on Transparent Optical Networks*, pages 1–4. IEEE, June 2011.

[89] Muhammad Usman, Christopher Broderick, Andrew Lindsay, and Eoin OReilly. Tight-binding analysis of the electronic structure of dilute bismide alloys of GaP and GaAs. *Phys. Rev. B*, 84(24):245202, December 2011.

[90] Nathaniel A. Riordan, Chaturvedi Gogineni, Shane R. Johnson, Xianfeng Lu, Tom Tiedje, Ding Ding, Yong-Hang Zhang, Rafael Fritz, Kolja Kolata, Sangam Chatterjee, Kerstin Volz, and Stephan W. Koch. Temperature and pump power dependent photoluminescence characterization of MBE grown GaAsBi on GaAs. *J. Mater. Sci.: Mater. Electron.*, 23(10):1799–1804, March 2012.

[91] I. Malajovich, J. M. Kikkawa, D D Awschalom, J. J. Berry, and N. Samarth. Resonant amplification of spin transferred across a GaAs/ZnSe interface. *J. Appl. Phys.*, 87(9):5073, 2000.

[92] Y. Puttisong, X. J. Wang, I. A. Buyanova, C. W. Tu, L. Geelhaar, H. Riechert, and W. M. Chen. Room-temperature spin injection and spin loss across a GaNAs/GaAs interface. *Appl. Phys. Lett.*, 98(1):012112, 2011.

[93] Pil Song and K. Kim. Spin relaxation of conduction electrons in bulk III-V semiconductors. *Physical Review B*, 66(3):1–8, July 2002.

[94] D. Dagnelund, J. Puustinen, M. Guina, W. M. Chen, and I. a. Buyanova. Identification of an isolated arsenic antisite defect in GaAsBi. *Applied Physics Letters*, 104(5):052110, 2014.

[95] Brennan C Pursley, X Song, E A Bokari, A Kayani, and V Sih. Robustness of n-GaAs carrier spin properties to 5 MeV proton irradiation. *Appl. Phys. Lett.*, 106(7):072403, 2015.

[96] Helmuth Spieler. Introduction to radiation-resistant semiconductor devices and circuits. *AIP Conference Proceedings*, 390:23–49, 1997.

[97] David Awschalom and Nitin Samarth. Spintronics without magnetism. *Physics*, 2:50, June 2009.

[98] Behtash Behin-Aein, Deepanjan Datta, Sayeef Salahuddin, and Supriyo Datta. Proposal for an all-spin logic device with built-in memory. *Nature nanotechnology*, 5(4):266–70, April 2010.

[99] Hanan Dery, Yang Song, Pengke Li, and Igor Zutic. Silicon spin communication. *Applied Physics Letters*, 99(8):082502, 2011.

[100] Igor Žutić and Hanan Dery. Spintronics: Taming spin currents. *Nature materials*, 10(9):647–8, September 2011.

[101] Jeongsu Lee, Rafa Oszwadowski, Christian Gø thgen, and Igor Žutić. Mapping between quantum dot and quantum well lasers: From conventional to spin lasers. *Physical Review B*, 85(4):045314, January 2012.

[102] K Vogt, F Y Fradin, J E Pearson, T Sebastian, S D Bader, B Hillebrands, A Hoffmann, and H Schultheiss. Realization of a spin-wave multiplexer. *Nature communications*, 5:3727, January 2014.

[103] Ju-Ying Chen, Tong-Ming Wong, Che-Wei Chang, Chen-Yuan Dong, and Yang-Fang Chen. Self-polarized spin-nanolasers. *Nature nanotechnology*, 9(10):845–50, October 2014.

[104] S.M. Khanna, A. Houdayer, A. Jorio, C. Carlone, M. Parentean, and J.W. Gerdes. Nuclear radiation displacement damage prediction in gallium arsenide through low temperature photoluminescence measurements. *IEEE Transactions on Nuclear Science*, 43(6):2601–2608, 1996.

[105] L. F. Zakharenkov, V. V. Kozlovskii, and B. A. Shustrov. Transmutation Doping of Indium Phosphide and Gallium Arsenide Due to Protons and α-Particles. *physica status solidi (a)*, 117(1):85–90, January 1990.

[106] Alejandro Sonzogni. National Nuclear Data Center, information extracted from the NuDat 2 database (ver 2.6), 2014.

[107] Anouar Jorio, Chedly Rejeb, Martin Parenteau, Cosmo Carlone, and Shyam M. Khanna. Radiation induced carrier enhancement and intrinsic defect transformation in n-GaAs. *Journal of Applied Physics*, 74(4):2310, 1993.

[108] R Jansen, S P Dash, S Sharma, and B C Min. Silicon spintronics with ferromagnetic tunnel devices. *Semiconductor Science and Technology*, 27(8):083001, August 2012.

[109] Pengke Li and Hanan Dery. Theory of Spin-Dependent Phonon-Assisted Optical Transitions in Silicon. *Physical Review Letters*, 105(3):3–6, July 2010.

[110] J. Cheng, J. Rioux, J. Fabian, and J. Sipe. Theory of optical spin orientation in silicon. *Physical Review B*, 83(16):165211, April 2011.

[111] Jesús a. del Alamo and Richard M. Swanson. Modelling of minority-carrier transport in heavily doped silicon emitters. *Solid-State Electronics*, 30(11):1127–1136, 1987.

[112] M.S. Tyagi and R. Van Overstraeten. Minority carrier recombination in heavily-doped silicon. *Solid-State Electronics*, 26(6):577–597, 1983.

[113] Yang Song, Oleg Chalaev, and Hanan Dery. Donor-Driven Spin Relaxation in Multivalley Semiconductors. *Physical Review Letters*, 113(16):167201, October 2014.

[114] J. Lohrenz, T. Paschen, and M. Betz. Resonant spin amplification in intrinsic bulk germanium: Evidence for electron spin lifetimes exceeding 50 ns. *Physical Review B*, 89(12):121201, March 2014.

[115] R. Dzhioev, K. Kavokin, V. Korenev, M. Lazarev, B. Meltser, M. Stepanova, B. Zakharchenya, D Gammon, and D. Katzer. Low-temperature spin relaxation in n-type GaAs. *Phys. Rev. B*, 66(24):1–7, December 2002.

[116] M. Römer, H. Bernien, G. Müller, D. Schuh, J. Hübner, and M. Oestreich. Electron-spin relaxation in bulk GaAs for doping densities close to the metal-to-insulator transition. *Physical Review B*, 81(7):075216, February 2010.

[117] M. P. Walser, C. Reichl, W. Wegscheider, and G. Salis. Direct mapping of the formation of a persistent spin helix. *Nature Physics*, 8(10):757–762, August 2012.